THERMALLY INDUCED WETTABILITY CHANGE DURING SAGD FOR OIL SAND EXTRACTION

A Thesis

by

YASIN UNAL

Submitted to the Office of Graduate and Professional Studies of
Texas A&M University
in partial fulfillment of the requirements for the degree of

MASTER OF SCIENCE

Chair of Committee,	Berna Hascakir
Committee Members,	Robert H. Lane
	Tahir Cagin
Head of Department,	A. Daniel Hill

December 2014

Major Subject: Petroleum Engineering

ABSTRACT

Steam-assisted gravity drainage (SAGD) is an in-situ bitumen extraction technique that significantly increases ultimate oil recovery from oil sand reservoirs. Because SAGD is one of the newest proven thermal oil recovery techniques, laboratory test and field pilot efforts are in progress to enhance oil recovery by using less energy and water for steam generation. These efforts are simplified with the contribution of numerical simulations to optimize the oil recovery of SAGD projects.

Several critical parameters determine the reliability of numerical simulation for SAGD, and wettability is one of the most crucial parameters defining the microscopic displacement efficiency with the change in relative permeabilities, interfacial tension, and capillary pressure.

In this work, relative permeability as a function of temperature are determined during SAGD for bitumen extraction from oil sand reservoirs numerically. Three SAGD experiments are used to validate the accuracy of simulation studies. The effect of injection temperature and clay type in the formation on SAGD performance were investigated experimentally. Cumulative oil recovery, cumulative water production, and temperature distribution in time for each experiment are used as history-matching parameters of the numerical simulation.

Contact angle, zeta potential, interfacial/surface tension, residual fluid saturation, X-ray diffraction (XRD), and scanning electron microscope (SEM) measurements are conducted on produced oil, produced water, and spent rock samples to determine the

relative permeability endpoint changes with temperature and with clay type in the formation. Three experimental results are combined with the experimental analyses on produced samples to numerically obtain the relative permeability change at each experimental condition.

Numerical results are in good agreement with the experimental findings. History-match is obtained in all three experiments by only changing the relative permeability endpoints, which proves the reliability of the numerical model and the relative permeability assumptions. For the case in which temperature is the only variable, relative permeabilities are adjusted to represent water-wet behavior at higher temperatures. For the case in which clay type is the only variable, relative permeability endpoints are tuned to better represent different wettability characteristics observed for each clay type.

DEDICATION

To my parents…

ACKNOWLEDGEMENTS

First of all, I would like to thank Dr. Hascakir for her precious efforts and guidance throughout this study. I wish to express my appreciation for her supervision and financial support. I am also grateful to Dr. Lane and Dr. Cagin for accepting to serve on my committee.

A special thanks to Albina, who conducted the experiments I worked on for my research. Without her contribution, the results of this study could not be achieved. I also want to thank all the past and current members of the Texas A&M University Heavy Oil, Oil Shales, Oil Sands, & Carbonate Analysis and Recovery Methods (HOCAM) group.

Thanks also to all my friends, who motivated and helped me whenever I felt discouraged.

Finally, the scholarship provided by Turkish Petroleum Corporation is gratefully appreciated.

NOMENCLATURE

2D	two-dimensional
AOSTRA	Alberta Oil Sands Technology and Research Authority
BDNS	barium dinonyl naphthalene sulfonate
BIC	Brookhaven Instruments Corporation
CMG	Computer Modelling Group Ltd.
CSS	cyclic steam stimulation
CTL	coal-to-liquid
DDDC	dual-drop-dual-crystal
EIA	Energy Information Administration
ELS	electrophoretic light scattering
EOR	enhanced oil recovery
GTL	gas-to-liquid
HWI	hot water injection
IEA	International Energy Agency
IWS	irreducible water saturation
k_{rg}	relative permeability to gas at S_l
k_{rog}	relative permeability to oil at S_l
k_{row}	relative permeability to oil at S_w
k_{rw}	relative permeability to water at S_w
OOIP	original oil in place

OPEC	Organization of the Petroleum Exporting Countries
PALS	phase analysis light scattering
PTFE	polytetrafluoroethylene
ROS	residual oil saturation
RWS	residual water saturation
SAGD	steam-assisted gravity drainage
SEM	scanning electron microscope
S_l	liquid saturation
S_{org}	residual oil saturation for gas injection
S_{orw}	residual oil saturation for water injection
S_w	water saturation
S_{wr}	irreducible water saturation
TDS	total dissolved solids
USBM	US Bureau of Mines
UTF	underground test facility
XRD	X-ray diffraction

TABLE OF CONTENTS

Page

LIST OF FIGURES

Page

LIST OF TABLES

Page

CHAPTER I

INTRODUCTION AND LITERATURE REVIEW

Developments in technology and industry yield an increasing energy demand, which causes the search for new energy supplies. Most of this demand has been supplied by fossil fuels, a trend that will continue until renewable energy (solar, wind, etc.) becomes cheaper than fossil fuels. According to the 2013 Organization of the Petroleum Exporting Countries (OPEC) world oil report, the demand for energy will increase by 52%, 80% of which will still be supplied by fossil fuels in 2035 (Abdul-Hamid, 2013). This fact reveals that there will be a huge demand for fossil fuels as well as oil in the near future.

The main source for oil in the 20th century was conventional resources, which contain light- to medium-gravity liquid hydrocarbons in porous and permeable reservoirs. However, according to the research of Greene et al. (2006), a peak in conventional oil production is almost certain, and there will be a transition from conventional resources to unconventional resources that makes unconventional oil resources more important in the 21st century.

Unconventional oil cannot be produced effectively without heating or diluting it, and the International Energy Agency (IEA (2011)) classified unconventional oil as extra-heavy oil, bitumen (oil sands), kerogen oil, gas-to-liquid (GTL), and coal-to-liquid (CTL). Because almost 70% of the world's oil resources is unconventional, it is vital to produce from unconventional oil reserves to supply the increasing oil demand of the world (Alboudwarej et al., 2006). The unconventional liquid fuel production in 2008 was only

3.9 million bbl./d. However, this number increased to 13.1 million bbl./d in 2012, and it is expected to supply 12% of total world oil demand by 2035 (Rajnauth, 2012).

The third largest proven oil reserve in the world, after Saudi Arabia and Venezuela, is controlled by Canada. This reserve contains 173.6 billion bbl. of oil, 98% of which (approximately 170 billion bbl.) is from oil sands. Most of these oil sands are located in Alberta. A typical oil sand is composed of approximately 83% sand, 14% bitumen, and 3% water by weight, and almost 90% of the solid matrix is quartz, with the rest being silt and clay (Nasr and Ayodele, 2005).

Although Canada has giant oil sand deposits, production has a relatively high break-even price due to advanced and costly extraction techniques (EIA, 2012). In 2011, 1.74 million bbl./d of bitumen was produced, and this production rate will increase to 3.7 million bbl./d by 2021 in Alberta (Government, 2013a). There are three major oil sand areas in Canada: Athabasca, Cold Lake, and Peace River. It is expected that Alberta's oil sand exploration and development programs will continue to increase due to decreasing conventional hydrocarbon reserves. In addition, technological advancements in production techniques will help to maintain these developments (Hein and Marsh, 2008).

Primary recovery methods can recover up to 20 to 30% of the original oil in place (OOIP). Secondary recovery methods can increase the recovery up to 40%. However, these methods cannot be applied effectively for some reservoirs. Therefore, enhanced oil recovery (EOR) can be implemented for the depleting conventional reservoirs with a maximum 65% recovery or for the unconventional ones even at an initial stage. There are several EOR methods in which a fluid is used to displace oil in the reservoir. CO_2,

polymers, surfactants, and steam are some of the fluids injected during EOR, and fluid selections are based on several techniques (Tunio et al., 2011). For instance, due to high viscosities of bitumen, fluid displacement can only be achieved by heat introduction. Steam injection is one of the most reliable and easy-to-apply thermal EOR methods. Displacement efficiency of thermal recovery depends on the following mechanisms: thermal expansion, viscosity reduction, and wettability alteration. While thermal expansion plays a crucial role in light-oil displacement, viscosity reduction and wettability change are effective for heavy-oil displacement (Prats, 1982).

Steamflooding is one of the most reliable and easy-to-apply steam injection methods. However, its success is limited in Canadian oil sands due to low initial mobility of the bitumen. CSS is another steam injection method that some Canadian in-situ oil sand recovery projects currently operate. The recovery percentage of this method is very low (less than 20%) when compared with other thermal recovery processes. In addition, CSS is not suitable for some types of reservoirs, such as solution gas drive reservoirs (Nasr and Ayodele, 2005).

SAGD is the most promising thermal recovery method for high-viscosity bitumen reservoirs when compared with steamflooding and CSS. It enables high oil recovery and reduces the number of wells drilled. Butler (1994) compares two steam projects for bitumen and heavy oil reservoirs, both of which have horizontal producers and steam injection wells. The findings of this study reveal that horizontal wells in an SAGD well configuration have feasible oil production during steamflooding without bypassing steam. This result can be explained by the increase in the effective area to be swept by steam.

Peace River oil sand deposits extend 6200 km^2 and contain 12 billion m^3 of bitumen. Production comes from the Bullhead member of the Cretaceous Bluesky/Gething zone, and the average depth of this formation is 600 m (Hamm and Ong, 1995). Primary bitumen production is only possible at some parts of Peace River and Lloydminster oil sands, with less than 20% recovery rates.

First discovery of Peace River oil sand deposits was in 1949. Shell Canada started several in-situ recovery tests after that time. The company applied a steam-soak project in 1962 and then implemented steam drive and in-situ combustion in 1965. In 1979, Shell started a 31-well cyclic steam stimulation (CSS) pilot, which continued for 13 years until 1992 (Adams et al., 2012). Shell also applied a SAGD field-pilot in 1996 in Peace River (Bell et al., 2010).

1.1 History and Current Status of SAGD

In 1974 the Alberta government established a corporation for developing new oil sand production technologies by creating a collaborative environment for both industry and researchers: the Alberta Oil Sands Technology and Research Authority (AOSTRA). The main purpose of this corporation was to find new ways to extract oil from oil sand reservoirs inaccessible by surface mining techniques. After the introduction of SAGD by Dr. Roger Butler in 1978, AOSTRA quickly supported this promising innovation for in-situ oil sand production technology. Then, there was a testing period of SAGD at the AOSTRA underground test facility (UTF), which was operated by 10 industrial organizations and supported by government (Deutsch and McLennan, 2005). Good et al. (1994) mention SAGD field tests in Canada. AOSTRA UTF Phase A and Phase B and

Shell Peace River Horizontal Well Demonstration Project are described in detail, with a production cost comparison to better state the commercial potential of SAGD and a conclusion that developing SAGD technology can lead to an increase in remaining world oil reserves by almost 25%.

SAGD has become a more popular in-situ oil sand extraction technique day by day, and companies in Canada invest more money for SAGD projects each year. The total number of active SAGD projects increased from 5 to 18 from 2000 to 2014 (Government, 2013b; OilSandsReview, 2014). The complete list of currently active oil sand projects and their capacities are shown in **TABLE 1.** Cenovus Energy Inc. has the biggest SAGD project capacity and it is followed by Suncor Energy Inc. and China National Offshore Oil Corporation Ltd.. The greatest oil recovery is obtained in Athabasca region with SAGD method because the SAGD performance is highly depending on geology and the geological properties of Athabasca is in favor of SAGD projects (Jimenez, 2008).

TABLE 1—CURRENT SAGD PROJECTS AND THEIR CAPACITIES (OilSandsReview, 2014)

Operator	Project Name	Capacity (bbl/d)
Blackpearl Resources Inc.	Blackrod	800
Canadian Natural Resources Ltd.	Kirby	40,000
Cenovus Energy Inc.	Christina Lake	138,800
Cenovus Energy Inc.	Foster Creek	120,000
Cenovus Energy Inc.	Grand Rapids	600
China National Offshore Oil Corporation Ltd.	Long Lake	72,000
Connacher Oil and Gas Ltd.	Great Divide	20,000
ConocoPhillips Canada Ltd.	Surmont	28,200
Devon Canada Corporation	Jackfish	70,000
Husky Energy Inc.	Tucker	30,000
Japan Canada Oil Sands Ltd.	Hangingstone	11,000
MEG Energy Corporation	Christina Lake	60,000
Pengrowth Energy Corporation	Lindbergh	1,260
Royal Dutch Shell PLC	Orion	10,000
Southern Pacific Resource Corporation	STP Mckay	12,000
Statoil	Kai Kos Dehseh	10,000
Suncor Energy Inc.	Firebag	180,000
Suncor Energy Inc.	Mackay River	33,000

1.2 Theory of SAGD

SAGD is based on one horizontal well pair drilled inside an oil sand formation. SAGD depends on continues steam injection from the upper well in the horizontal well pair. During steam chamber development, steam condensates at the outer boundary of the steam chamber, and both heated oil and condensate water drains to the production well from the edge of the steam chamber as a result of gravitational force. The steam chamber grows both upward and sideways at first, and after it reaches the overburden formation, the growth continues laterally. Heated oil also drains inside the steam chamber, which

causes countercurrent flow within the steam chamber in the opposite direction to steam flow. A cross-sectional view of an SAGD well pair and a schematic description of SAGD are presented in **Fig. 1.**

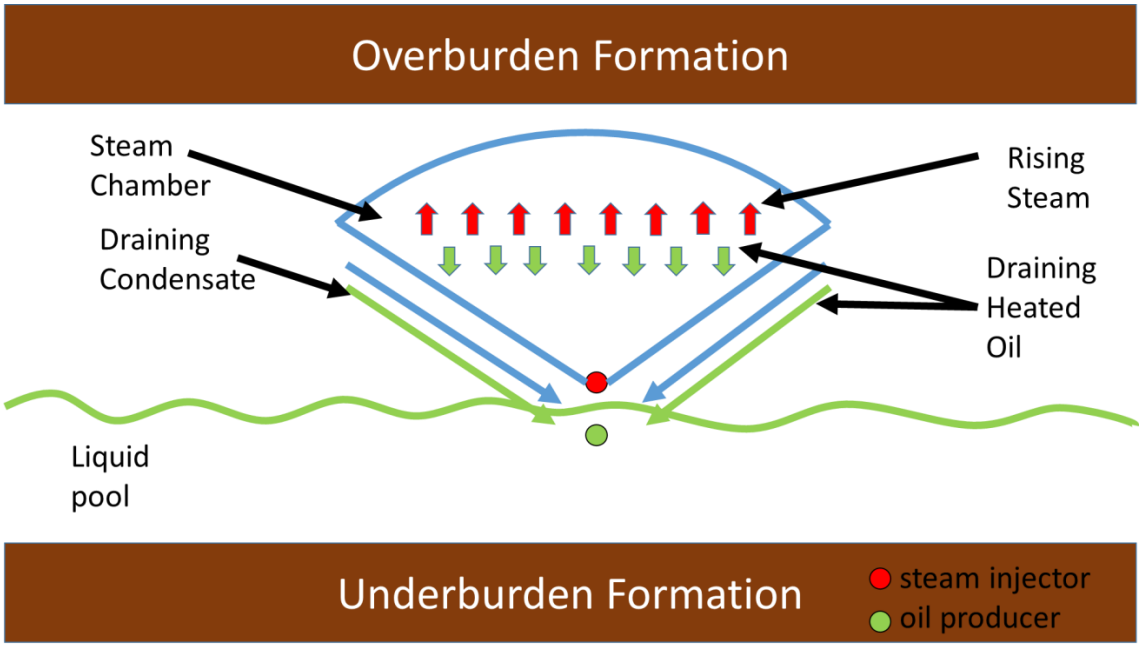

Fig. 1—Conceptual diagram of SAGD process (Bahlani and Babadagli, 2008).

For an economic SAGD project, there are several cutoffs for reservoir properties, such as the pay thickness must be thicker than 12 m and average reservoir permeability should be higher than 3 Darcy. At least 1000-kPa pressure at the reservoir has to be sustained during SAGD operations, and there should not be any contact with bottom water or top gas zones (Bahlani and Babadagli, 2008).

Wettability is playing a crucial role in displacement efficiency of oil by hot fluid injection. Prats (1982) provided a graph at which relative contribution of displacement

mechanisms on the displacement efficiency of oil (**Fig. 2**) which shows wettability and viscosity reduction are very important during heavy oil extraction with hot fluids.

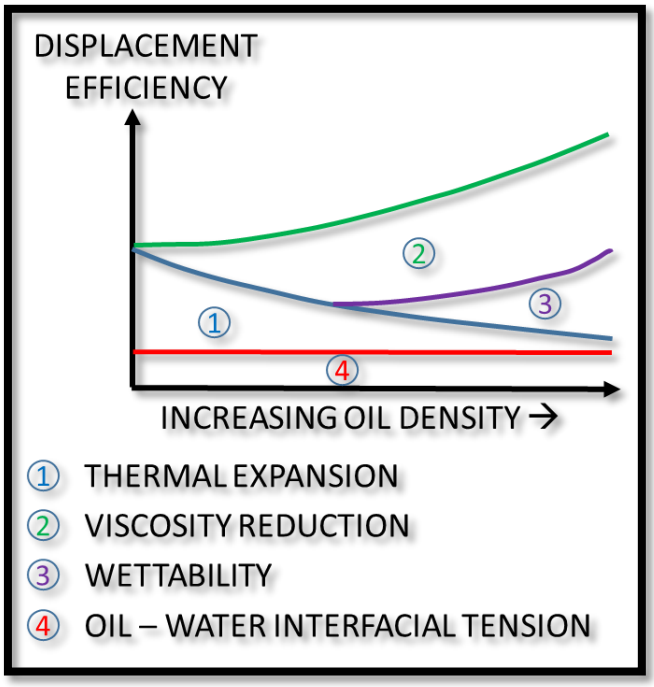

Fig. 2—The effect of recovery mechanisms on displacement efficiency of oil by hot fluid injection (Prats, 1982).

1.3 Wettability

The definition of wettability is given as "*the tendency of one fluid to spread on or adhere to a solid surface in the presence of other immiscible fluids.*"(Anderson, 1986). If a rock is water-wet in a rock/oil/brine system, water tends to fill the small pores and most of the rock surface is covered by water. If the rock is oil-wet in a rock/oil/brine system, the pore-occupying fluid is oil and the majority of the rock surface is covered by oil. Relative permeability, capillary pressure, waterflood behavior, irreducible water

saturation (IWS), and residual oil saturation (ROS) are several examples of reservoir characteristics affected by changes in wettability (Anderson, 1986). To determine wettability change, Amott, US Bureau of Mines (USBM), and contact angle methods can be implemented (Kwan, 1998). In addition, electrical double layer repulsion and Van der Waals force give an inference of the water film thickness around rock and crude oil surfaces. Therefore, zeta potential measurements can be used for determining water film stability, which is closely related to the wettability preference of the rock (Quan et al., 2012). Contact angle and zeta potential methods will be described in the below sections.

1.3.1 Contact Angle

The wettability of a surface can be determined by using contact angle measurements. This method is based on using a small piece of rock and two immiscible fluids. Alotaibi et al. (2010) mention the classification of wettability in terms of oil-water contact angle being water-wet (0 to 75^{o}), intermediate-wet (75 to 115^{o}), or oil-wet (115 to 180^{o}). This classification can be detailed by adding weakly water-wet (55 to 75^{o}) and weakly oil-wet (115 to 135^{o}) subcategories.

Drop shape analysis is a trusted way of measuring contact angles, with regard to the following assumptions:

- The drop is symmetrical in the vertical direction, which means it is independent of direction of drop view.
- Because the drop is not in motion, viscosity and inertia do not play a role in shaping the drop. The only active forces on shaping the drop are interfacial tension and gravity.

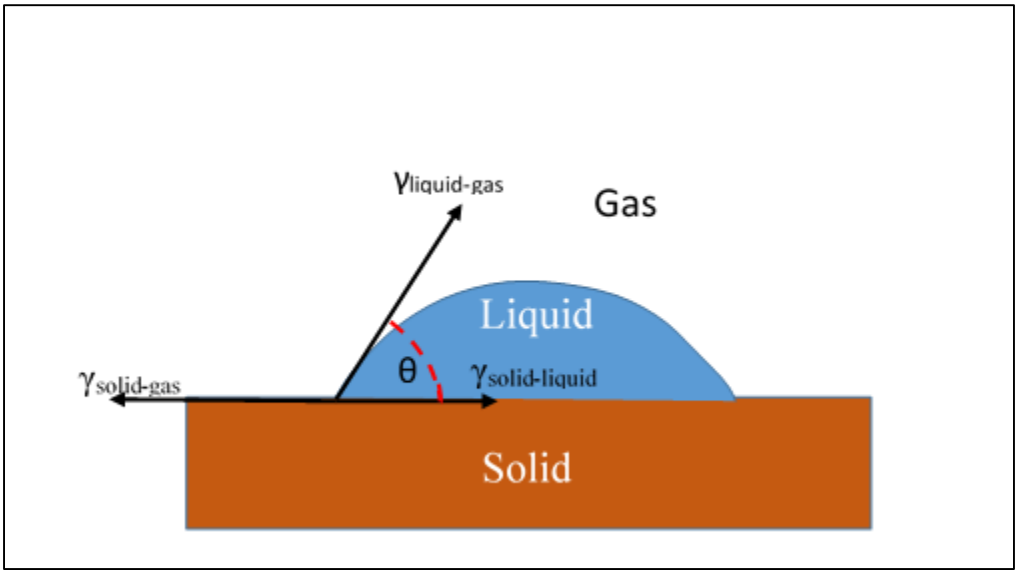

Fig. 3—Diagram of air-water contact angle.

A diagram for air-water contact angle can be seen in **Fig. 3.** Young's contact angle formula combines the surface tensions (γ) of three interfaces and relates them with an angle value (Glover, 2014).

$$\cos\theta = \frac{\gamma_{solid-gas} - \gamma_{solid-liquid}}{\gamma_{liquid-gas}} \ ,$$

where:

θ = Young's contact angle

$\gamma_{solid-gas}$ = interfacial tension between solid and gas

$\gamma_{solid-liquid}$ = interfacial tension between solid and liquid

$\gamma_{liquid-gas}$ = interfacial tension between liquid and gas

Van Dijke and Sorbie (2002) conducted an analytical study to better understand the relation between interfacial tension and wettability in three-phase systems. Their research focuses on the Bartell and Osterhof equation for weakly wetted three-phase systems and introduces relationships between gas-oil, gas-water, and oil-water contact angles. The Bartell and Osterhof equation is given as

$$\sigma_{gw}\cos\theta_{gw} = \sigma_{go}\cos\theta_{go} + \sigma_{ow}\cos\theta_{ow}\,,$$

where:

θ_{gw} = water-gas contact angle

θ_{ow} = oil-water contact angle

θ_{go} = oil-gas contact angle

σ_{go} = oil-gas interfacial tension

σ_{ow} = oil-water interfacial tension

σ_{gw} = water-gas interfacial tension

Van Dijke and Sorbie (2002) propose a linear relationship between water-gas contact angle and oil-water contact angle. The linear equation is given as

$$\cos\theta_{wa} = \left[\frac{1-(\sigma_{oa}-\sigma_{ow})/\sigma_{wa}}{2}\right]\cos\theta_{ow} + \left[\frac{1+(\sigma_{oa}-\sigma_{ow})/\sigma_{wa}}{2}\right],$$

where:

θ_{wa} = air-water contact angle

θ_{ow} = oil-water contact angle

σ_{oa} = oil-air interfacial tension

σ_{ow} = oil-water interfacial tension

σ_{wa} = water-air interfacial tension

This linear relationship between water-air contact angle and oil-water contact angle was validated by an experimental study of Grate et al. (2012), in which they used silica surfaces with different wettability characteristics, water, and hexadecane droplets. Their experimental results are in a good agreement with the linear assumption of Van Dijke and Sorbie (2002).

1.3.2 Zeta Potential

Zeta potential is a measuring method of particle surface charge within a liquid. Because this value gives an idea about the interaction between liquid and solid particles, it is used in several processes, such as water treatment, paper manufacturing, mining, and petroleum production. More specifically, zeta potential is the electrical double layer potential that develops around solid particles in a liquid sample, and it gives an idea about the surface charge of the solid. Zeta potential gives a general idea about the stability of suspensions, as can be seen in **TABLE 2.** High zeta potential value shows the tested suspension is in extremely good stability, while low zeta potential value indicates low stability even precipitation.

TABLE 2—STABILITY DETERMINATION OF SUSPENSION USING ZETA POTENTIAL (Riddick, 1968)

Zeta Potential (mV)	Suspension Stability
From 0 to +3	Maximum agglomeration and precipitation
From +5 to –5	Range of strong agglomeration and precipitation
From –10 to –15	Threshold of agglomeration
From –16 to –30	Threshold of delicate dispersion
From –31 to –40	Moderate stability
From –41 to –60	Fairly good stability
From –61 to –80	Very good stability
From –81 to –100	Extremely good stability

The most common application in the petroleum industry is to determine the colloidal stability of emulsions and suspensions like drilling fluids. Another usage of this method in the petroleum industry is finding the proper waterflooding composition to change the reservoir wettability characteristic to more water-wet. By accomplishing this wettability change to a more water-wet state, oil recovery rates are expected to be higher.

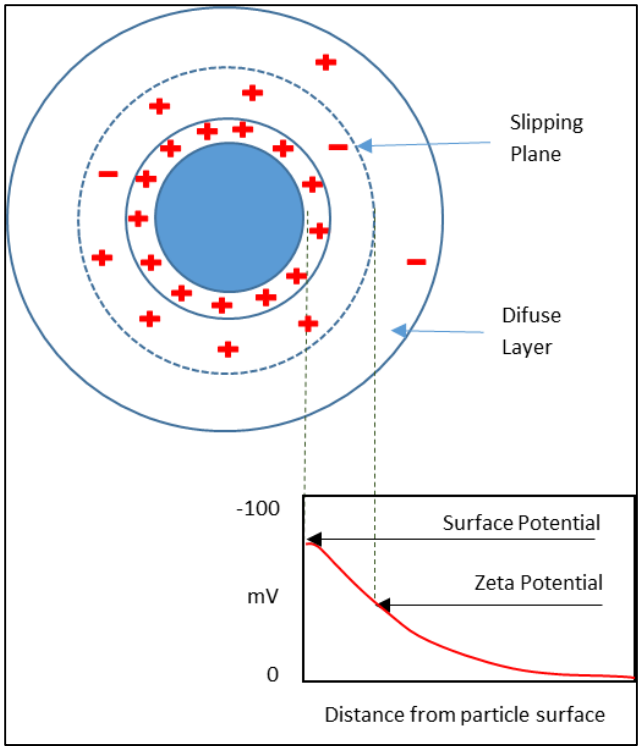

Fig. 4—Charge system in colloidal system and representation with zeta and surface potential (Xu (2010)).

Most zeta potential literature focuses on brine/clay and brine/sand interactions (Nasralla and Nasr-El-Din, 2011; Quan et al., 2012). Some papers are specifically related to the ore flotation industry, emphasizing the relationship between brine/clay interactions from the point of view of zeta potential (Hussain et al., 1996; Kaya et al., 2003). There are also some articles that mention the bitumen/clay zeta potentials for bitumen extraction at the hot-water-processing plants of oil sand mines in Canada (Jiang et al., 2010; Liu et al., 2005; Liu et al., 2002).

As can be seen in **Fig. 4,** Yukselen and Kaya (2003) give the definition of zeta potential as the electrical potential developed at the solid-liquid interface that is the result

of relative movement of the particles and water. Despite the fact that the location of zeta potential is not clear, it gives consistent results, indicating the electrical potential of particles. In their study, the change in zeta potential values was examined with different types of ions in solution. They conclude that while NaCl and LiCl salts cause higher zeta potential readings than water measurements, divalent cations such as Ca^{2+} and Mg^{2+} and heavy metal ions like Cu^{2+}, Co^{2+}, and Pb^{2+} yield a decrease in zeta potential values. Kaya et al. (2003) investigated the settling behavior of kaolinite in an aqueous solution by relating it to the zeta potential measurements. Their results show a good correlation between zeta potential and settlement properties of sediment. Increasing zeta potential causes thinner sediment thickness. Hussain et al. (1996) focus on the zeta potential of kaolinite, illite, and chlorite to investigate their effects on coal flotation. According to their results, kaolinite clay is the most negatively charged clay type when compared with illite and chlorite.

Nasralla and Nasr-El-Din (2011) conducted a study to better understand the role of electrical surface charges on the success of low-salinity waterflooding. Oil/brine and solid/brine interfaces are the scope of their study. They conclude that the type of cations existing in water has more effect on waterflooding oil recovery efficiency than salinity of water. Alotaibi and Nasr-El-Din (2011) focus on electrokinetic properties of crude oil and limestone particles in saline solutions. They used different salinity values and different types of cations in the water solution. Their study reveals that the zeta potential of oil droplets and solid/brine suspensions are closely related to wettability of rock. Quan et al. (2012) conducted a study on ions matching waterflooding focusing on electrical surface

charges and wettability alteration during ion-matching waterflooding. They measured oil/brine, kaolinite/brine, illite/brine, chlorite/brine, montamorillonite/brine, and quartz/brine zeta potentials. One of their conclusions is that water-wet interfaces have high negative zeta potential values, indicating an increase in electrical double layer force, as well as increasing disjoining pressure.

Jiang et al. (2010) studied the effect of kaolinite zeta potential on wettability alteration characteristics of diluted bitumen emulsion separation. They conclude that changing the zeta potential of kaolinite by using silicate and pH control yields a wettability change of clay solids, which can enhance the water-diluted bitumen emulsion separation. Liu et al. (2002) propose a new technique to study bitumen-clay interactions in aqueous solutions by using zeta potential distribution measurements to better understand the effect of kaolinite and montamorillonite clays on bitumen during oil sands ore-processing operations. They observed a much weaker coagulation between the kaolinite and bitumen than the montamorillonite-bitumen pair. Shuhua and Jialin (1997) studied three different oil sand deposits that were oil-wet, water-wet, and mixed-wettability. The zeta potential results of this study support the theory that negative charge and repulsive force are present at the bitumen and sand surfaces.

Parra-Barraza et al. (2003) conducted an analysis to better understand the surface properties of asphaltenes, including zeta potential analysis. Their results suggest that cationic and anionic surfactants can be good candidates to control crude oil dispersions.

1.4 Relative Permeability

Relative permeability is "*a direct measure of the ability of the porous system to conduct one fluid when one or more fluids are present. These flow properties are the composite effect of pore geometry, wettability, fluid distribution, and saturation history.*" (Anderson, 1987).

Mungan (1972) mentions the importance of using reservoir fluids and preserved cores rather than refined fluids and restored-state cores. Because using restored cores and refined fluids yields wrong results, it is suggested to use original oil and preserved core samples in relative permeability measurements. However, some of the relative permeability measurements were done using restored-state cores and refined fluids to obtain more homogeneous samples for more consistent results.

If experimentally determined relative permeability curves are missing, there are several correlations in the literature proposed for the prediction of three-phase relative permeability curves by using two-phase data or the saturation/capillary pressure relationship. The models of Stone, Hirasaki, Corey et al., Naar and Wygal, Land, Aleman, and Parker et al. are some of these correlations. There are also saturation-weighted interpolation and true-linear interpolation models, except from the models mentioned above (Baker, 1988).

1.4.1 Wettability Effect on Relative Permeability Curves

There are several studies that reveal the direct relationship between wettability and relative permeability curves. Anderson (1987) states that relative permeability is affected by wettability because wettability influences the location, flow, and distribution of fluids

in a porous medium. Frizzell (1990) enhances this explanation by mentioning that fluid distribution is one of the controlling parameters of relative permeability and is dominantly controlled by wettability. Wettability also directly influences relative permeabilities with interrelated rock properties such as grain shape, distribution, surface area, and orientation. Reservoir wettability is a complex and important parameter because it affects the flow behavior of reservoir fluids. If reservoir wettability is investigated properly with contact angle, imbibition, relative permeability, and displacement tests, it gives valuable information about the possibility of changing wettability with chemicals to increase oil recovery efficiency (Mungan, 1981).

In the study of Treiber and Owens (1972), they gathered wettability and flow data from 50 oil-producing reservoirs around the world. According to them, both contact angle and flow test results give confident results for determining reservoir wettability. Pollkar et al. (1989) conducted experiments to determine the steady-state relative permeabilities of Athabasca bitumen and water in resaturated sand packs. They give a comparison of heavy-oil–water normalized relative permeability curves for several Canadian heavy oil fields. The results of their measurements indicate concave water and convex bitumen relative permeability curves, which could be the reflection of heavy-oil recovery by hot water injection (HWI).

Owens and Archer (1971) prepared five different fluid samples, four of them obtained by mixing refined oil and various amounts of barium dinonyl naphthalene sulfonate (BDNS); the last fluid sample was prepared by stirring a small amount of detergent in the water phase. They compared relative permeability curves of each sample

with different contact angle values and note that a decrease in water wettability causes a decrease in relative permeability to oil and an increase in relative permeability to water. McCaffery and Bennion (1974) point out the relationship between relative permeability curves and contact angles. They used polytetrafluoroethylene (PTFE) and various pure fluids (nitrogen, n-heptane, n-docane, dioctyl ether, α-bromonaphthalene, ethylene glycol, and water) to control uniform wetting behavior during their experiments. They obtained contact angle measurements for wettability determination and relative permeability behavior were investigated by using the Penn State steady-state method. Their results are in good agreement with the results of Owens and Archer (1971). Anderson (1987) comprehensively studied the relationship between wettability and relative permeability. In this study, he outlines some important points concerning the effect of wettability on relative permeability curves. If a core becomes more oil-wet, the effective oil permeability at IWS decreases. Varying from water-wet to oil-wet wettability behavior causes a decrease in the effective oil permeability at initial water saturation. Also, oil relative permeability decreases while water relative permeability increases in an increasingly oil-wet environment. Anderson also mentions Craig's published study on the several rules of thumb indicating relative permeability characteristics of strongly water-wet and strongly oil-wet cores. **TABLE 3** shows these rules of thumb (Anderson, 1987).

TABLE 3—CRAIG'S RULES OF THUMB (Anderson, 1987; Craig, 1976)

	Water-Wet	Oil-Wet
Interstitial water saturation	Usually greater than 20 to 25% pore volume (PV)	Generally less than 15% PV, frequently less than 10%
Saturation at which oil and water relative permeabilities are equal	Greater than 50% water saturation	Less than 50% water saturation
Relative permeability to water at the maximum water saturation (based on the effective oil permeability at reservoir interstitial water saturation)	Generally less than 30%	Greater than 50% and approaching 100%

Another study points out the importance of making independent wettability measurements without relying only on Craig's rules of thumb to evaluate wettability (Rao, 2002). In this study, Rao obtains dual-drop-dual-crystal (DDDC) contact angle measurements and checks relative permeability curves obtained from dynamic displacement tests for 10 rock-fluid systems. Although the results of this study point out that Craig's rules work for 8 out of 10 rock-fluid systems, rules of thumb should also include the endpoint relative permeability at connate water saturation and wettability relationship (Rao, 2002).

1.4.2 Relative Permeability Endpoints and Temperature

Several factors influence relative permeability, such as absolute permeability, fluid viscosity, and temperature. Although most researchers agree on the effects of permeability and viscosity, there is still a continuing debate on the effect of temperature on relative permeability curves (Frizzell, 1990).

Some researchers claim that there is no direct relationship between temperature and relative permeability curves. Polikar et al. (1986) conducted 25 experiments with Athabasca bitumen, deionized water, and sand packs to determine the effect of temperature on relative permeabilities and saturation endpoints. They claim that endpoint relative permeabilities are independent of temperature (below 200 °C). Sufi et al. (1982) conducted experimental studies on the impact of temperature on oil-water relative permeabilities. Their results show that there is no relationship between temperature and relative permeability endpoints. They conducted their experiments with distilled water and white mineral oil, with a temperature range between 21 and 86 °C.

On the other hand, a number of researchers show the relationship between relative permeability curves and temperature experimentally (Closmann et al., 1988; Maini and Okazawa, 1987; Poston et al., 1970). Maini and Okazawa (1987) investigated the effect of temperature on relative permeability curves of sand. They used heavy crude oil and deionized water in their unsteady-state technique experiments. They combined several experimental studies on temperature effect on relative permeability without any consensus on how temperature affects each parameter. According to their conclusions, water relative permeability can change significantly with temperature. Leverett (1939) studied flow behavior of oil-water mixtures in unconsolidated sand formations and proposes a relative permeability curve representing these formations. Closmann et al. (1988) worked on tar/water relative permeabilities of Peace River cores and investigated the temperature effect on relative permeability curves. They used three different types of Peace River tar: thermally altered tar, unaltered tar, and deasphalted tar. They show that relative

permeability of unaltered Peace River tar (extracted using methylene chloride) is shifted toward low water saturation at 196 °C when compared with the Leverett curve. Poston et al. (1970) focused on irreducible water saturation and relative permeability of unconsolidated sands with several experiments to inspect their relationship with temperature. They point out that IWS rises with increasing temperature, practical ROS (residual oil at 100:1-producing water cut) is negatively affected by increasing temperature, and both oil and water relative permeabilities usually increase with rising temperature.

Frizzell (1990) analyzed 15 years of thermal laboratory data in order to find a correlation between relative permeability and saturation endpoints for heavy oils. According to the results of this study, ROS to water, gas, and steam decreases with increasing temperature, IWS increases with rising temperature, and effective permeability to gas at residual oil increases with increasing temperature. Another study, which is similar to Frizzell's research, was conducted with the only difference being that core samples were from western Canadian unconsolidated bitumen-producing formations. Bennion et al. (2006) present two different average relative permeability curve correlations for low-temperature (between 60 and 100 °C) and high-temperature (between 150 and 275 °C) cases. The results of this study claim that increasing temperature causes a decrease in ROS and an increase in water endpoint relative permeability.

Nakornthap and Evans (1986) reviewed most of the literature and generalize several points according to the research related to thermal oil recovery methods:

1. Increasing temperature causes a ROS decrease and an IWS increase.

2. At constant saturation, while relative permeability to water decreases, relative permeability to oil increases with rising temperature.
3. The oil/water/rock contact angle decreases as temperature increases, which shows increasingly water-wet behavior with increasing temperature.

TABLE 4 shows some of the relative permeability studies conducted to analyze the effect of temperature on relative permeability curves. All of the studies investigated water-oil relative permeability curves and their temperature dependences. There is a consensus on the temperature effect on IWS and ROS. Almost all the studies agree on the fact that increasing temperature will cause an increase in IWS and a decrease in ROS. On the other hand, all the published works propose different conclusions about the temperature effect on relative permeability endpoints.

TABLE 4—STUDIES FOCUSING ON TEMPERATURE EFFECT OF RELATIVE PERMEABILITY (After Maini and Okazawa (1987))

				Temperature Effects						
Oil Type	Rock Type	Core Type	Temperature Range, °C	IWS	ROS	Endpoint Relative Permeability to Oil	Endpoint Relative Permeability to Water	Measurement Technique	Reference	Year
Bitumen	Sand	Clean	125–250	No change	No change	No change	No change	Steady-state	Polikar et al.	1986
N-dodecane	Berea sand	Fired	22–175	Increased	Decreased	Increased	Decreased	Steady-state	Torabzadeh and Handy	1984
Mineral oil	Sand	Clean	21–149	No change	No change	No change	No change	Unsteady-state	Miller and Ramey	1985
Heavy crude		Preserved	27–220	Increased	Decreased	Decreased	Increased	Unsteady-state	Bennion et al.	1985
Heavy crude	Sand	Preserved	23–272	Increased	Decreased at first then increased	Decreased	Independent	Unsteady-state	Maini and Batycky	1985
Mineral oil	Sand	Clean	21–86	No change	No change	No change	No change	Unsteady-state	Sufi et al.	1982
Mineral oil	Boise sandstone		27–79	Increased	Decreased			Unsteady-state	Weinbrandt et al.	1975
Mineral oil	Berea sand and porous teflon		25–100	Increased	Decreased			Steady-state	Lo and Mungan	1973
Refined oil	Sand	Unconsolidated	24–140	Increased	Decreased			Unsteady-state	Poston et al.	1970
Heavy crude	Ottawa sand	Unconsolidated	25–200					Unsteady-state	Maini and Okazawa	1987
Refined oil/ crude oil	Berea sand	Consolidated	24–260/ 24–149		Decreased			Unsteady-state	Edmondson	1965
Refined oil	Bandera sandstone, Barea sandstone, limestone	Consolidated	21–163	Increased	Decreased			Unsteady-state	Sinnokrot et al.	1971
Bitumen	Silica sand, oil sand samples	Unconsolidated	100–250			No change	No change	Steady-state/ unsteady-state	Polikar et al.	1990

1.5 Asphaltenes

Asphaltenes are the heaviest component of crude oil which cause several problems in petroleum industry (Hematfar et al., 2013). They can be defined as complex molecules which are insoluble in low molecular weight n-alkanes and can be found in petroleum, coal or shale oil (Kokal and Sayegh, 1995). Although asphaltene molecular structure may vary for each different sample, its composition mainly includes fused aromatic rings with alkane chains. Aromatic rings can also contain heteroatoms such as sulfur, nitrogen, oxygen, vanadium, and nickel (Akbarzadeh et al., 2007).

Crude oil fractions including asphaltenes can be obtained by following ASTM procedure D-2007. The fractions of crude oil (saturates, aromatics, resins, and asphaltenes) can be separated on the basis of polarity and solubility differences of the oil constituents by following the ASTM procedure (Crocker and Marchin, 1988).

The adsorption of asphaltenes on mineral surfaces are controlled by several factors (Kokal and Sayegh, 1995): structural and chemical nature of the mineral surface, the asphaltene and resin content of the crude oil, brine composition and pH, pressure, and temperature. Dubey and Waxman (1991) investigated adsorption of asphaltenes on various clays, and they used tar-sand-derived asphaltene, which was n-pentane insoluble, for their studies. They found that the highest asphaltene adsorption was achieved for illite (Beavers Bend, OK).

1.6 Numerical Simulation

Numerical simulation is a powerful tool widely used by reservoir engineers in order to simulate challenging and complex reservoir systems. The reliability of a numerical simulation depends on the quantity and quality of input parameters. Even if each parameter is input in numerical simulation, the simulator results could be insufficient due to lack of built-in mathematical equations to represent every physical phenomenon. Because of this reason, the results of numerical studies have to be checked with experimental and field operation data. This process is called history-matching, and it is essential to increase the reliability of the numerical simulation.

Relative permeability curves are very important for numerical simulations because the difference in shape and endpoint saturations significantly affect the production and flow behavior of the simulated reservoir. There are several relative permeability studies, some of which focus on the relative permeability and temperature relationship from the perspective of numerical simulation. Bennion et al. (1985) investigated the changes in relative permeability endpoints by temperature. They used both preserved and restored cores for their relative permeability measurements. They provided the results of the measurements to Computer Modelling Group Ltd.'s (CMG's) thermal simulator and found that preserved core results give a better match to the field water cut curve. In addition, an increase in temperature causes a decrease in both the residual saturation and the relative permeability to oil at the IWS. On the other hand, the endpoint relative permeability to water increases with increasing temperature. Tamim et al. (2000) introduce recent improvements in thermal numerical simulation techniques and

extensively discuss temperature effects on relative permeability. They point out the importance of three-phase relative permeability in numerical simulation, as well as the proven effect of temperature on water-oil relative permeability endpoints. Li and Horne (2003) propose a numerical simulation method without relative permeability inputs. They use capillary pressure data instead of relative permeability curves. The results of the numerical simulations without relative permeability functions are almost same with experimental data. In discussing part of their study, they point out that if capillary pressure is negligible in a system, linear relative permeability curves can be used in numerical simulation models. Bahlani and Babadagli (2008) point out that most SAGD numerical simulation studies in literature do not include relative permeability change with temperature, which yields conservative numerical simulation results when compared with field data. There are also some numerical simulation studies focusing on the impact of relative permeability curves on SAGD performance. Sasaki et al. (2001) constructed a numerical simulation model to obtain a good match with their two-dimensional (2D) scaled physical model. They checked oil production rates, cumulative oil production, steam chamber volume, and temperature distribution results of both physical and numerical models. One result of their study is that non-zero endpoint saturations give a good match, while zero endpoint saturations for linear and nonlinear relative permeability curves do not provide good agreement. This result contradicts the results of Chow and Butler (1996). Lei et al. (2010) numerically studied the impact of oil-water relative permeability curves on SAGD performance. They used the previously history-matched oil-water and gas-oil relative permeability curves of Good et al. (1997) and did several

sensitivity runs to better understand the effect of oil-water relative permeability endpoints. They conclude that the endpoints of oil-water relative permeability curves highly affect the SAGD recovery factor and steam-oil ratio.

There are also quite a few attempts to numerically determine wettability change for steam processes. Yuan et al. (2002) conducted a simulation study to investigate wettability change near the production well and its positive impact on SAGD performance. They separated relative permeability and capillary pressure curves for each of the oil-wet and water-wet reservoir sections. Hascakir and Kovscek (2010) prepared a field-scale CSS simulation study to examine thermally induced wettability alteration. They questioned the temperature impact on wettability by interrelating it with relative permeability endpoints.

Although SAGD is a relatively new thermal recovery method, there are some field-scale SAGD numerical simulation studies. Souraki et al. (2012) investigated SAGD performance parameters numerically with several experimental analyses, such as compositional analysis, density, viscosity, and interfacial tension measurements. They ran sensitivity studies on several important parameters to understand the effect of each parameter on SAGD performance. Heron et al. (2008) conducted a numerical simulation of noncondensable gas coinjection with steam in an SAGD operation. They used methane, which is a noncondensable gas, and exchanged properties in the CMG STARS thermal simulator; the results point out that the coinjection should have intermittent intervals and steam injection should be steadily continuous. Egermann et al. (2001) introduce a methodology for SAGD performance optimization with ATHOS reservoir simulation software from the IFP group. Glandt and Malcolm (1991) conducted a numerical

simulation study for a Peace River recovery process by including four oil-phase components (high- and low-molecular-weight components, CO_2, and methane), a visbreaking reaction that reduces bitumen viscosity, and a rock-water interaction that produces CO_2. They used the THERM numerical simulator to match field data of the Peace River in-situ project and the Peace River expansion project. They obtained good history-matches for simulations of both projects.

There are also several combinations of experimental and numerical studies that improve the knowledge of process mechanisms of this method. Chow and Butler (1996) transferred Chung (1988) 2D SAGD laboratory experiment into a numerical environment. They matched simulation results with experimental data (cumulative oil production and steam interface isotherm). However, they note that the numerical simulator does not have the capability to simulate either in-situ water/oil emulsification or countercurrent flow mechanism inside the expanding steam chamber. Another laboratory-scale numerical simulation study was conducted by Ashrafi et al. (2011). The aim of their study was to investigate possible effects of solvent coinjection on the history-matched model of Chung (1988) laboratory experiment. They conclude that the optimum steam injection temperature for their model is 130 °C at 153 kPa, and steam quality has to be 90% or higher. In addition, normal hexane coinjection is a good candidate to increase SAGD performance. Yuan et al. (2003) conducted two numerical simulation studies to enhance the knowledge on the impact of gas during SAGD operations. They focused on two experiments, one prepared with dead oil and the other prepared with live oil. They history-matched both experiments with numerical simulation results from the CMG STARS

thermal reservoir simulator, and they observed gas accumulation outside the steam chamber slowing down the oil production in live oil experiment. Zhao et al. (2005) prepared a comprehensive experimental and numerical study to find an energy-efficient method for the wind-down process of an SAGD operation. They also used CMG STARS for numerical history-matching purposes. The results of this study show that more than 10% of OOIP can be recovered by noncondensable gas injection after an SAGD operation. Another laboratory-scale numerical study was conducted by Law et al. (2003) to observe top water and gas cap zone effects on the SAGD process. The laboratory experiments were prepared with top water and gas cap zones in order to mimic Athabasca oil sand reservoir properties. They also agree on the capabilities of CMG STARS for simulating SAGD experiments.

CHAPTER II

STATEMENT OF THE PROBLEM AND OBJECTIVES

Because SAGD is proven and reliable technique for in-situ bitumen extraction which ensures high oil recovery, it is one of the most popular EOR methods. However, SAGD field implementation still requires research to increase the performance of the process due to its economic and environmental challenges.

These challenges can be overcome by increasing knowledge of the process mechanism, which should be investigated both experimentally and numerically. This way, performance can be predicted in advance, and the solutions for the challenges can be produced effectively. First, experimental results should be coupled with numerical simulation to find parameters that cannot be easily obtained by conducting experiments. Historically matched experiments can then be scaled up for field-scale performance determination.

In this study, three SAGD experiments are simulated with a reservoir simulator to estimate relative permeability changes with temperature and reservoir rock type. Rock wettability is an important parameter influencing the recovery efficiency of EOR methods. However, wettability change hasn't been investigated extensively for SAGD-applied reservoirs and experiments. The spent rock samples of the experiments show varying wettability characteristics, which are needed as input data in a numerical model. Thus, temperature-dependent relative permeability endpoints are adjusted according to the experimental oil recovery and temperature propagation obtained in all three experiments.

The objectives of this study are as follows:

- To investigate the impact of wettability change with the change in injected fluid temperature on SAGD performance.
- To investigate the impact of clay type on wettability change during SAGD.
- Developing and tuning temperature-dependent relative permeability endpoints by using post experimental wettability analyses to better represent a physical model in a numerical environment.
- Coupling experimental results on surface and interfacial tension measurements with three SAGD experiment results to obtain relative permeability changes with temperature and clay type numerically.

CHAPTER III

EXPERIMENTAL STUDIES

3.1 Experimental Procedure

Wettability change is investigated for two SAGD experiments and one HWI experiment. All three experiments were conducted with a 2D physical SAGD model, which is shown in **Fig. 5.**

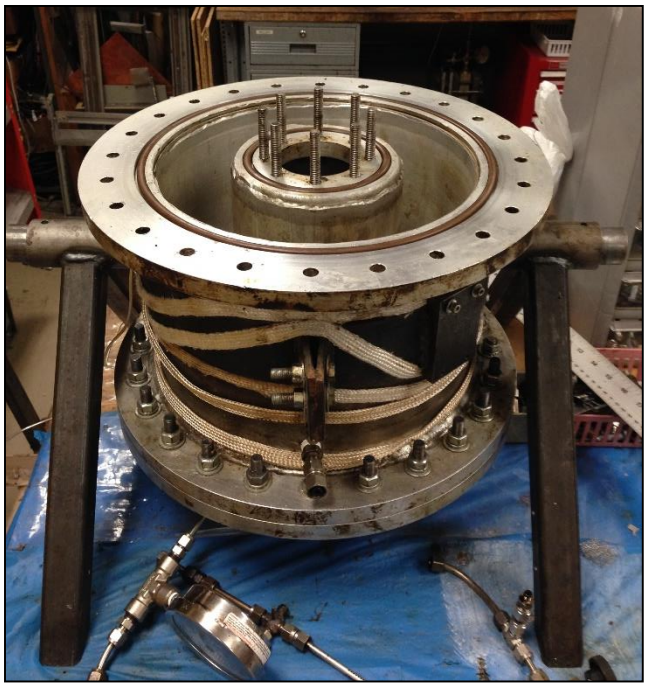

Fig. 5—2D physical SAGD model.

All three experiments were conducted at 75 psig. Reservoir rocks were simulated by mixing 85-wt% Ottawa sand and 15-wt% clay, which corresponds to 32% porosity.

Pore space was filled with 84-vol% Peace River bitumen and 16-vol% distilled water (Hamm and Ong, 1995). Among these three experiments, temperature and clay type were varied to investigate the impact of injection temperature and clay type on wettability change.

The first experiment (HWI) was conducted at 155 °C, which yields hot water at 75-psig experimental pressure (Fig. 6 – red dot).

The second experiment (SAGD1) was conducted at 165 °C, which maintains steam injection at experimental pressure (Fig. 6 – green dot).

The third experiment (SAGD2) was conducted at 165 °C by preparing the oil sand sample with different clay type (Fig. 6 – green dot).

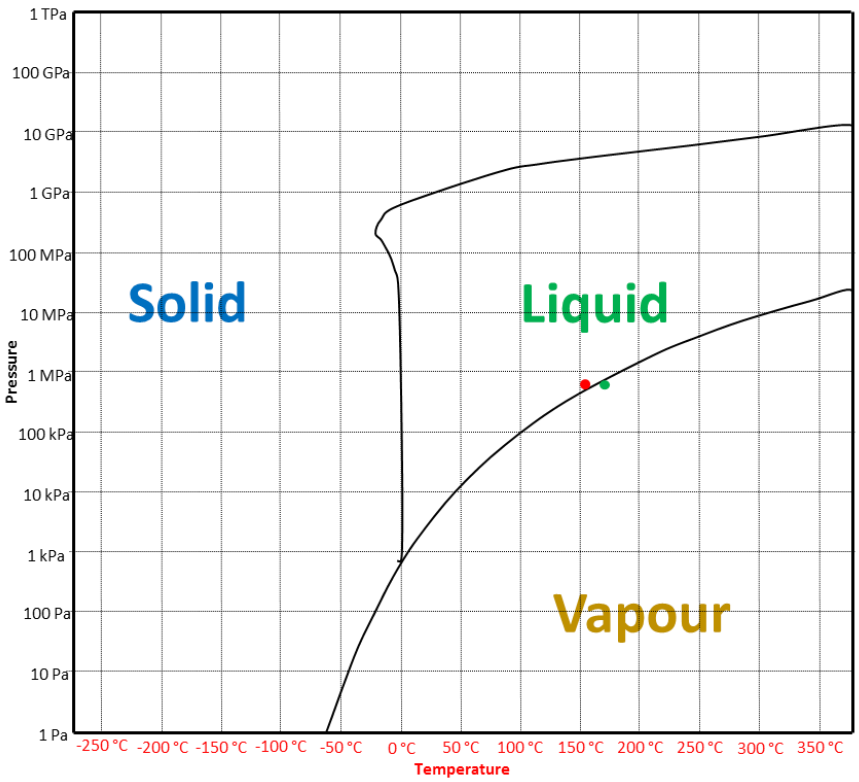

Fig. 6—Water phase diagram and injected fluid phases at experimental conditions.

The performance of the first and the second experiments was investigated for the effect of injection temperature. The second and the third experiments were conducted to understand the effect of different clay types on SAGD performance.

Thus, in the first and second experiments, the only variable was the injection temperature of water and all other initial and experimental conditions were the same. In the second and third experiments, the only variable was clay type and all other initial and experimental conditions were kept constant. For the first and the second experiments, clay type 1, which has mainly kaolinite in its composition, was mixed with the Ottawa sand, and for the third experiment, clay type 2, which has both kaolinite and illite, was mixed initially with the Ottawa sand for the preparation of the rock samples. X-ray diffraction (XRD) results of clay types 1 and 2 are shown in **Fig. 7** and **Fig. 8.** The red curves are the XRD traces of clay types 1 and 2, the blue curve is reference values of quartz mineral, the gray curve is kaolinite, and the green curve is illite.

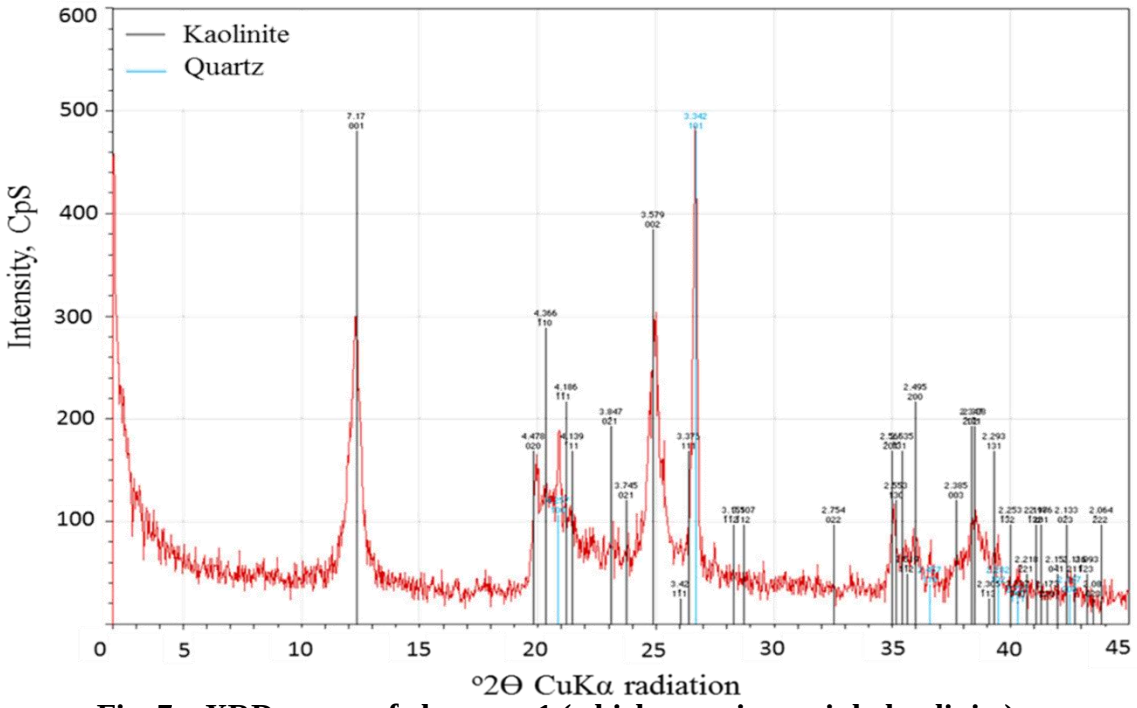

Fig. 7—XRD traces of clay type 1 (which contains mainly kaolinite).

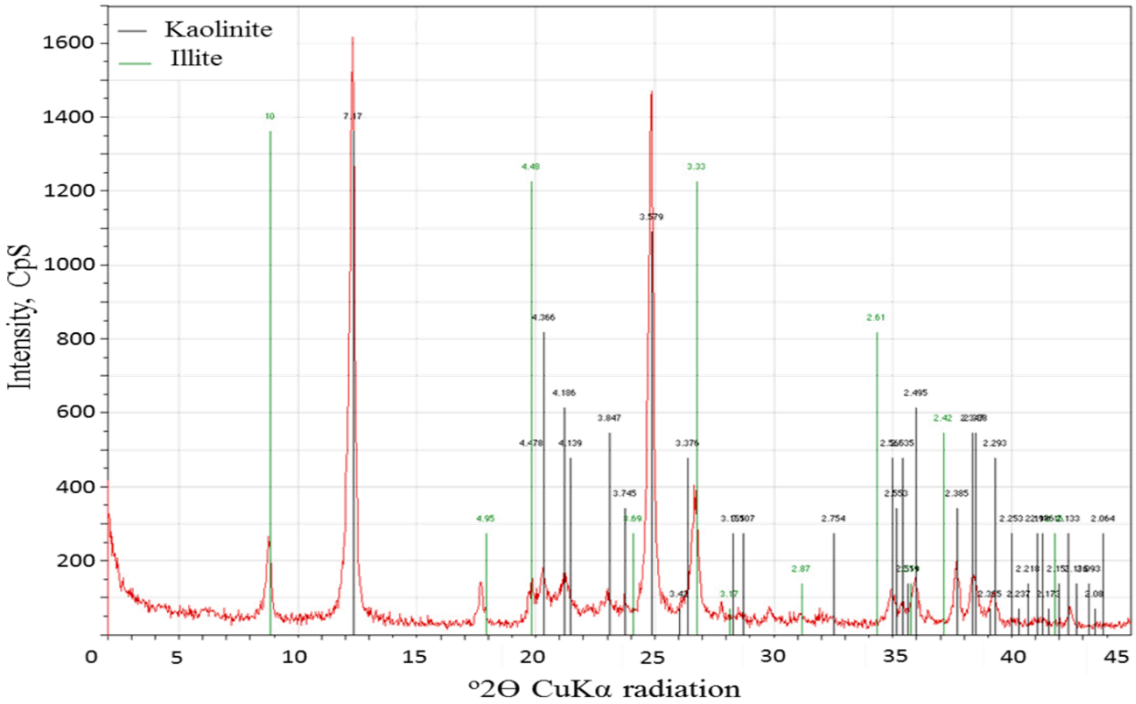

Fig. 8—XRD traces of clay type 2 (which contains mainly kaolinite and also 10% illite).

Note that Peace River reservoir rock contains both illite and kaolinite; therefore, clay type 2 better represents the reservoir rock clay (Bayliss and Levinson, 1976). **TABLE 5** summarizes the variables for each experiment.

TABLE 5—INITIAL CONDITIONS OF EXPERIMENTS

Experiment Name	Clay Type	Injection Temperature	Experimental Pressure
HWI	Clay type 1	155 °C	75 psig
SAGD1	Clay type 1	165 °C	75 psig
SAGD2	Clay type 2	165 °C	75 psig

The greatest oil recovery (47.4 wt%) is observed for the SAGD1 experiment among these three experiments. The second successful experiment is HWI, with almost 33-wt% oil recovery. Although SAGD2 was a steam injection process and was expected to recover more oil than the HWI case, it has the least oil recovery was obtained for this experiment (32 wt%) (Mukhametshina, 2013).

A later section analyzes the results obtained from HWI and SAGD1 experiments to develop an understanding of wettability change with temperature, and SAGD1 and SAGD2 experimental results are investigated to explain the mechanism of clay-bitumen-steam interactions. The experimental analyses on produced oil, water, spent rock, original rock, clay, and bitumen samples were conducted with contact angle, zeta potential, interfacial/surface tension, residual fluid saturation, and XRD measurements. SEM images were used to visualized the change in the surface and pore structures. Results of the experimental studies were later used to develop relative permeability curves to obtain a representative numerical model.

3.1.1 Contact Angle

Kruss DSA30S (**Fig. 9**) was used to conduct contact angle measurements of oil sand samples. This device works with drop shape analyzer software (DSA3) to measure the surface properties of materials by analyzing video images of liquid drops. This device has a contact angle measuring range from 1 to 180^{o}, and the measurement resolution is a 0.1^{o} angle.

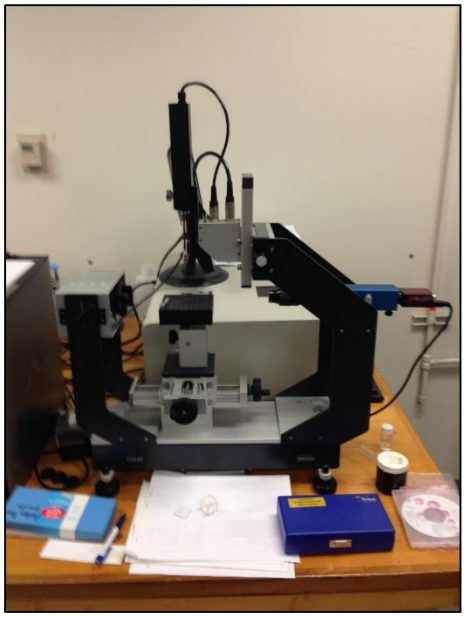

Fig. 9—Kruss DSA30S drop shape analyzer.

The procedure to conduct contact angle measurements is explained step by step as follows:

The oil sand samples are flattened by using 1- × 1-in. glass plates before starting each measurement. The DSA30S syringe and Popper pipetting stainless steel needle (14 × 4 in.) are used to drop distilled water on the flattened sample. The drop shape is captured through video recording while the water droplet is dropped to the surface. DSA3 software is used to measure contact angle. The software gives a graph showing the time-dependent change of contact angle values. Static contact angle values are obtained by using the mean values of stable sections of each graph.

3.1.2 Zeta Potential

The Brookhaven Instruments Corporation (BIC) ZetaPALS zeta potential analyzer device (**Fig. 10**) was used for zeta potential measurements of bitumen, produced oil, produced water, sand, clay, asphaltene, and postmortem oil sand samples. PALS stands for phase analysis light scattering and is the extended version of electrophoretic light scattering (ELS). This device simply measures the velocity of particles affected by a known electric field and then calculates mobility and zeta potential from this information.

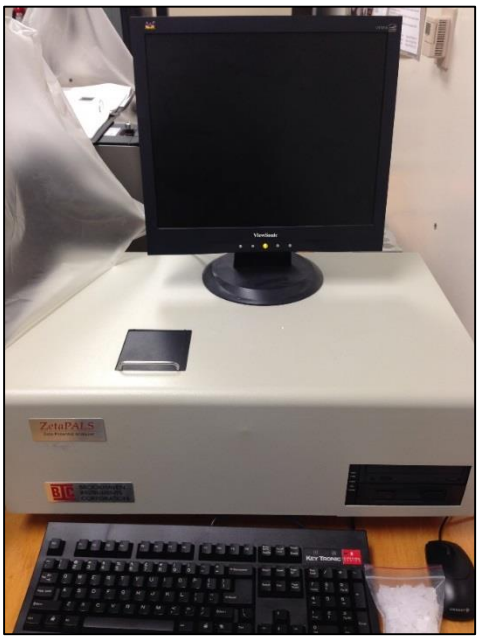

Fig. 10—BIC ZetaPALS zeta potential analyzer.

The list of the equipment used in zeta potential measurements is given below:

- Magnetic stirrer (Corning PC-4200)
- Ultrasound tub (Cole Parmer instruments)

- Centrifuge (Damon IEC HN-SII)
- High-speed blender (Silverson L4RT)
- pH meter (Oakton)
- Total dissolved solids (TDS) meter (Oakton)
- Zeta potential analyzer (BIC ZetaPALS)
- Particle size analyzer (BIC 90Plus)
- Plastic cuvettes (BIC BI-SCP)

Suspension and emulsion samples for zeta potential measurements have to be carefully prepared before each zeta potential measurement to obtain a stable colloidal system, which gives repeatable zeta potential measurements. KCl is used as a supporting electrolyte for all zeta potential measurements.

Sand Sample Preparation: 5 g of sand is ground for 10 minutes using a pestle grinder to obtain a fine powder (5- to 10-μm diameter). Approximately 10 mg of the powder is transferred to a 100-mL aqueous solution containing 1 mM of KCl, and a magnetic stirrer is used to prepare suspension in a shorter time (Shuhua and Jialin, 1997).

Clay Sample Preparation: Approximately 10 mg of clay powder is transferred into 100 mL of an aqueous solution containing 1 mM of KCl, and 15 minutes of magnetic agitation is applied for each sample (Yukselen and Kaya, 2003).

Bitumen Sample Preparation: 1 g of bitumen is placed in 100 mL of 1-mM KCl solution, and a high-speed electric blender is used to make an emulsion for 15 minutes at 80 °C. After waiting 3 hours, samples cool down to room temperature, and 10 mL of the

emulsion is diluted with 90 mL of 1-mM KCl solution to obtain an emulsion containing about 0.01 to 0.1 wt% of bitumen (Liu et al., 2002).

Asphaltene Sample Preparation: 50 mg of asphaltene is mixed with 15 mL of ethanol; this mixture is homogenized with an ultrasound tub. After 20 minutes of ultrasound treatment of the sample, 1.5 mL of it is added to 100 mL of 1-mM KCl solution (Parra-Barraza et al., 2003).

Clay-Asphaltene Mixture Sample Preparation: Asphaltene and clay weight percentages in original oil sand samples are used to prepare a 10-mg sample. Asphaltene (2.8 mg) is mixed with 7.2 mg of clay; this mixture is transferred into 100 mL of an aqueous solution containing 1-mM KCl, and 15 minutes of magnetic agitation is applied for each sample (Yukselen and Kaya, 2003).

Produced Water Sample Preparation: Produced water samples are used without any preparation to check their properties after the experiments.

Postmortem Sample Preparation: First, postmortem samples are cleaned from bitumen by using toluene. Then, 5 g of postmortem sample is ground for 10 minutes using a pestle grinder to obtain a fine powder. Approximately 10 mg of the powder is transferred to 100 mL of aqueous solution containing 1-mM KCl, and a magnetic stirrer is used to prepare suspension in a shorter time (Shuhua and Jialin, 1997).

Each of the prepared samples for zeta potential measurements is subjected to pH, TDS, and particle size measurements as well.

Zeta potential results for each sample are obtained by using statistical methods. For each cuvette, five runs of measurements are conducted with 30 cycles (Alotaibi et al.,

2010). If the data retention value of a single run is less than 90%, the measurement is conducted again. Each sample is placed inside more than one cuvette for measuring zeta potential. The mean value of the zeta potential results of each cuvette is assigned as the zeta potential of that sample.

3.1.3 Interfacial Tension

Interfacial and surface tension measurements were conducted with the KSV Sigma 703 tensiometer (**Fig. 11**) using the Wilhelmy plate method. In this method, a thin plate, which is wetted by tested fluid, is contacted with the liquid surface, and the force applied by the fluid climbing the plate surface is measured.

Fig. 11—KSV Sigma 703 tensiometer.

For surface tension measurements, the 20 mL of oil sample is placed inside a small beaker, and the plate is wetted with the oil sample before the start of each experiment. The maximum value measured by the tensiometer represents the surface tension value of that oil sample. Interfacial tension measurements for oil samples are prepared with 20 mL of the oil sample, which is placed into the beaker. Then, 20 mL of the distilled water sample is poured onto the oil sample. The same procedure as the surface tension measurement procedure is followed for interfacial tension measurements. These measurement procedures were obtained from the device manual.

For each sample, three measurement runs of surface tension (tension between oil and air) and three measurement runs of interfacial tension (tension between oil and distilled water) were conducted, and the mean value of these three runs was assigned as a final surface/interfacial tension value of the sample. This procedure statistically produces more reliable results.

3.1.4 Residual Oil and Water Saturations

The residual oil and water saturations are important parameters to classify the efficiency of the recovery process. Postmortem samples were divided into two regions. One of the regions was defined as near injection well, and the other region was far away from the injection well.

Because postmortem samples were wetted with steam, postmortem residual water was determined first. Postmortem samples taken from different regions, near and away from the injection well, were kept under a hood for 24 hours, and the samples were weighed before and after they dried, with the difference in weight assumed to be residual

water. Residual water saturations (RWS) were calculated using the proportionality between mass of water and saturation of water inside the oil sand sample prepared for experiments.

The postmortem samples in which water was removed were used to determine the residual oil. These samples were subjected to toluene for 5 days and then filtered through a 1-μm-size filter paper. This procedure was determined according to personal communication with KT GeoServices. The weight difference before and after treatment of toluene is the residual oil. ROSs are calculated using the proportionality between oil mass and oil saturation before the oil sand sample experiment. Note that asphaltenes are soluble in toluene, so for this methodology it is assumed that most of the oil has been removed from the rock surface.

$$RWS = \frac{[M_{wr}] \times [IWS]}{[M_{wmb}]}$$

M_{wr}: Mass of water removed from the sample

IWS: Initial water saturation

M_{wmb}: Initial mass of water inside the sample calculated using mass balance

$$ROS = \frac{[M_{or}] \times [IOS]}{[M_{omb}]}$$

M_{or}: Mass of oil removed from the sample

IOS: Initial oil saturation

M_{omb}: Initial mass of oil inside the sample calculated using mass balance

3.1.5 XRD Measurements

XRD analysis is one of the most common methods used to determine the mineral content of rock samples. The solid sample is exposed to X-rays with fixed intensity and wave length. Because the reflection angle of each mineral has a unique behavior, intensity analyses provide information on the possible identity matches.

Two original clay types (clay type 1 and 2), clay type 2 (which was exposed to steam for 6 hours), and postmortem samples gathered from around the injection wellbore region for SAGD1 and SAGD2 experiments were analyzed with XRD measurements. The main purpose of these analyses were to observe clay alteration due to interactions of clay with only steam and both steam and bitumen during steam injection processes. The XRD measurements of postmortems originated from SAGD1 and SAGD2 experiments were conducted by KT GeoServices with the Siemens D500 X-ray diffractometer, and the original clays and steamed clay type 2 were measured at Texas A&M University in on campus facilities with the Bruker D8 Advance X-ray diffractometer.

3.1.6 SEM Images

It is a common practice to inspect rock samples at the pore scale with an SEM. These images give idea about the mineralogical and physical changes on rock sample (Clelland and Fens, 1991).

SEM has been used since the late 1950s; this type of microscope uses electrons instead of light to form images. Because the SEM needs vacuum conditions to capture an image, special sample preparation is essential.

First, all the water content has to be removed from samples. Although conductive materials do not need any special preparation, nonconductive materials, such as sand and clay samples, have to be covered with a thin layer of conductive material. This process was accomplished using a “sputter coater” (Rosenberg et al., 1985).

In this study, the prepared samples were placed inside the JEOL JSM-6400 SEM, and several images were captured between the magnification ranges of 25× to 3,000×.

3.2 Experimental Results

3.2.1 Contact Angle

Contact angle measurements on original oil sand samples and postmortem samples from HWI, SAGD1, and SAGD2 experiments were done using the sesslie drop technique.

The first set of contact angle measurements was completed by measuring the contact angles of original oil sand samples prepared with two different clay types. The results for the initial samples yielded very similar contact angle values for different two clay types (**Fig. 12**).

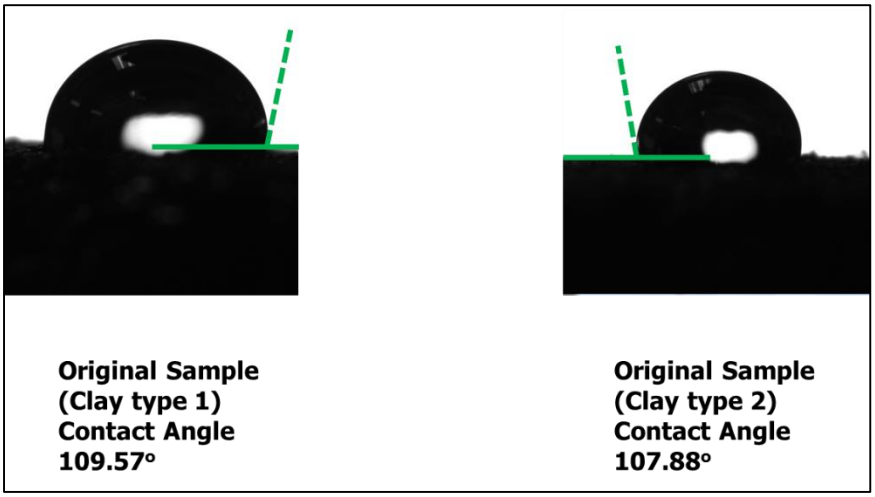

Fig. 12—Contact angle comparison for original oil sand samples before SAGD1 (left) and SAGD2 (right) experiments.

For the contact angle measurements on postmortem samples, postmortem samples were divided into several zones according to the hot water/steam injection point. The HWI experiment was divided into two regions as inside the injection zone (R1) and outside the injection zone (R2) (**Fig. 13**). As expected, R1 is much more water-wet than R2. The reason for this wettability difference is obvious: R1 was exposed to higher temperatures, and most oil production came from this region.

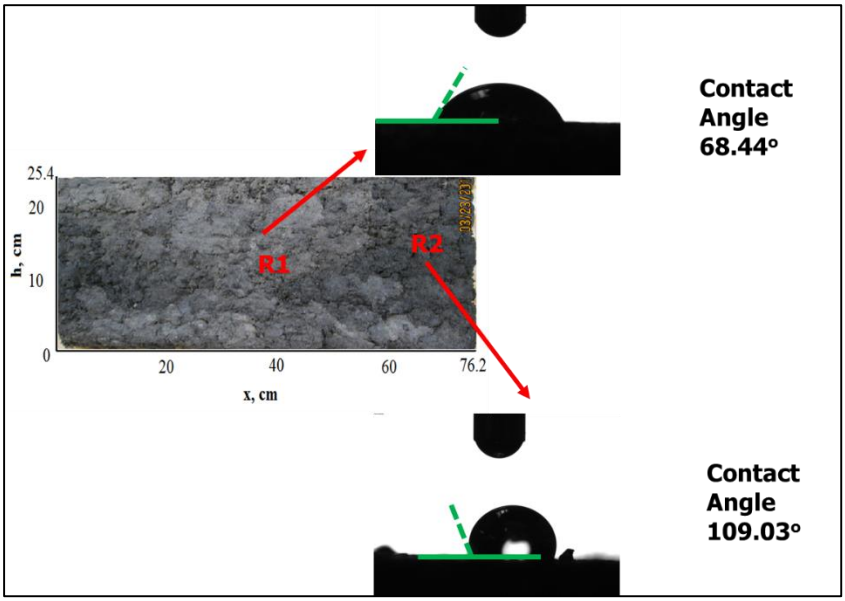

Fig. 13—Contact angle measurement results for HWI. R1: swept zone, whose contact angle measurement is provided at the top, and R2: less touched zone, whose contact angle measurement is provided at the bottom.

Another contact angle measurement set was prepared using a postmortem sample of the SAGD1 experiment. R3 represents inside the steam chamber region, and R4 represents outside the steam chamber (**Fig. 14**). A significant increase in water-wetness is observed in R3 with better sweep, and it is more water-wet than R1. This can explain the higher oil production observed with steam injection; it is also proof of increasing temperature causing increasing water-wetness.

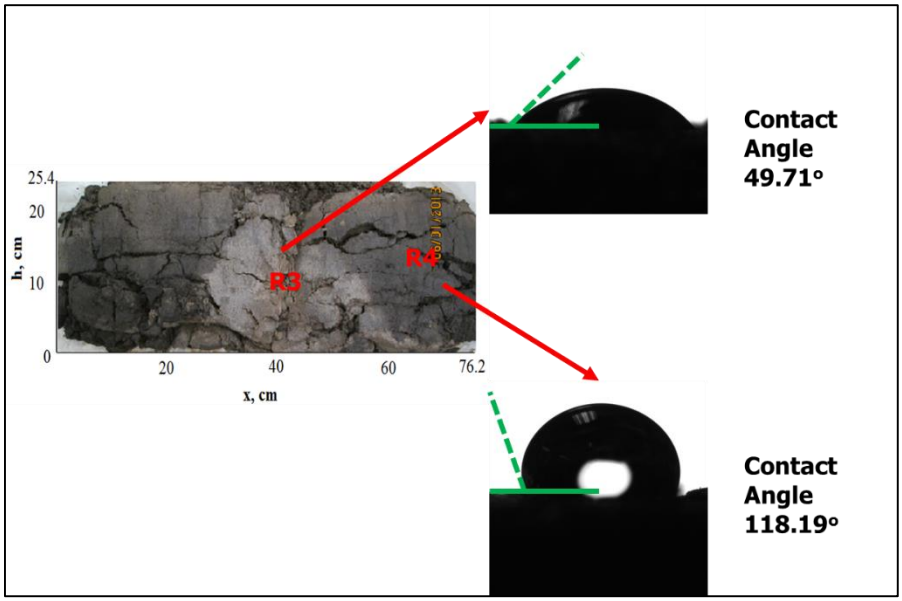

Fig. 14—Contact angle measurement results for SAGD1. R3: swept zone, whose contact angle measurement is provided at the top, and R4: less touched zone, whose contact angle measurement is provided at the bottom.

The final experimental analysis for contact angle measurements is obtained for the postmortem of the SAGD2 experiment. R5 represents inside the steam chamber zone, and R6 represents outside the steam chamber (**Fig. 15**). Although R5 is more water-wet than R6, as expected, there is a significant difference when R5 compared with R3 (compare **Fig. 14** and **Fig. 15**). Although, both experiments were conducted at the same experimental temperature and pressure conditions, the postmortem samples of the experiment conducted with clay type 2 (SAGD2) shows significantly more oil-wet behavior than the experiment conducted with clay type 1 (SAGD1). It is obvious that clay type plays an important role in the wettability characteristics of steam injection processes for bitumen extraction.

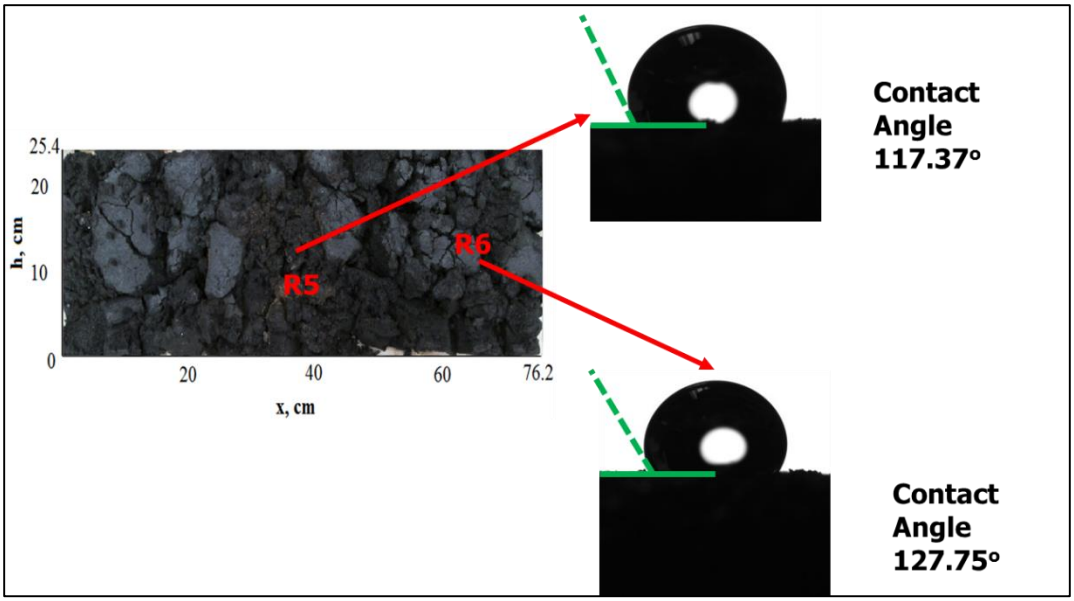

Fig. 15—Contact angle measurement results for SAGD2. R5: swept zone, whose contact angle measurement is provided at the top, and R6: less touched zone, whose contact angle measurement is provided at the bottom.

As it can be inferred from **Fig. 14** and **Fig. 15**, a significant color difference is observed between SAGD1 and SAGD2. Note that the oil sand mixture of SAGD2 was prepared with clay containing both kaolinite and illite inside. On the other hand, the clay type used in SAGD1 mostly contains kaolinite. This color difference might be due to asphaltene precipitation, which yields a darker color on the postmortem of SAGD2. Another reason for the color difference could be higher ROSs as a result of decreased effectiveness of the SAGD process, which is due to clay type. However, the effectiveness of steam chamber growth has not been influenced by clay type.

The wettability classification from literature is given with water-oil contact angle ranges. Due to the unconsolidated structure of oil sand samples and high viscosity of bitumen, it was almost impossible to do contact angle experiments inside a water

environment with oil droplets. Thus, it is essential to convert water-air contact angle values to oil-water contact angle values to use literature definitions, for determining the wettability classification of our samples (**TABLE 6**).

TABLE 6—LITERATURE DEFINITIONS FOR THE OIL-WATER CONTACT ANGLE VALUES (Alotaibi et al., 2010)

Contact Angle	Literature Definition
0 to 75˚	Water-wet
55 to 75˚	Weakly water-wet
75 to 115˚	Intermediate-wet
115 to 135˚	Weakly oil-wet
115 to 180˚	Oil-wet

Although there is a linear equation to convert water-air contact angle to oil-water contact angle using interfacial and surface tension values, which was mentioned in the literature review, it cannot be used to convert these values properly (Van Dijke and Sorbie, 2002). The most probable explanation for this is due to the fact that the results of the linear equation do not pass through the origin of the oil-water and water-air contact angle graph. Thus, some of the air-water contact angle values are out of the conversion range of this equation. Therefore, the air-water contact angle values were converted to oil-water contact angles by using the graph in **Fig. 16.** This graph was prepared for hexadecane samples, and the linear equation results were forced to pass through the origin of the graph.

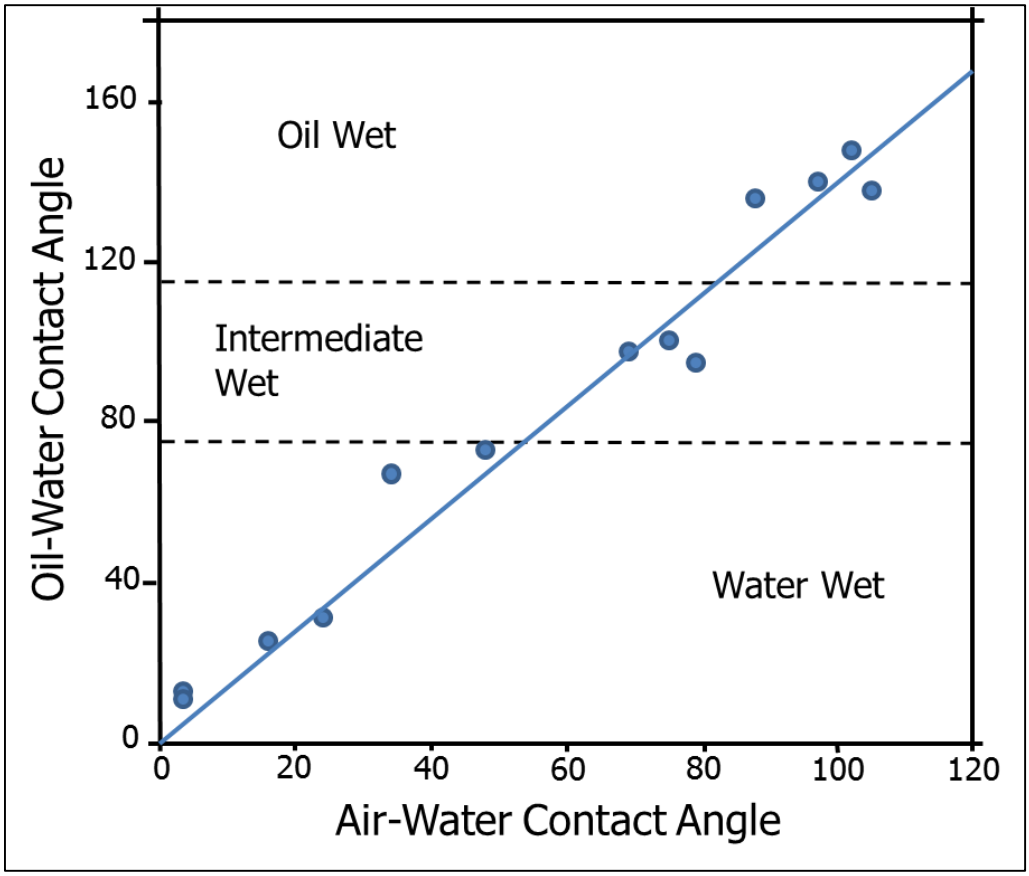

Fig. 16—Air-water contact angle to oil-water contact angle conversion graph for hexadecane, adapted from (Grate et al., 2012).

The results of the air-water to water-oil contact angle conversion and the literature wettability definition for each sample are listed in **TABLE 7.** Hot fluid injection causes water-wet behavior around the injection area. Contact angle values of R1 and R3 are in accordance with this statement. However, this behavior cannot be observed for the sample prepared with clay type 2. R5, which is also around the injection area, shows oil-wet behavior, and the only possible explanation for this change is due to clay type, because all other experimental conditions were the same for both SAGD1 and SAGD2.

TABLE 7—CONTACT ANGLE CONVERSION RESULTS AND THEIR LITERATURE DEFINITIONS FOR OIL SAND SAMPLES

Sample Name	Contact Angle (Air-Water)	Contact Angle (Water-Oil)	Literature Definition
Original oil sand sample from SAGD1	109.57	154	Oil-wet
Original oil sand sample from SAGD2	107.88	151	Oil-wet
HWI postmortem-R1	68.44	96	Intermediate-wet
HWI postmortem-R2	109.03	154	Oil-wet
SAGD1 postmortem-R3	49.71	70	Weakly water-wet
SAGD1 postmortem-R4	118.19	165	Oil-wet
SAGD2 postmortem-R5	117.37	164	Oil-wet
SAGD2 postmortem-R6	127.75	180	Oil-wet

3.2.2 Zeta Potential

Several sets of zeta potential measurements were conducted to better understand the effect of surface electrical properties of materials on wettability behavior. High zeta potential is an indication of thick water film around solid particles inside the colloid. Thus, the materials with high zeta potential values can be classified as water-wet because the water film around them is much stronger (Quan et al., 2012).

The first set of zeta potential analyses consists of reference materials that were the components of all initial samples: original bitumen, Ottawa sand, clay type 1, and clay type 2. Moreover, zeta potential was also measured for the asphaltene separated from the original bitumen with ASTM D2007-11. According to ASTM D2007-11, asphaltenes are n-pentane insoluble portion of bitumen sample. The results are provided in **TABLE 8.** According to the zeta potential values description, the reference materials can be ordered

from thickest to thinnest water layer as original bitumen, sand, clay type 2, clay type 1, and asphaltenes. The results of these measurements confirm that the water-wet property of the sand is observed with high zeta potential and the oil-wet behavior of asphaltene obtained from original bitumen is observed with low zeta potential. In addition, clay type 2 is slightly more water-wet than clay type 1, which could be explained by the water-wet behavior of illite clay (Bantignies et al., 1997). The particle size of clay type 2 is almost double that of clay type 1, which might cause clay type 2 to plug pore throats more easily. This could be the reason of production decrease observed in the SAGD2 experiment.

TABLE 8—ZETA POTENTIAL, AVERAGE PARTICLE SIZE, pH, AND TDS RESULTS FOR REFERENCE MATERIALS

Sample	Zeta Potential (mV)	Particle Size (nm)	pH	TDS (ppm)
Original bitumen	–57.09	450	5.3	70
Original asphaltene	–14.55	1504	5.6	76
Sand	–44.99	3942	5.9	70
Clay type 1	–34.89	1200	5.5	68
Clay type 2	–38.92	2300	5.5	68

A possible explanation for the particle size difference observed between bitumen and asphaltene sample is the bitumen emulsion preparation process. As mentioned previously with experimental procedures, bitumen was treated with a high-speed electric blender to produce emulsion; this process could reduce the particle size of bitumen droplets to even less than its components like asphaltene. Another possible explanation

for the observed particle size difference might be the dissolution of asphaltene particles in solution. Asphaltenes can be found dissolved in crude oil or they can be found in a colloidal suspension (Jamaluddin et al., 2002; Kokal and Sayegh, 1995). Thus, a lower particle size value was observed for bitumen than asphaltene, when asphaltene were dissolved in bitumen.

The second set of zeta potential measurements was done on produced water samples. Zeta potential results alone are not sufficient to draw any concrete conclusions, because these water samples may contain clay and bitumen in unknown concentration. However, the TDS values of them are worth investigating in detail. As can be seen from **TABLE 9,** the highest TDS value is observed in the produced water sample of SAGD1. This might be the result of the dissolution of clay type 1 minerals within injected steam and transported with produced water. Thus, the clay-free spaces created after the transportation could be the cause of high recovery observed in the SAGD1 experiment with increasing permeability by decreasing the clay content of the oil sand (Wilson, 1982). Particle sizes of clay types also support this statement. The smaller particle size of clay type 1 (1200 nm) makes it more mobile than clay type 2 (2300 nm).

TABLE 9—ZETA POTENTIAL, AVERAGE PARTICLE SIZE, pH, AND TDS MEASUREMENT RESULTS FOR PRODUCED WATER SAMPLES

Produced Water Sample Origin	Zeta Potential (mV)	Particle Size (nm)	pH	TDS (ppm)
HWI	–44.30	550	6	128
SAGD1	–34.42	1250	7.1	290
SAGD2	–52.57	370	6.1	51

The third set of zeta potential measurements was completed to check the surface charge changes on produced oil samples after the experiments. **TABLE 10** shows a negligible amount of change on produced oil sample zeta potential measurements, which means the effect of oil on observed wettability change is limited.

TABLE 10—ZETA POTENTIAL, AVERAGE PARTICLE SIZE, pH, AND TDS MEASUREMENT RESULTS FOR PRODUCED OIL SAMPLES

Produced Oil Sample Origin	Zeta Potential (mV)	Particle Size (nm)	pH	TDS (ppm)
HWI	–57.42	283	5.3	64
SAGD1	–56.74	395	5.2	69
SAGD2	–54.70	450	5.5	64

The asphaltenes obtained from original oil samples and produced oil samples of each experiment were analyzed by zeta potential measurements (**TABLE 11**). Asphaltenes obtained from the HWI and SAGD1 experiments have higher zeta potential values than the zeta potential results of asphaltene obtained from the produced oil of SAGD2. This result indicates that the asphaltene samples of experiments prepared with clay type 1 are more water-wet than the asphaltene sample obtained from SAGD2, which was prepared with clay type 2. The contact angle results on postmortem samples of these experiments are in good agreement with the same wettability characteristics for each experiments (**TABLE 7**); a possible reason for this wettability difference might be that asphaltene wettability characteristics changed for different clay types.

TABLE 11—COMPARISON OF ZETA POTENTIAL, AVERAGE PARTICLE SIZE, pH, AND TDS MEASUREMENTS OF ASPHALTENE BEFORE AND AFTER EXPERIMENT

Sample	Zeta Potential (mV)	Particle Size (nm)	pH	TDS (ppm)
Original asphaltene	–14.55	1504	5.6	76
HWI asphaltene	–18.98	1549	5.5	87
SAGD1 asphaltene	–19.20	1527	5.4	72
SAGD2 asphaltene	–11.73	1599	5.1	70

Clay type 2 was exposed to steam at atmospheric pressure for 6 hours, and the zeta potential of that clay sample was measured to check whether any surface electrical properties were changed with steam. According to zeta potential results, steam injection did not cause any changes on clay surface charges or wettability. Another test was if clay asphaltene reaction can change the wettability behavior of clay samples. To test this statement, clay types 1 and 2 were mixed with asphaltenes of produced oil originating from the SAGD1 and SAGD2 experiments, respectively. The last two rows of **TABLE 12** show the zeta potential, average particle size, pH, and TDS values of these experiments. Asphaltene addition did not cause any significant change in clay type 2 zeta potential value. However, a slight decrease in zeta potential value was observed with the addition of asphaltene in clay type 1.

TABLE 12—ZETA POTENTIAL, AVERAGE PARTICLE SIZE, pH, AND TDS MEASUREMENT RESULTS FOR CLAY SAMPLES

Sample	Zeta Potential (mV)	Particle Size (nm)	pH	TDS (ppm)
Clay type 1	–34.89	1200	5.5	68
Clay type 2	–38.92	2300	5.5	68
Clay type 2, exposed to steam for 6 hours	–38.16	2400	5.5	70
Clay type 1 + asphaltene SAGD1	–31.59	1394	5.6	69
Clay type 2 + asphaltene SAGD2	–39.00	2288	5.8	64

Finally, zeta potentials of oil sand samples after oil removal were measured to investigate the wettability properties of postmortem samples obtained from specified locations (**TABLE 13**). Initial oil sand samples not used in the experiments were also measured for comparison purpose. Because the error range of these measurements is ±4, any conclusion which would be drawn from these results might be due to either wettability change or the experimental measurement error. **Fig. 17** shows all zeta potential measurements both for reference and post experiment samples. Almost all the measurements are in the range of sand zeta potential and clay zeta potential results.

TABLE 13—ZETA POTENTIAL, AVERAGE PARTICLE SIZE, pH, AND TDS MEASUREMENT RESULTS OF OIL SAND SAMPLES

Sample	Zeta Potential (mV)	Particle Size (nm)	pH	TDS (ppm)
Original oil sand with clay type 1	–37.44	1774	5.6	78
Original oil sand with clay type 2	–37.94	1271	5.6	85
HWI postmortem (R1)	–33.85	2322	5.6	72
HWI postmortem (R2)	–38.87	1046	5.9	70
SAGD1 postmortem (R3)	–33.76	1847	5.7	77
SAGD1 postmortem (R4)	–39.37	1580	5.5	75
SAGD2 postmortem (R5)	–41.47	2294	6.3	84
SAGD2 postmortem (R6)	–41.00	1022	5.7	68

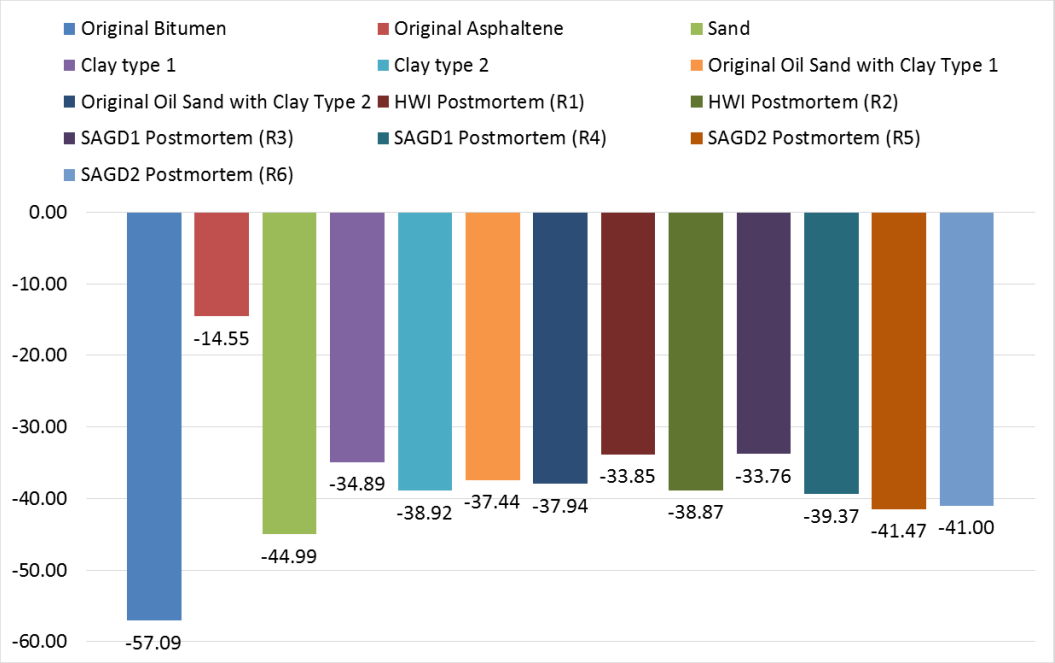

Fig. 17—Zeta potential measurement results of both reference materials and postmortem samples.

3.2.3 Interfacial Tension

The results of interfacial tension and surface tension measurements for original bitumen sample and produced oil samples originating from HWI, SAGD1, and SAGD2 were analyzed to find a possible correlation between the interfacial tension and cumulative oil production. **TABLE 14** shows the interfacial tension and surface tension measurements of each sample in detail along with cumulative oil production in percentages. Note that interfacial tension was measured at the interface of bitumen, and distilled water and surface tension were measured on the surface of bitumen when the oil sample was in contact with an air environment.

TABLE 14—SURFACE TENSION AND INTERFACIAL TENSION RESULTS FOR ORIGINAL AND PRODUCED OIL SAMPLES

Sample Name	Surface/Interfacial Tension	Interfacial and Surface Tension (mN/m)				Oil Recovery
		Run 1	Run 2	Run 3	Average	
Original bitumen	Surface tension	29.8	29.9	29.9	**29.87**	—
	Interfacial tension	18	16.8	18.4	**17.73**	
HWI	Surface tension	23.5	22.6	22.9	**23.00**	32.7%
	Interfacial tension	14.5	14.6	14.8	**14.63**	
SAGD1	Surface tension	29.3	30.2	29.5	**29.67**	47.4%
	Interfacial tension	13.7	14.1	14	**13.93**	
SAGD2	Surface tension	25	24.5	25.1	**24.87**	32%
	Interfacial tension	16.5	17.1	17	**16.87**	

The surface tension measurements of produced oil samples are lower than the surface tension of original Peace River bitumen. When the interfacial tension between oil

and distilled water was investigated, lower interfacial tension readings were observed for all produced oil samples in comparison to original Peace River bitumen. **Fig. 18** shows the comparison between measured surface tension and interfacial tension values.

Zhao et al. (2013) studied the oil-water interfacial tension effect on relative permeability curves, and one of their conclusions is that decreasing oil/water interfacial tension reduces the ROS and increases ultimate oil recovery. When the interfacial tension measurement results were investigated, they agree well with the proposed statement. Produced oil from SAGD1 has the highest recovery, and its interfacial tension is the lowest when compared with the HWI and SAGD2 experiments. Moreover, the lowest recovery is observed in SAGD2, and the interfacial tension value for this experiment is the highest in these three experiments.

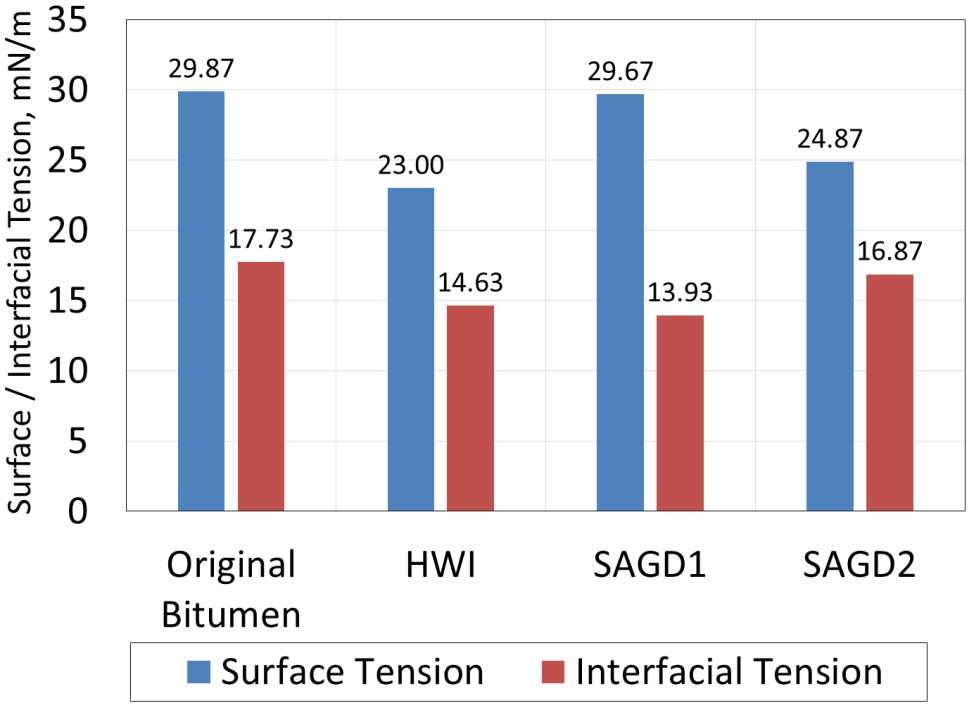

Fig. 18—Surface/interfacial tension results of original and produced oil samples.

3.2.4 Residual Oil and Water Saturations

All the experiments conducted with the SAGD experimental setup show lower ROS inside the injection zones when compared with outside the injection zones. Although steam reached the entire body of the system, oil drainage happened more efficiently in the region where the steam chamber growth was more exposed to steam as opposed to outside the steam chamber growth zone. The ROS measurements are in good agreement with the total oil recovery amounts. The SAGD1 experiment is the most successful experiment with respect to oil recovery percentages, and the ROSs are less than the other two experiments. The high ROS measurement for SAGD2 is due to the clay type, which contains both kaolinite and illite, and it yielded low recovery. **TABLE 15** shows the

observed ROSs of postmortem samples. The measurements were done for both around the injection well region, called inside injection zone, and very far away from the injection well, called outside injection zone.

The results of ROSs can be correlated with the contact angle measurements. The more oil-wet a section is observed to be using contact angle analysis, the more residual oil is encountered in the postmortem sample. R1 and R2 belong to the HWI experiment and represent inside and outside the injection zone, respectively (**Fig. 13**). As expected, sweep efficiency is more effective near the injection well, and oil is gathered mostly from this region. R3 and R4 belong to SAGD1 (**Fig. 14**), and similar results were obtained. Inside the injection zone (R3) shows less residual oil than R1 in the HWI experiment; this finding is a result of higher cumulative oil production obtained at the end of SAGD1. The residual oil values outside the injection zone are the same for both experiments, possibly due to the injected fluid being ineffective at that portion of the experimental setup, and because the rock properties of both experiments are the same, similar results are observed from outside the injection zone. R5 and R6 regions of SAGD2 (**Fig. 15**), prepared with a kaolinite and illite clay mixture, show significantly high ROS when compared with the other two experiments, which were prepared with clay type 1. This was expected as a result of the low oil recovery value obtained at the end of the SAGD2 experiment. There is still a residual oil contrast between inside injection zone and outside injection zone, but the difference is lower than HWI and SAGD1 experimental results.

TABLE 15—RESIDUAL OIL AND WATER SATURATION OF POSTMORTEM SAMPLES

Sample Name	Residual Saturation	
	Oil, fraction	Water (Range), fraction
HWI-R1	0.39	0.13 to 0.61
HWI-R2	0.47	0.02 to 0.53
SAGD1-R3	0.36	0.18 to 0.64
SAGD1-R4	0.47	0.07 to 0.53
SAGD2-R5	0.61	0.02 to 0.39
SAGD2-R6	0.64	0.02 to 0.36

Due to problems in preservation of postmortem samples, the residual water saturations are not reflected properly in the experimental results. The residual water saturations were measured very low, and most of the measurements are less than the initial water saturation, which is 16%. However, the postmortem samples were well preserved in terms of oil content due to low volatility of bitumen samples. Therefore, the residual water saturations were calculated by subtracting ROSs from one by assuming there was no residual gas saturation. Thus, the residual water saturation was given as a range between measured and calculated results **TABLE 15.** Because the system was filled with both water and steam just after the experiment, the condensed water could not occupy as much volume as steam did. **TABLE 15** also shows the residual water saturation ranges for each postmortem sample.

An interesting observation was made during the oil removal stage of postmortem samples. The postmortem samples were cleaned with a commercial chemical (Berryman

B-12 Chemtool), and when dried, samples were investigated and cementing behavior of illite containing clay (clay type 2) was observed. **Fig. 19 – A** and **– B** show the contrast between oil-free postmortem samples belonging to clay type 1 and clay type 2, respectively. Because B-12 Chemtool is a mixture of solvents, it was thought that a possible chemical reaction could cause this cementing behavior. Therefore, a new set of postmortem samples were cleaned from oil with toluene to verify the previously made observations. **Fig. 19 – C** and **– D** show the comparison between oil-free postmortem samples belonging to clay type 1 and clay type 2, respectively extracted by toluene. The same cementing behavior is observed for postmortem samples with clay type 2, which is an illite-containing clay type. This behavior might be explained by mica-type minerals (e.g., illite) that are thought to accelerate the chemical compaction between quartz grains. Thin grain-coating illite causes sandstone compaction and cementation while reducing its porosity and permeability (Worden and Morad, 2003). The possible cause of production decrease observed during the SAGD2 experiment could be the permeability reduction due to cementing or chemical alterations in clays.

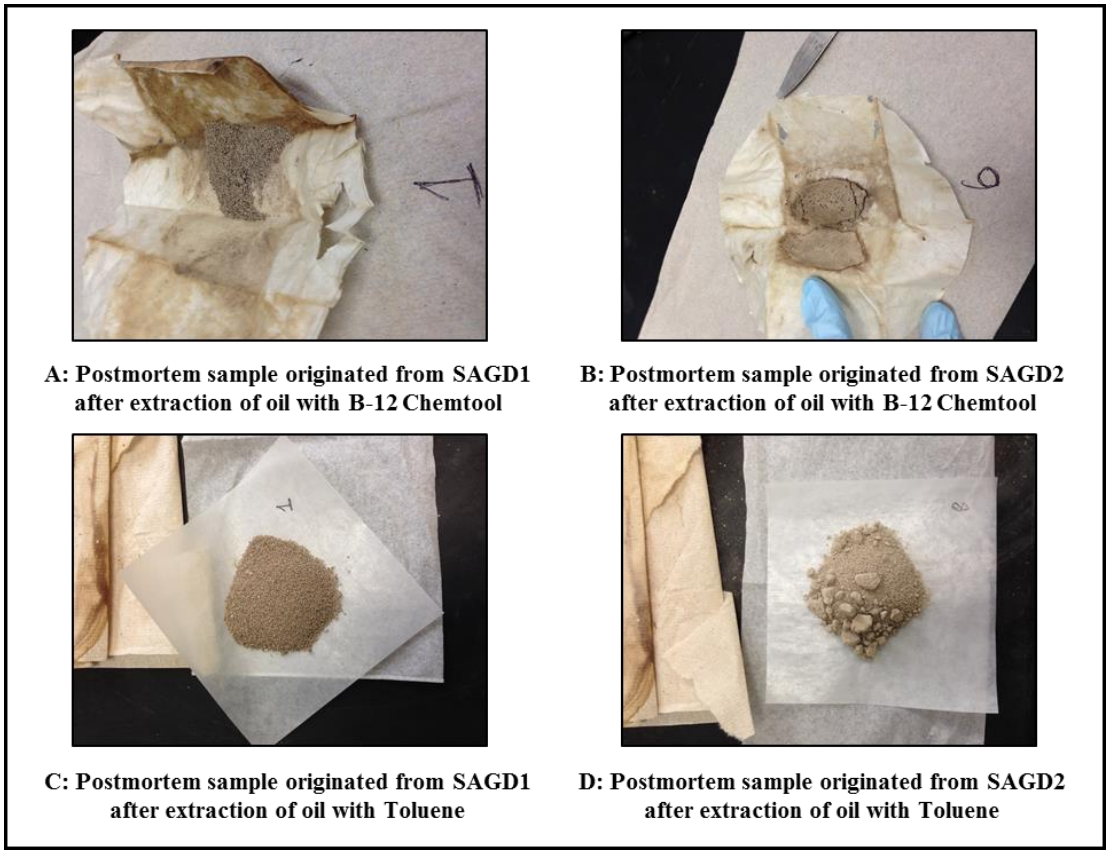

Fig. 19—Visualization of postmortem samples of SAGD1 and SAGD2 after oil extraction.

3.2.5 XRD Measurements

The SAGD1 and SAGD2 experiments provide very important findings that clay type difference can significantly impact the SAGD process performance. To better understand the mechanism behind the performance differences, two clay types were analyzed with XRD measurements previously in **Fig. 7** and **Fig. 8**. Note that, clay type 1 contains almost 100% kaolinite, and clay type 2 is a mixture of 10% illite and 90% kaolinite.

To understand the interaction of clay type 2 with steam, clay type 2 was subjected to continuous steam injection for six hours and then, analyzed with XRD. The XRD results of steamed clay type 2 are given in **Fig. 20.** No significant difference was observed between the steamed and non-steamed clay type 2. XRD results, proving that interaction of clay type 2 with steam does not cause any clay alteration.

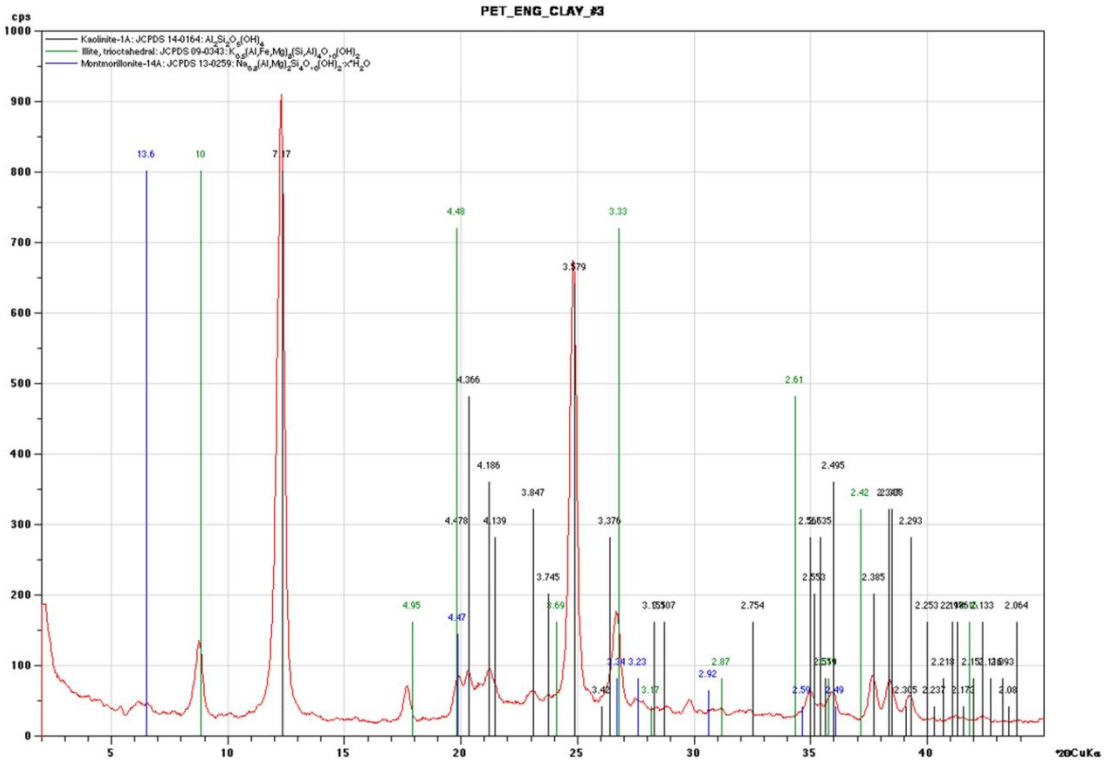

Fig. 20—XRD traces of clay type 2 after six-hour steam treatment.

Therefore, the possible clay alteration due to the interaction of clay-sand-bitumen under continuous steam injection condition was investigated with XRD analyses on the

postmortem samples of SAGD1 and SAGD2. Only inside steam chamber samples were analyzed at an off-campus facility. Before clay analyses, bitumen was removed by exposing postmortem samples to a solvent named Berryman B-12 Chemtool (**Appendix E**). The solid particles above 4 µm provide information on bulk mineral analysis; below 4 µm mainly provides the clay analyses results. Results are shown in **TABLE 16.** While clay type 2 does not show any alteration in clay composition, the XRD results on SAGD1 postmortem samples reveal the alteration of kaolinite and small portion of kaolinite is altered to smectite, mica, and illite. XRD spectrums of these two postmortem samples are given in **Appendix D.**

TABLE 16—BULK AND CLAY AND ONLY CLAY XRD ANALYSIS OF BOTH SAGD EXPERIMENTS IN wt% (R3 M-L I/S 15S: R=3 ORIENTED MIXED-LAYER ILLITE/SMECTITE WITH 15% SMECTITE LAYERS)

Analytical Method	Sample ID	R3 M-L I/S 15S	Illite and Mica	Kaolinite	Quartz	Total
Bulk and clay	SAGD 1	0.6	1.7	4.4	93.3	100
	SAGD 2	0	2.7	4.1	93.2	100
Clay	SAGD 1	1.7	1.1	94.6	2.7	100
	SAGD 2	0	11.2	79.1	9.7	100

3.2.6 SEM Images

The SEM images of reference materials used in each experiment during the preparation of experiments are shown in **Fig. 21. Fig. 21 - A** shows the sand grains with 25× magnification, and **Fig. 21 - D** is the same sand grains with 2,000× magnification.

Fig. 21 - B and **- E** show clay type 1 with 1,000× and 3,000× magnifications, respectively. The images of clay type 2 are shown in **Fig. 21 - C** and **- F** with 1,000× and 3,000× magnifications, respectively. These pictures show the initial view of materials before mixing for oil sand preparation.

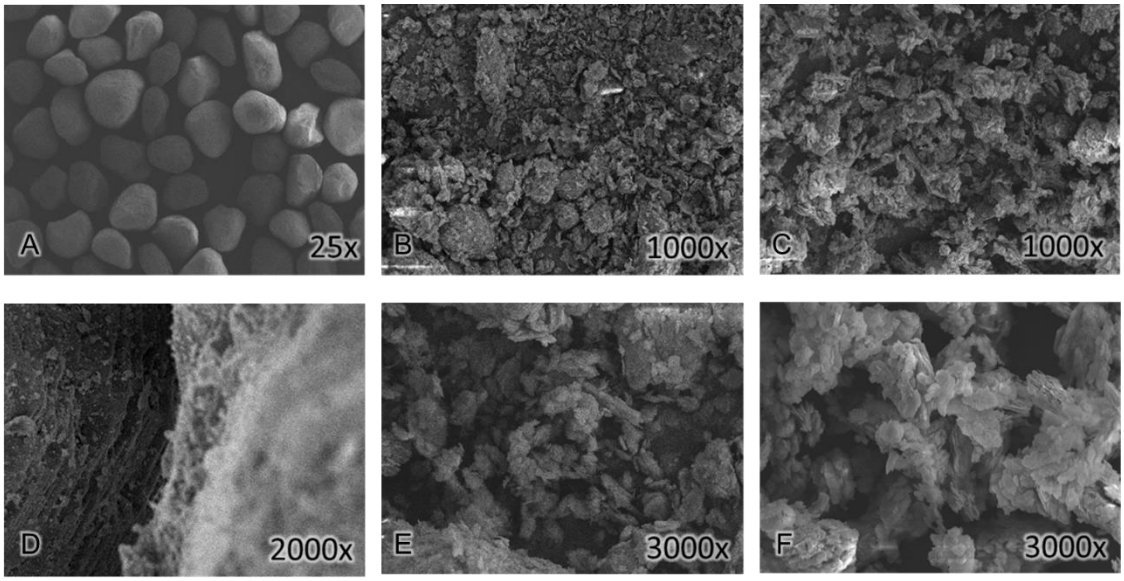

Fig. 21—SEM images of sand (at 25× magnification A, at 2,000× magnification D), clay type 1 (at 25× magnification B, at 3,000× magnification E), and clay type 2 (at 25× magnification C, at 3,000× magnification F).

The first analysis was done to investigate the direct interaction of steam with clay type 2. Clay type 2 was exposed to steam for 6 hours SEM images were taken before and after steam exposure of clay type 2 are provided in **Fig. 22.** While **Fig. 22 – C** and **– F** represent the original clay SEM images in 1,000× and 3,000× magnification, respectively, **Fig. 22 – G** and **– H** give the SEM images of steamed sample at same magnification. When steamed sample was compared with original clay type 2 result, steamed sample is

in more consolidated structure. Therefore it is obvious that interaction of clay with steam result in permeability reduction.

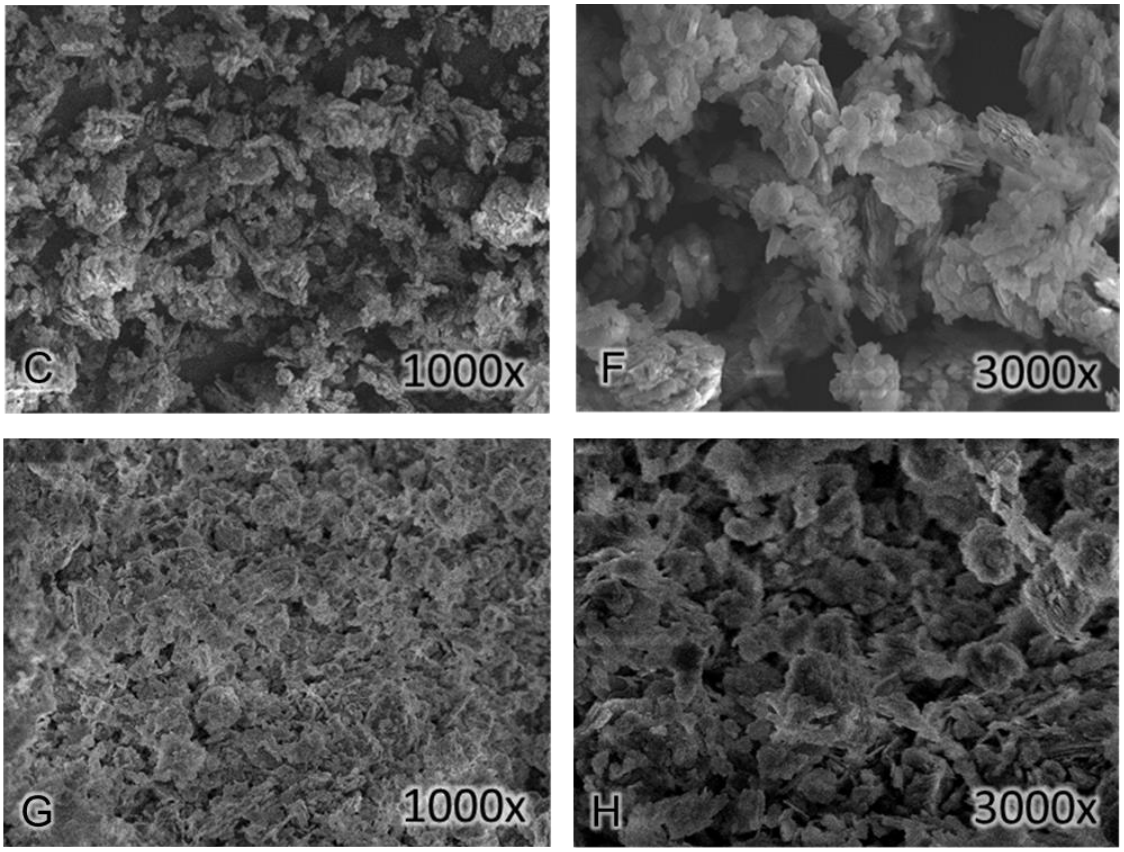

Fig. 22—SEM images of original clay type 2 (C, F) and clay type 2 after steam treatment (G, H).

The SEM images of spent rock samples were investigated for possible pore throat plugging due to clay cementation **Fig. 23.** Note that the samples for the HWI and SAGD1 experiments were prepared with clay type 1, the only difference was the injection temperature used in each experiment. SAGD1 and SAGD2 were conducted at identical injection temperature. However, during sample preparation clay type 1 and clay type 2

were used respectively. Before SEM images were taken, residual oil was removed from postmortem and samples visualized with SEM after oil extraction is completely achieved. Extraction is done with toluene. **Fig. 23 – I** and **– J** show the extracted postmortem after HWI, **Fig. 23 – K** and **– L** show the extracted postmortem after SAGD1, and **Fig. 23 – M** and **– N** show the extracted postmortem after SAGD2 in 25× and 1,000× magnification, respectively. It is obvious that while the experiments conducted with clay type 1 (HWI and SAGD1) did not result in plug-in pore throats, experiment prepared with clay type 2 (SAGD2) result in cementing. Consequently, reduction in permeability caused oil production reduction. On the other hand, the temperature difference in HWI and SAGD1 experiments did not cause any significant change on surface structures of both post mortems.

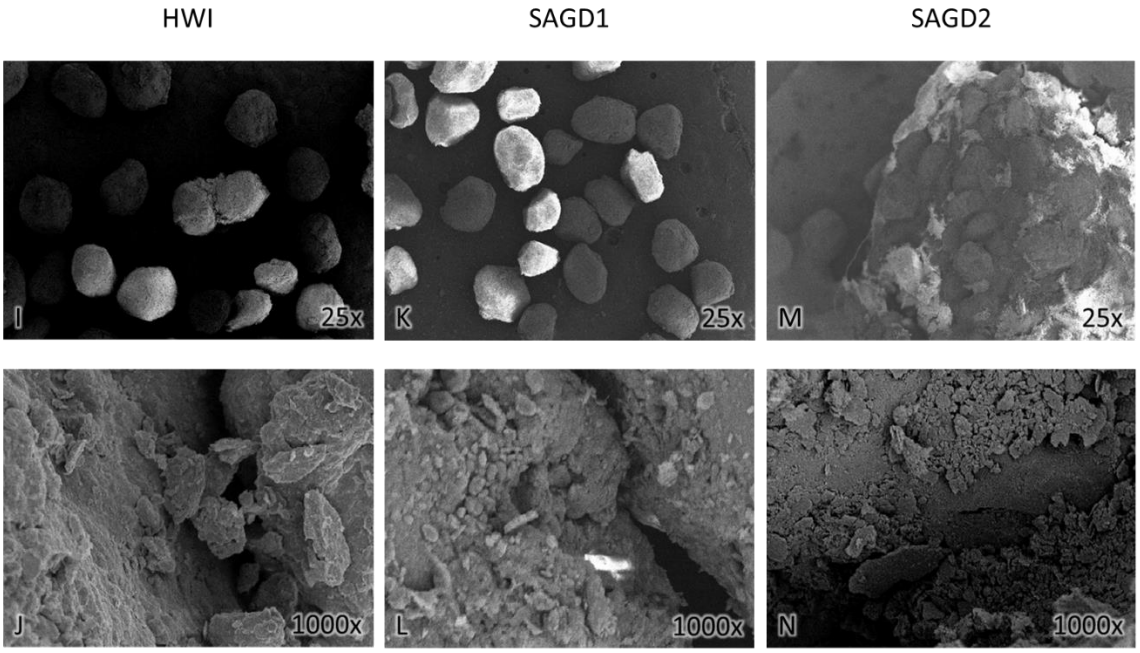

Fig. 23—SEM images of postmortem samples of HWI (I, J), SAGD1 (K, L), and SAGD2 (M, N).

3.3 Conclusions

Wettability change mechanisms for three experiments were investigated with several experimental analyses on produced oil, produced water, and spent rock samples. The samples originating from HWI and SAGD1 experiments were investigated to characterize the impact of injected fluid temperature on wettability characteristics. Analyses of SAGD1 and SAGD2 experiments were compared to better understand the influence of clay composition on production trends of SAGD with wettability, clay alteration, clay migration, and permeability reduction due to cementation behavior of clays.

The analyses consist of contact angle measurements, zeta potential measurements, interfacial and surface tension measurements of oil samples, residual fluid saturations of postmortem samples, SEM images, and XRD measurements of clay and postmortem samples. Contact angle measurements were done to understand the wettability characteristics around the injection wellbore and away from injection zone. Zeta potential, interfacial/surface tension, and XRD measurements were conducted to check the impact of chemical and surface electrical forces on wettability, as well as SAGD process performance. Residual fluid saturations were determined to reveal the relationship between wettability and residual fluid saturations. The results of these analyses are also used for tuning relative permeability curves and determining their temperature-dependent endpoint changes in numerical analyses.

The following conclusions can be drawn from this study:

- Increasing temperature triggers wettability to a more water-wet state, and illite containing clay (clay type 2) in oil sands yields more oil-wet rock samples after steam treatment.
- Particle size measurements of clay types explains the possible reason for oil recovery reduction for SAGD2. The measured particle size of clay type 2 is almost double compared to clay type 1. Thus, clay type 2 is a possible candidate for pore throat plugging and causing oil production reduction by decreasing the permeability of oil sand. Particle size measurements on produced water samples and SEM images support this statement.

- The produced water TDS measurement of SAGD1 is higher than the produced water of SAGD2. This might be a sign that clay type 1 is more prone to migrate in water. Suspended clay particles were transported with produced water, and permeability increase might be the reason for high oil production encountered during SAGD1. The particle size measurement results also support this finding. Due to large particle sizes in produced water originating from SAGD1, which is the same size as clay type 1 (~1,200 nm), kaolinite and transformed clays should be produced along with water.
- Asphaltenes obtained from the produced oil of SAGD2 shows a lower zeta potential value than asphaltene originating from the produced oil of HWI and SAGD1 experiments. This means that asphaltene of SAGD2 is more oil-wet. Note that both HWI and SAGD1 experiments were conducted with clay type 1, the composition of which is mostly kaolinite. This result indicates that the wettability of asphaltene could be the cause of high oil-wetness observed at the end of SAGD2 and relatively less oil-wetness observed for HWI and SAGD1 might be due to wettability of asphaltene.
- Interfacial tension measurements support the literature statement that higher ultimate recoveries can be observed for oils with lower interfacial tension values.
- Clay type 2–containing oil sand samples were more cemented and compacted, yielding lower oil recoveries due to lower permeability. Cementing behavior of clay type 2 is observed on the SEM images also.

CHAPTER IV

NUMERICAL STUDIES

4.1 Numerical Procedures

Reservoir performance can be predicted by using experimental methods, analytical methods, and numerical methods. Because numerical simulations are simple and yield quick results, they are always preferred to predict reservoir performance (Wang, 2010).

Numerical methods are applied by using finite difference simulators, which divide reservoir sections into small grid blocks and use material balance, fluid phase behavior, and Darcy flow equations in porous media for each grid block. Thermal reservoir simulators also include conversion of energy in addition to previously mentioned parameters (Mattax and Dalton, 1990).

Accuracy of reservoir simulation results have to be validated with field data or experimental results. This phase is called history-matching, and it is the most time consuming and crucial section of a numerical study. Numerical simulation studies are unreliable without history-matching by real data.

Commercial reservoir simulation software programs are widely used by reservoir engineers, and they prove their effectiveness in simulation of both laboratory-scale and complicated field-scale problems. Three experimental results were simulated numerically with CMG STARS (2013), HWI, SAGD1, and SAGD2, with the aim of finding relative permeability changes with temperature and clay type. The details of input parameters

(model dimensions, reservoir properties, fluid model, relative permeability data, well constraints, and initial conditions of the model) are detailed in the following sections.

4.1.1 Model Dimensions

The experimental model used for the experiments consists of two concentric cylinders, and prepared oil sand samples were placed inside the annulus of these two concentric cylinders. The outer radius of the experimental setup is 16.51 cm, and the inner radius is 6.35 cm. The stainless steel wall thickness is 1.905 cm, and it covers all the reservoir section. The producer well was located 2.54 cm higher from the bottom of the setup, and the well spacing between injector and producer wells was 5.08 cm.

The physical model, which is shown in **Fig. 5,** was converted to a numerical model with a grid system of 4 × 60 × 29, as shown in **Fig. 24.** In literature, 1- × 1-cm grid blocks are used for Cartesian laboratory-scale SAGD simulations. A radial model with an average grid size of 1.27 × 1 cm was used to model the reservoir section of the experimental setup. A cross-sectional view of the numerical model is shown in **Fig. 25.** In this figure, grid blocks A represent the stainless steel body of the physical setup with 1.905 cm thickness, which is the wall thickness of stainless steel. Grid blocks B are the reservoir section with 6.35 cm thickness. The innermost cylindrical grid blocks were chosen very small in volume due to gridding problems, and they were assigned as null blocks.

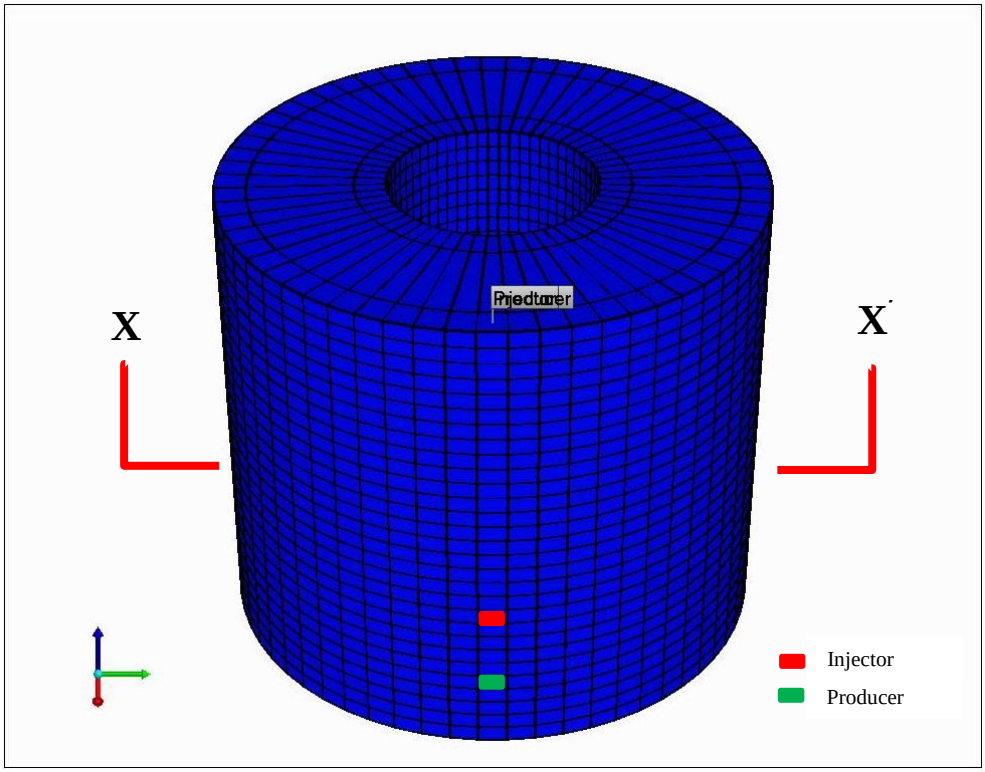

Fig. 24—General view of SAGD model; red and green represent the location of injection and production wells, respectively.

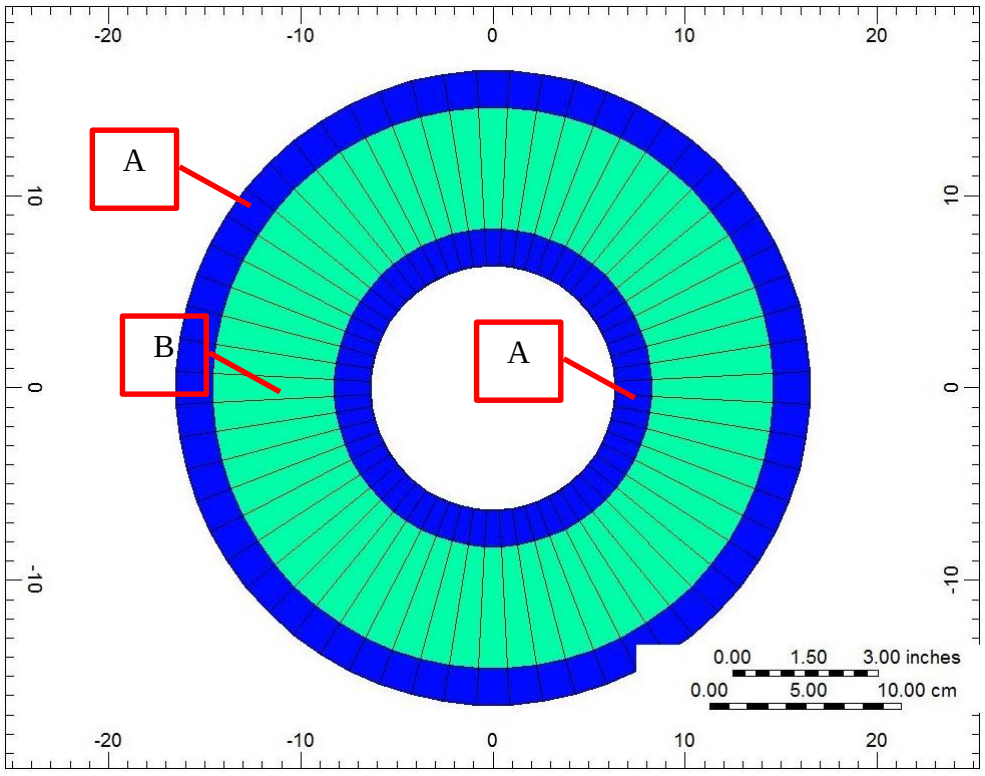

Fig. 25—Cross-sectional view of numerical model. The dark blue sections (A) represent stainless steel sections of the SAGD setup. The green section (B) represents the oil sand pack region (X — X' cross section is given in Fig. 24).

The locations of injection and production wells are given in **TABLE 17.** The block numbers in the k-direction increase from top to bottom.

TABLE 17—WELL LOCATIONS OF THE NUMERICAL MODEL

	Block		
Well Name	**i**	**j**	**k**
Producer	3	1	25
Injector	3	1	20

4.1.2 Reservoir Properties

Homogenous reservoir conditions were assumed for this numerical model. The reservoir properties are mentioned in **TABLE 18.**

TABLE 18—RESERVOIR PROPERTIES USED IN THE NUMBERICAL MODEL

Parameter (Unit)	**Value**	**Obtained**
Porosity (fraction)	0.32	Experimentally
Horizontal permeability (Darcy)	80	(Wang, 2010)
Vertical permeability (Darcy)	80	(Wang, 2010)
Capillary pressure (kPa)	0	Assumed
Rock compressibility (1/kPa)	$9.6e^{-6}$	(Shin, 2006)
Rock heat capacity [J/(cm^3-°C)]	2.35	(Wang, 2010)
Rock thermal conductivity (J/cm-min-°C)	2.5833	(Wang, 2010)
Water thermal conductivity (J/cm-min-°C)	0.3715	(Wang, 2010)
Oil thermal conductivity (J/cm-min-°C)	0.07986	(Wang, 2010)
Gas thermal conductivity (J/cm-min-°C)	0.000972	(Wang, 2010)
Initial temperature (°C)	25	Experimentally
Initial pressure (kPa)	101	Experimentally
Initial oil saturation (fraction)	0.84	Experimentally
Initial water saturation (fraction)	0.16	Experimentally
Initial gas saturation (fraction)	0	Experimentally

Different input parameters are used to define stainless-steel sections of the model. Those properties are given in **TABLE 19.** Because stainless steel is an impermeable and nonporous material, permeability and porosity were chosen as zero in the numerical simulation. The assigned heat capacity and heat conductivity values are for Grade 304 stainless steel (Mukhametshina, 2013). The experimental setup was wrapped with insulator materials to minimize heat losses. Directional heat loss parameters were introduced for stainless steel grid blocks by considering the minimized heat losses. While

k-direction heat loss represents the heat losses from the top and bottom of the experimental setup, i-direction heat loss represents the heat losses from the lateral surfaces of cylinders. Volumetric heat capacities for heat loss calculations were relatively high values to better represent the heat losses due to convectional heat transfer. Gas thermal conductivity was included in the simulation by considering the heat losses due to ambient air surrounding the experimental setup.

TABLE 19—GRID BLOCK REPRESENTING STAINLESS STEEL SECTIONS OF THE EXPERIMENTAL SETUP

Parameter (Unit)	**Value**	**Obtained**
Porosity (fraction)	0	-
Horizontal permeability (Darcy)	0	-
Vertical permeability (Darcy)	0	-
Rock compressibility (1/kPa)	0	-
Rock heat capacity [J/(cm^3-°C)]	3.92	(Steel, 2007)
Rock thermal conductivity (J/cm-min-°C)	10.20	(Steel, 2007)
Initial oil saturation (fraction)	0	-
Initial water saturation (fraction)	0	-
I-direction volumetric heat capacity [J/(cm^3-°C)]	7	Assumed
I-direction thermal conductivity (J/cm-min-°C)	0.000972	(Wang, 2010)
K-direction volumetric heat capacity [J/(cm^3-°C)]	7	Assumed
K-direction thermal conductivity (J/cm-min-°C)	0.000972	(Wang, 2010)

The uppermost grid-block layer of the reservoir section was assigned as a gas-bearing zone to better represent the production delay observed during experiments. This phenomenon might be true for the real case experiments. Because the experimental sand pack was unconsolidated sand and perfect packing of the samples cannot be accomplished. This settlement can be observed for SAGD1 and SAGD2 experiments in **Fig. 26** and **Fig.**

27, respectively. The properties assigned for this layer slightly differ from the original reservoir section (**TABLE 20**).

Fig. 26—Top view of SAGD experimental setup after SAGD1 experiment to visualize sand settlement which result in gas bearing zone at the top of the setup.

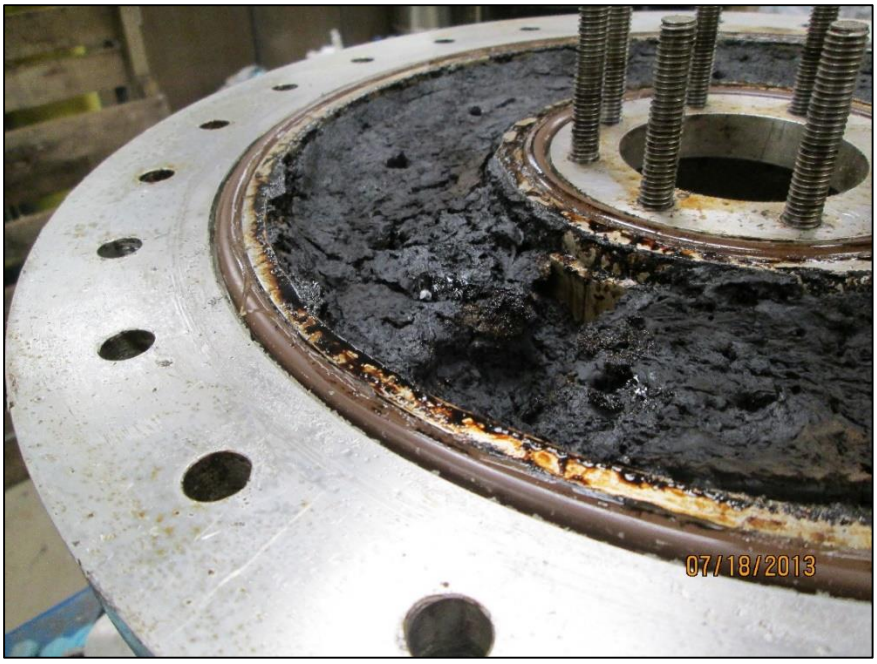

Fig. 27—Top view of SAGD experimental setup after SAGD2 experiment to visualize sand settlement which result in gas bearing zone at the top of the setup.

TABLE 20—MODIFIED PARAMETERS REPRESENTING THE NITROGEN-SATURATED SECTION OF EXPERIMENT FOR THE TOP OF THE RESERVOIR

Parameter (Unit)	Value
Porosity (fraction)	1
Horizontal permeability (Darcy)	10,000
Vertical permeability (Darcy)	10,000
Initial oil saturation (fraction)	0
Initial water saturation (fraction)	0
Initial gas saturation (fraction)	1

4.1.3 Fluid Model

The model has three components: bitumen, water, and nitrogen (N_2). CMG library values were used for the water and N_2 properties. While some of the bitumen properties

were based on laboratory measurements, the other properties were obtained from reference studies (Shin, 2006; Svrcek and Mehrotra, 1989). The list of the bitumen properties is shown in **TABLE 21.**

TABLE 21—BITUMEN PROPERTIES USED IN NUMERICAL MODEL

Parameter (unit)	Value	Obtained
Bitumen molecular weight (kg/gmole)	0.5275	(Svrcek and Mehrotra, 1989)
Critical pressure (kPa)	1360	(Shin, 2006)
Critical temperature (°C)	624.65	(Shin, 2006)
Mass density of bitumen (kg/cm^3)	0.0010085	Experimentally
Bitumen compressibility (1/kPa)	5.5e^{-7}	(Shin, 2006)
First thermal expansion coefficient (1/°C)	8e^{-4}	(Shin, 2006)

Viscosity measurements of Peace River bitumen were obtained experimentally by using Brookfield DV-III Ultra programmable rheometer. Measurements were achieved between 23 and 100 °C. A trend line was fitted for these measurements, and a temperature-viscosity relationship was found between 21 and 315 °C and these values were used in numerical simulation studies. **Fig. 28** shows the viscosity measurements, fitted trend line, and the trend line equation. **Appendix C** shows the calculated viscosity and temperature values by using the trend line equation.

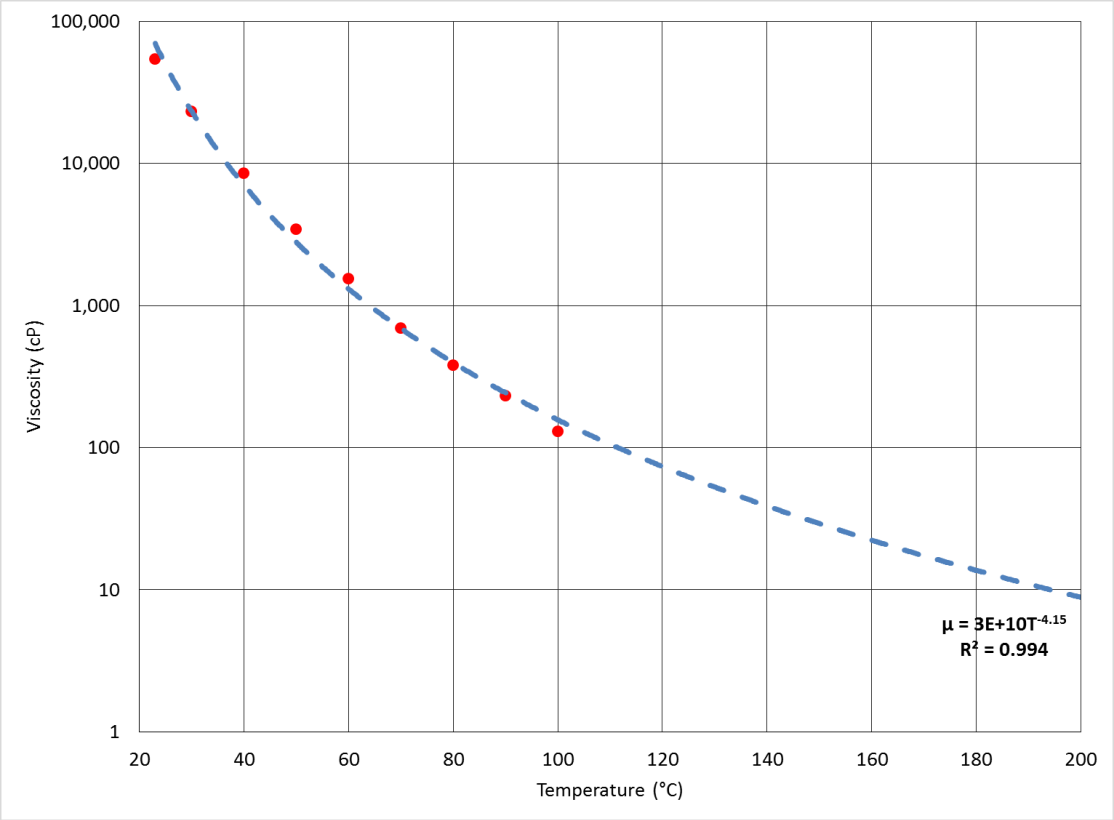

Fig. 28—Viscosity-temperature relation for original bitumen sample. Red dots were obtained experimentally and blue dashed line values were used in numerical simulation.

4.1.4 Relative Permeability Data

Oil-water and liquid-gas relative permeabilities are two of the most important parameters drastically affecting the flow behavior of reservoir fluids. However, it is very difficult to determine relative permeability curves experimentally, especially for heavy-oil and bitumen reservoirs. The relative permeability curves for the oil-water system and gas-liquid system were modified from the study of Wang (2010) considering the results of the experimental analyses. The relative permeability curves obtained from literature are

shown in **Fig. 29** and **Fig. 30** show oil-water and gas-liquid relative permeability curves used in this study for base case simulation. The relative permeability curves represent oil-wet behavior according to the **TABLE 3.** Initially, relative permeability graphs selected as oil-wet due to the experimentally obtained contact angle measurements of original oil sand samples given in **Fig. 12** which indicate oil-wet behavior prior to experiments.

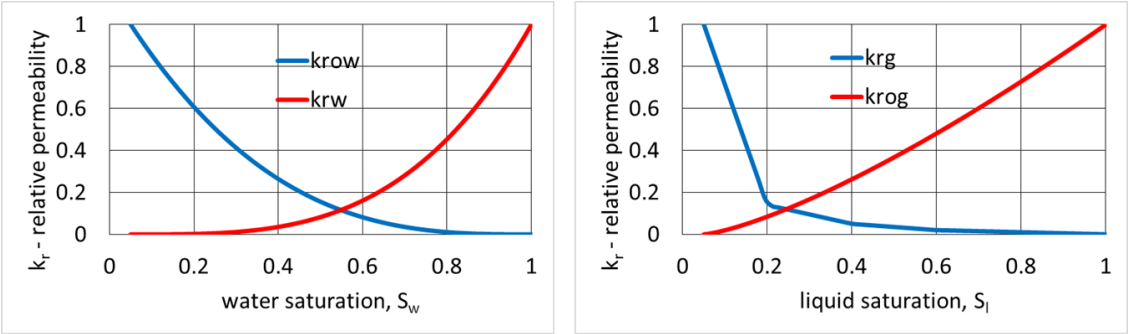

A – Water-oil relative permeability curve

B – Liquid-gas relative permeability curve

Fig. 29—Water-oil (A) and liquid-gas (B) relative permeability curves from literature (Wang, 2010).

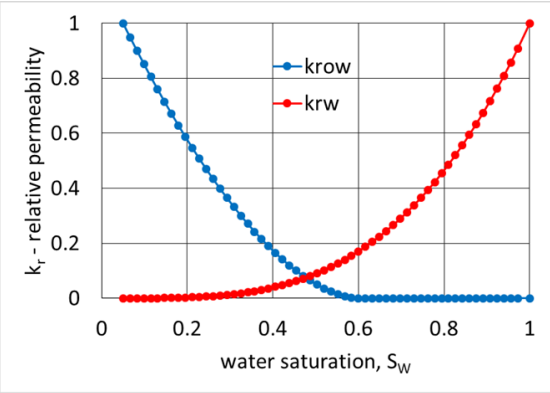

C – Modified water-oil relative permeability curve

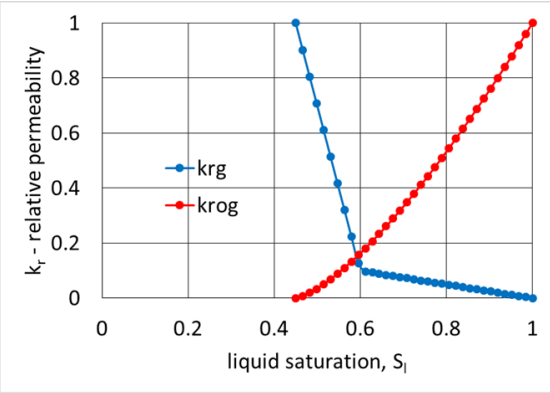

D – Modified liquid-gas relative permeability curve

Fig. 30—Modified water-oil (C) and liquid-gas (D) relative permeability curves.

As mentioned in the literature review, relative permeability endpoints change with a change in temperature (**TABLE 4**). Because the results of these studies agree on the effect of temperature on endpoint saturations, IWS (S_{wr}), ROS for water injection (S_{orw}), and ROS for gas injection (S_{org}) values were determined as temperature-dependent values in the numerical simulation.

Increasing temperature raises water-wetness, which is supported by previous studies (Civan, 2004; Nakornthap and Evans, 1986). Therefore, ROS decreases and IWS increases by increasing water-wetness as a result of increasing temperature. **TABLE 22** shows the temperature-dependent endpoint saturation values used in the numerical model.

TABLE 22—ASSUMED TEMPERATURE-DEPENDENT ENDPOINT SATURATIONS FOR HWI, SAGD1, AND SAGD2 EXPERIMENTS

Experiment Name	Temperature (°C)	S_{wr} (fraction)	S_{orw} (fraction)	S_{org} (fraction)
SAGD1, HWI	25	0.05	0.4	0.4
	180	0.2	0.3	0.35
SAGD2	25	0.05	0.4	0.7
	180	0.2	0.05	0.6

Fig. 31 and **Fig. 32** graphically show the temperature-dependent changes in relative permeability curves for HWI and SAGD1 numerical models. Blue lines show relative permeability curves at 25 °C, and red lines represent relative permeability curves at 180 °C. Solid lines in **Fig. 31** represent oil relative permeabilities, and dashed lines represent water relative permeabilities. The solid lines of **Fig. 32** show gas relative permeabilities, and dashed lines show liquid relative permeabilities.

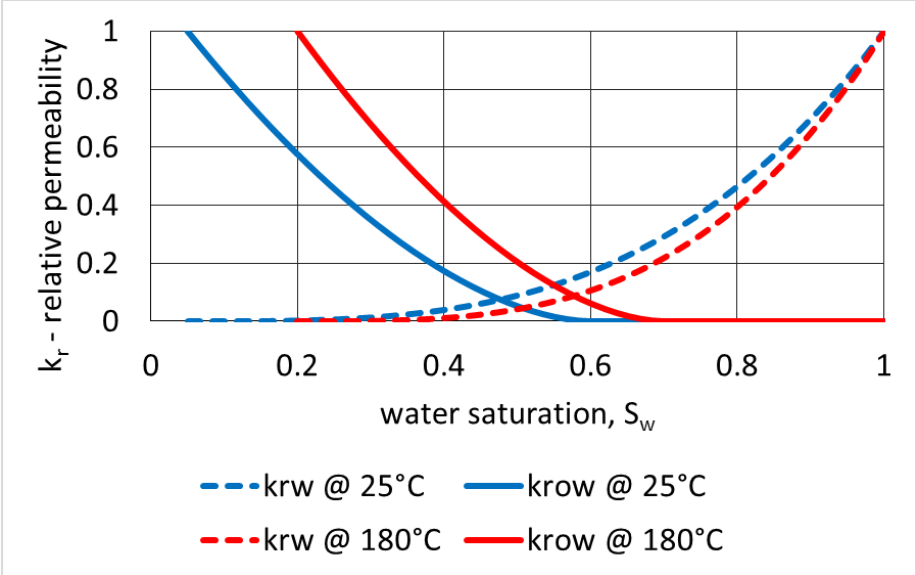

Fig. 31—Temperature dependence of water-oil relative permeability curve for HWI and SAGD1 used in numerical model.

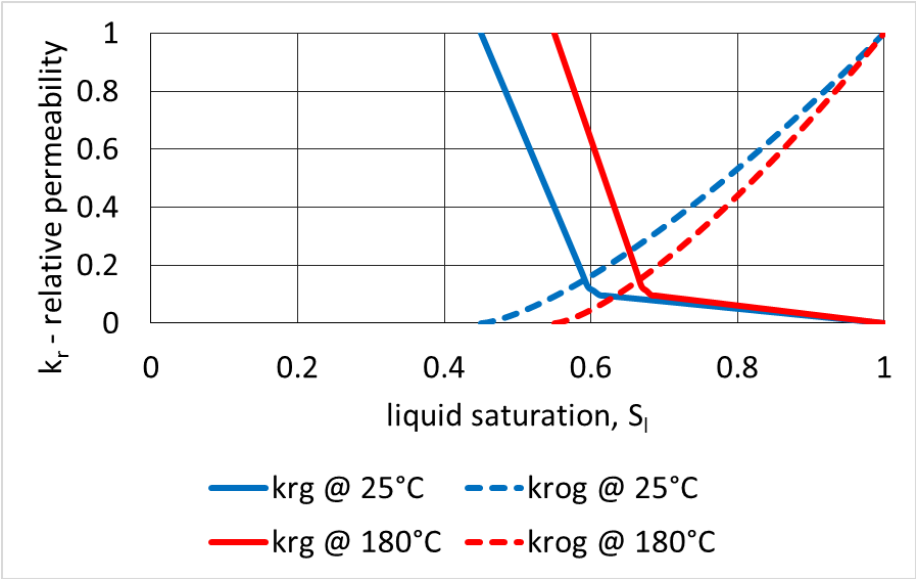

Fig. 32—Temperature dependence of gas-liquid relative permeability curve for HWI and SAGD1 used in numerical model.

When the water-oil relative permeability curve used to simulate SAGD1 experiment is compared with Craig's rules of thumb, the 180 °C case satisfies the rules for the water-wet case (Anderson, 1987). In addition, the 25 °C case satisfies Craig's rules of thumb for the oil-wet case. Thus, it can be said that temperature-dependent wettability change successfully transferred to the numerical model.

The water-oil and gas-liquid relative permeability curves used in the simulation of SAGD2 are given in **Fig. 33** and **Fig. 34,** respectively. Blue curves show relative permeability curves at 25 °C, and red curves represent relative permeability curves at 180 °C. Solid lines in **Fig. 33** represent oil relative permeabilities, and dashed lines represent water relative permeabilities. The solid lines of **Fig. 34** show gas relative permeabilities, and dashed lines indicate liquid relative permeabilities. Relative permeability curves of

the SAGD2 numerical model were modified according to the ROS measurements obtained experimentally and given in **TABLE 15.**

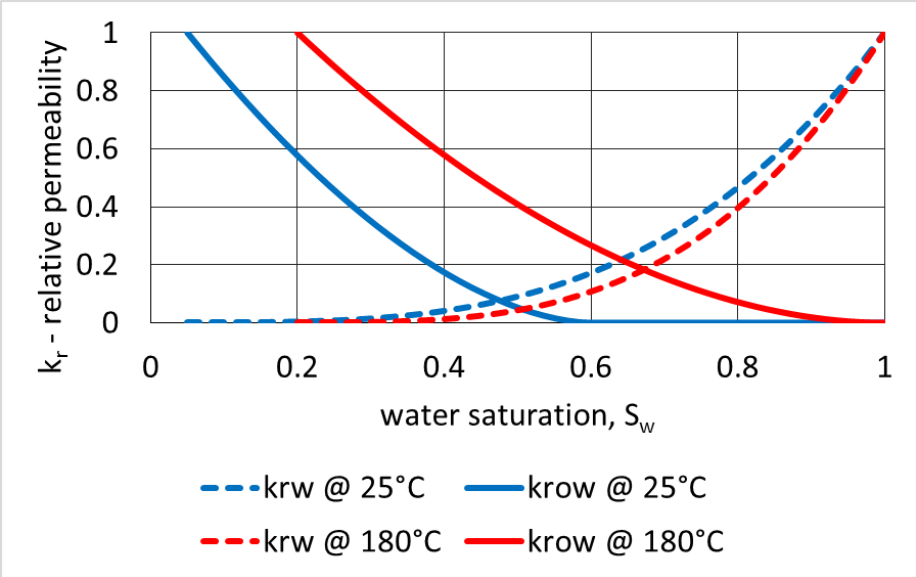

Fig. 33—Temperature dependence of water-oil relative permeability curve for the simulation of SAGD2 experiment.

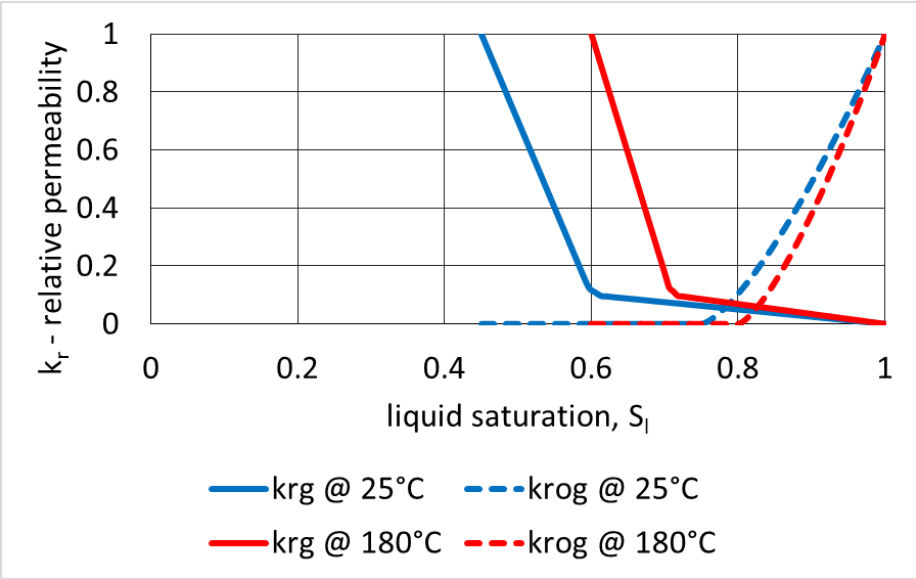

Fig. 34—Temperature dependence of gas-liquid relative permeability curve for the simulation of SAGD2 experiment.

4.1.5 Well Constraints

The steam injection rate was constant at 18 cc/min of cold water–equivalent for all three experiments. In addition, the production well was back-pressured with N_2 at 618.5 kPa throughout all three experiments. Injected fluid properties are shown in **TABLE 23.** Hot water injection was maintained numerically by varying the steam quality of injected fluid. For numerical simulations of SAGD1 and SAGD2 experiments nearly pure steam is injected with almost 100% steam quality.

TABLE 23—INJECTED FLUID PROPERTIES USED IN NUMERICAL SIMULATION FOR THREE EXPERIMENTS

Parameters Used in Numerical Simulation	**Experiment Name**		
	HWI	**SAGD1**	**SAGD2**
Steam temperature (°C)	165	165	165
Steam quality (fraction)	0.6	0.99	0.99

4.2 Numerical Results

Experimentally obtained, cumulative oil production results from HWI, SAGD1, and SAGD2 are shown in **Fig. 35.** Oil production was started about 15 minutes later than steam injection started for HWI and SAGD1. However, it can be inferred that SAGD2 started to produce oil 90 minutes later than the steam injection started, which can be explained by a possible problem faced at the startup procedure of the experiment. Because of this reason, the cumulative oil and water production values of SAGD2 were adjusted according to this fact. The modified cumulative oil production curves are given in **Fig. 36.**

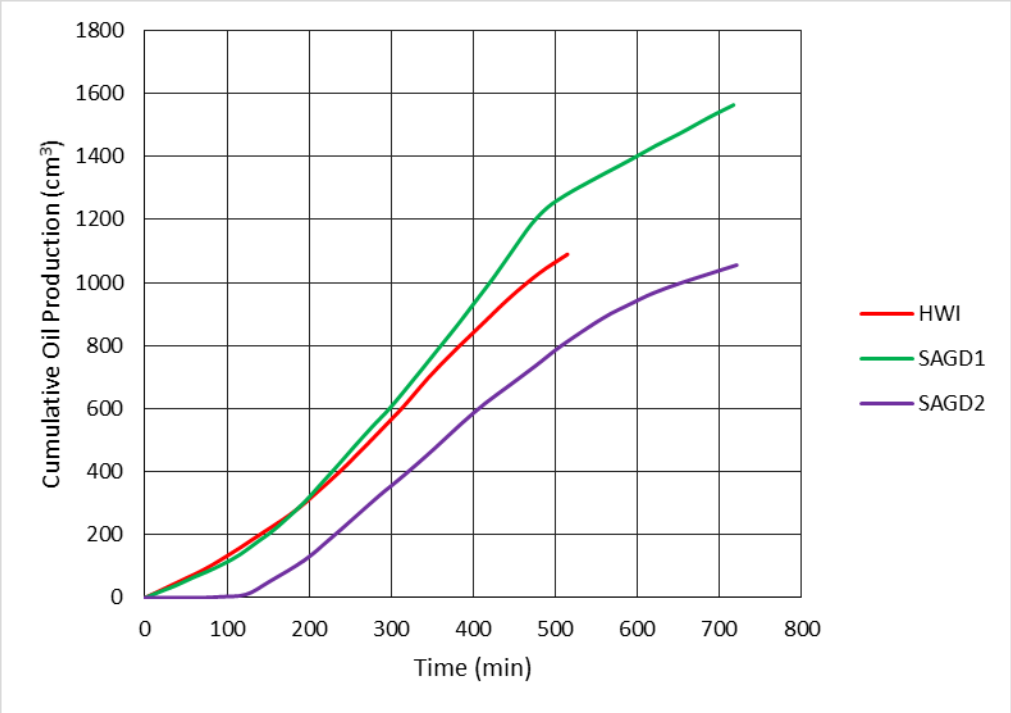

Fig. 35—Experimentally obtained cumulative oil production for HWI, SAGD1, and SAGD2 experiments.

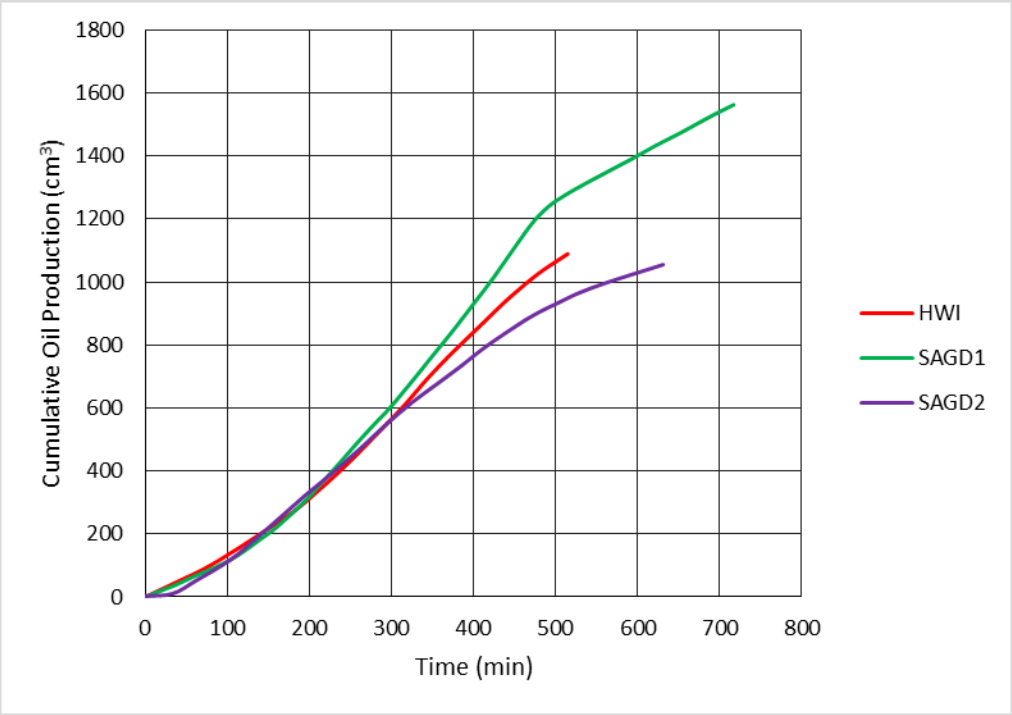

Fig. 36—Modified cumulative oil production data for HWI, SAGD1, and SAGD2 experiments.

Cumulative oil production and cumulative water production curves obtained at the end of simulations were checked with the data from experiments. It was observed that perfect history-matches were obtained on the modified water and oil production rates for all three experiments by changing injected fluid property and wettability behaviors to represent the impact of clay type. Temperature profiles of experiments and numerical simulation results were also compared, and the results are in a good agreement.

Note that because SAGD1 is the experiment packed with Ottawa Sand and clay type 1 mixture, it was selected as the base case for the numerical simulation studies. Moreover, SAGD1 is selected as base case, since this experiment only vary with one

parameter with the other two experiment. Therefore, this experiment is the best candidate for the starting point of history-matching because it has frequent data for oil production, and the injection temperature was kept constant during the experiment. As can be observed from **Fig. 37,** a perfect match was obtained with the numerical model for the SAGD1 cumulative oil production curve.

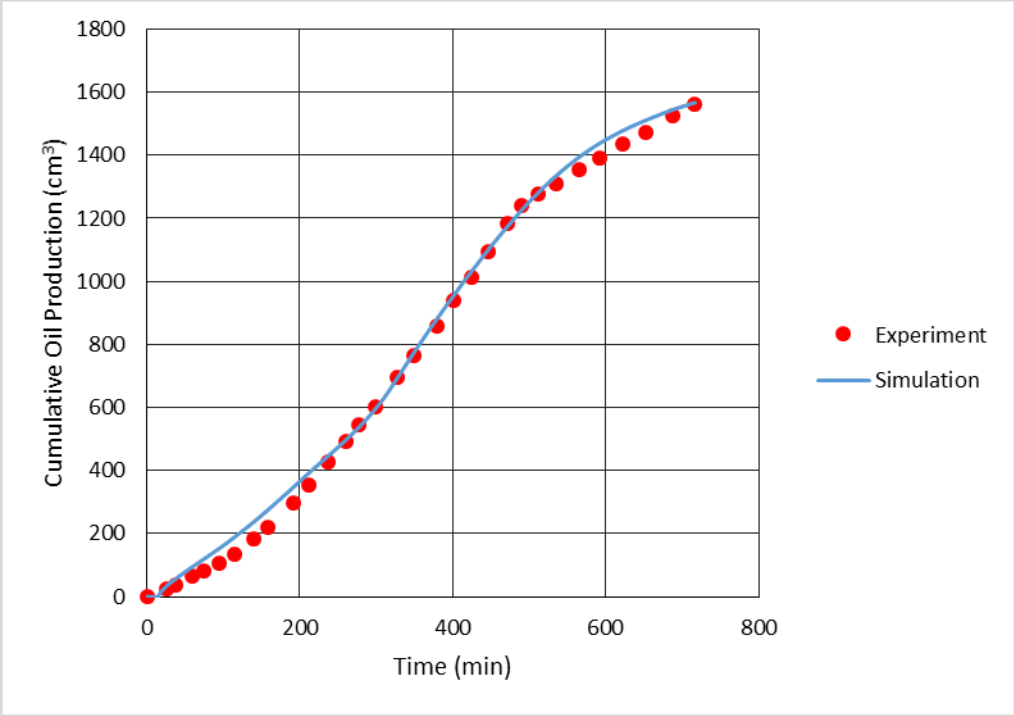

Fig. 37—Cumulative oil production vs. time results of SAGD1 experiment and simulation.

The history-matching result for cumulative water production is shown in **Fig. 38.** Slightly higher cumulative water production was observed in simulation results when the history-matched results were investigated. Due to the fact that separators used in the

experimental setup were not capable of condensing all the produced steam, some of the produced water was lost in gas phase and it could not be captured in the later stages. Note that the oil saturation of near-injection-wellbore grid cells at the end of the simulation (34%) is almost the same as the postmortem ROS result gathered from the injection zone (36%) (**TABLE 15**). This is increasing the reliability of relative permeability graphs and saturation end point changes with temperature, used to simulate SAGD1 experiment.

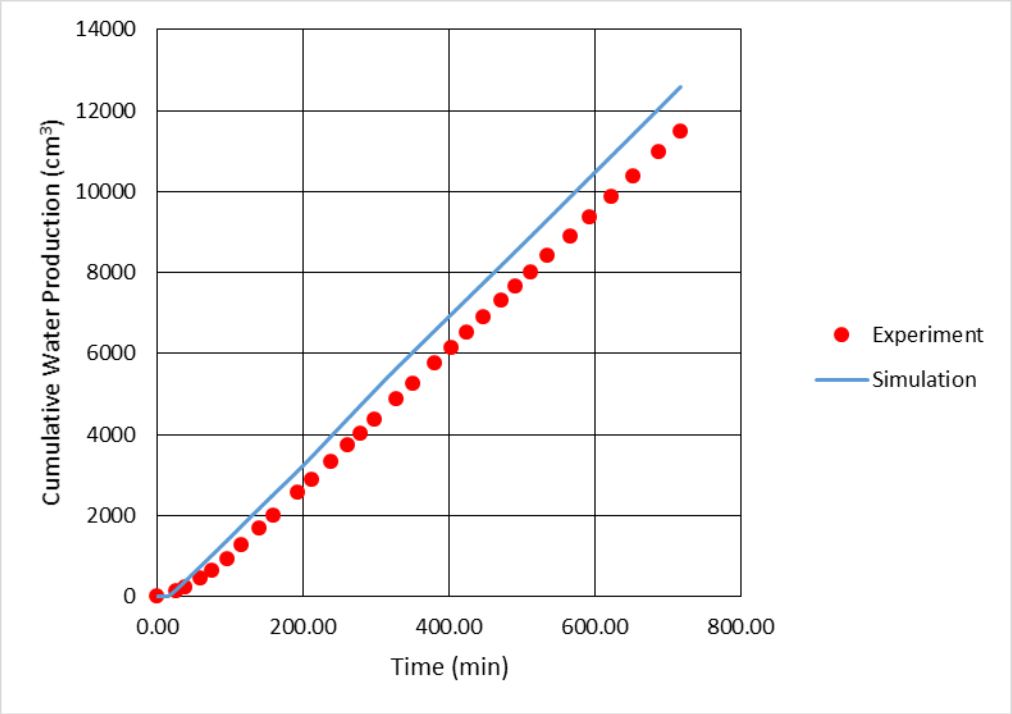

Fig. 38—Cumulative water production vs. time results of SAGD1 experiment and simulation.

Numerical simulation results further compared with experimental results for temperature propagations. Hourly temperature profile changes of the SAGD1 experiment

and its numerical simulation are given in **Fig. 39.** A reasonable match is observed between simulation and experimental results in spite of the fact that there are some deviations between them. Because countercurrent flow inside the steam chamber cannot be simulated in the numerical simulation (Chow and Butler, 1996), the steam chamber reached the top of the model faster than the experimentally observed time. In contrast, lateral expansion of the steam chamber is slower in the numerical simulation than the experimental temperature propagation because the numerical model cannot simulate microfractures emerged inside the experimental setup by steam injection. While these fractures support steam penetration faster than expected in the horizontal direction, the simulation results are more conservative. The distinctive shape of the developing steam chamber is clearly observed in temperature profiles obtained from the numerical simulation. However, this shape is not so obvious in the results of experimental temperature profiles. The possible explanation for this observation might be an insufficient number of thermocouples used far away from the wells at the 2D SAGD experimental setup.

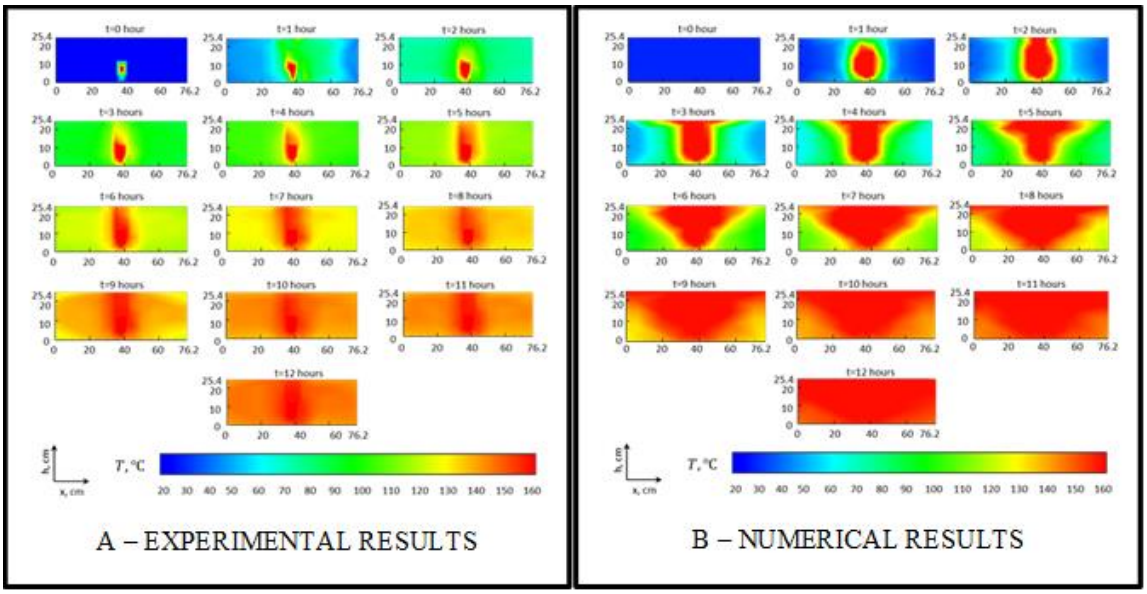

Fig. 39—Hourly change of temperature profiles for SAGD1 obtained during experiments (A) and numerical studies (B).

The same model used for SAGD1 was used to model the HWI case. Because injection temperature could not be kept constant during the experiment, an average value of steam quality (60%) was assigned for the injection well to mimic the total enthalpy introduced to the system. History-matched results for cumulative oil and water productions are provided in **Fig. 40** and **Fig. 41**, respectively. As mentioned for the numerical simulation results of SAGD1, higher cumulative water production is observed for the HWI numerical simulation. The oil saturation around the injection wellbore at the end of the numerical simulation (35%) is close to the ROS obtained postmortem (39%) (**TABLE 15**). The reliability of selected relative permeability curves and temperature dependence end point relative permeabilities are validated second time with the simulation results obtained both for SAGD1 and HWI.

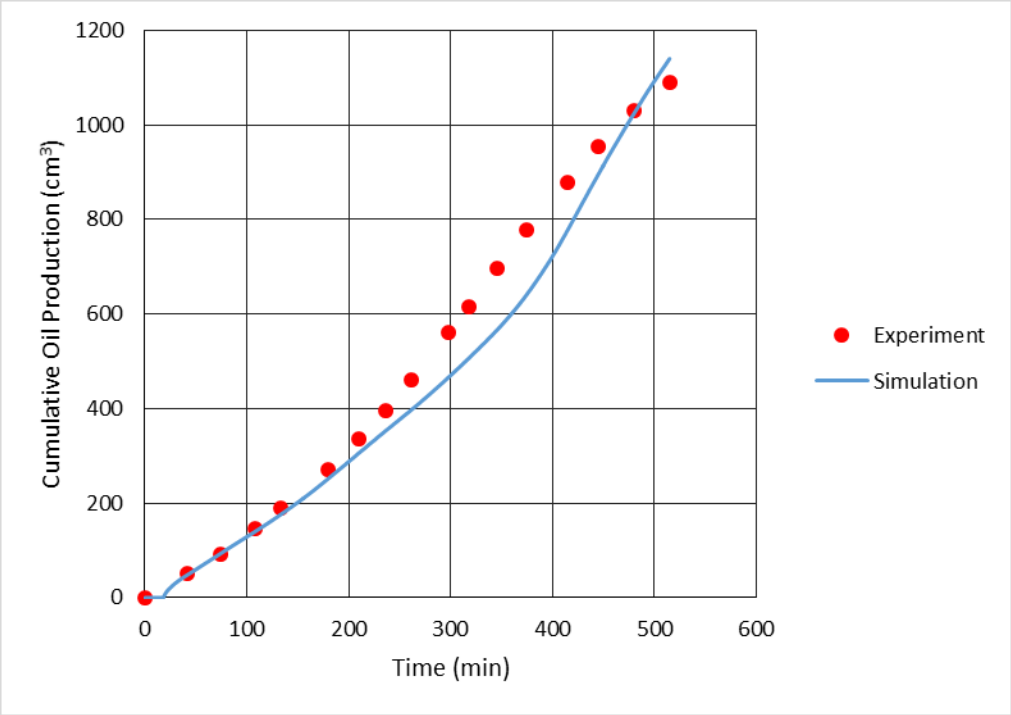

Fig. 40—Cumulative oil production vs. time results of HWI experiment and simulation.

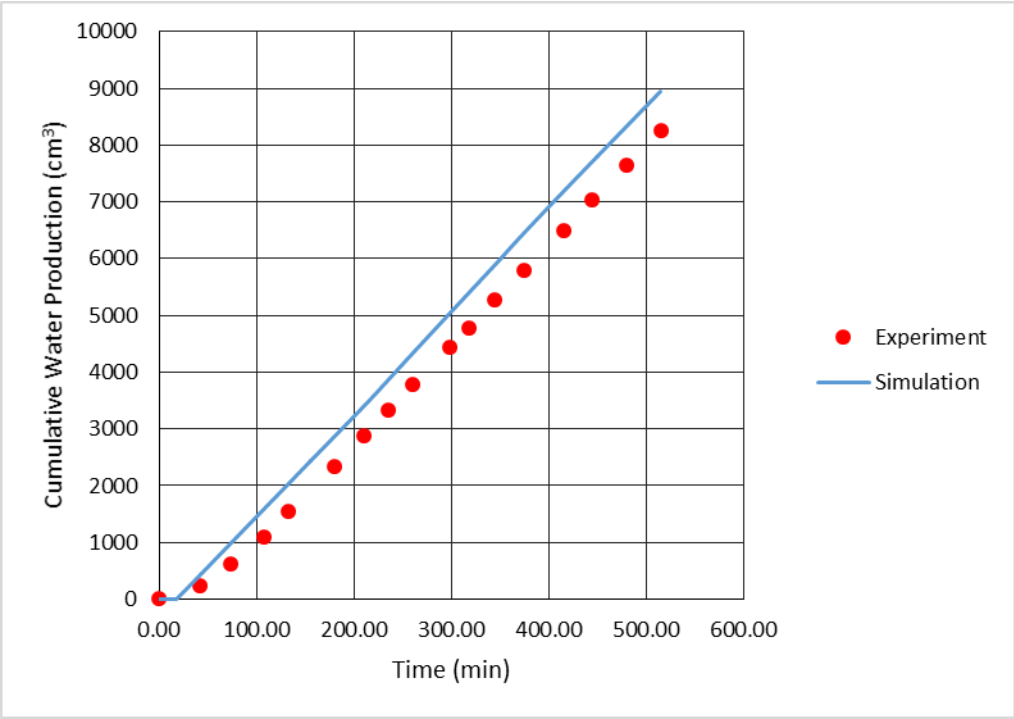

Fig. 41—Cumulative water production vs. time results of HWI experiment and simulation.

The hourly temperature profiles of both the experiment and simulation are given in **Fig. 42.** Because an average value of injection temperature and steam quality was assigned to mimic the experimental conditions in this numerical simulation, the temperature propagation in numerical simulation results is faster than experimental results. Note that thermocouple numbers in the experimental setup are not sufficient far away from the wells, and injection temperature fluctuates continuously throughout the

experiment. Therefore, slight differences can be observed on the temperature profiles of HWI experiment and its numerical simulation.

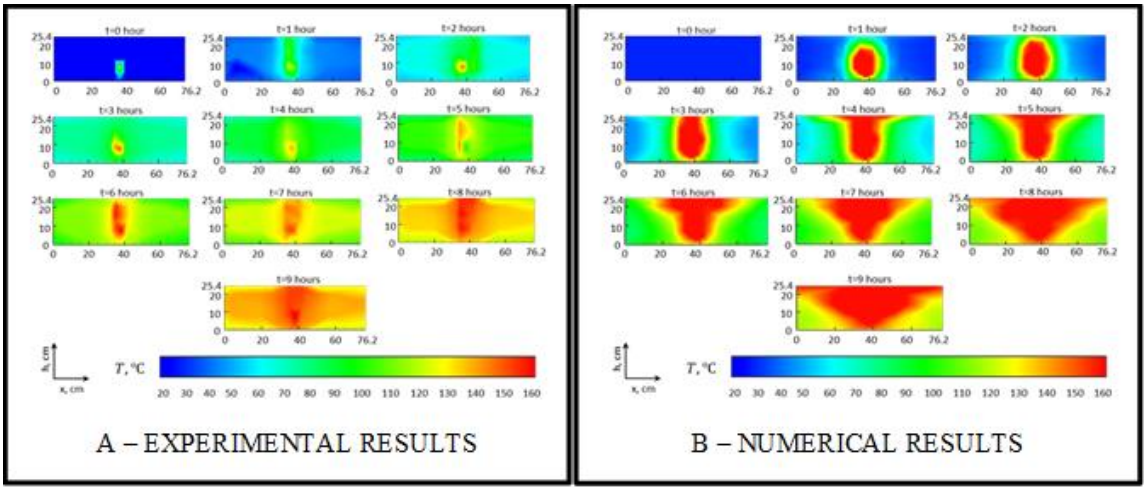

Fig. 42—Hourly change temperature profile comparison for HWI obtained during experiments (A) and numerical studies (B).

The last history-match was obtained for SAGD2, which was prepared with clay type 2. Because the only parameter varied between base case (SAGD1) to SAGD2 is the clay type, the base case model was used to simulate SAGD2 experiment. The relative permeability endpoint saturation is used as a tuning parameter in this numerical run. In addition, the experimentally observed cementing tendency (**Fig. 23**) for clay type 2 was introduced to the numerical model by decreasing the effective permeability from 80 to 60 Darcies. As mentioned in the previous section, no oil production is observed during the first 90 minutes after steam injection began. Therefore, the history-matching was conducted on the modified experimental results (**Fig. 36**). It was assumed that steam injection was started in the 90th minute of the experiment. Some water was produced

during the 90th minute of the experiment, but according to the assumption, this early water production is omitted. The history-matched results of cumulative oil production and cumulative water production vs. time are shown in **Fig. 43** and **Fig. 44,** respectively. The oil saturation of the grids around the injection well at the end of the simulation (55%) is close to the ROS analysis results postmortem (61%) (**TABLE 15**).

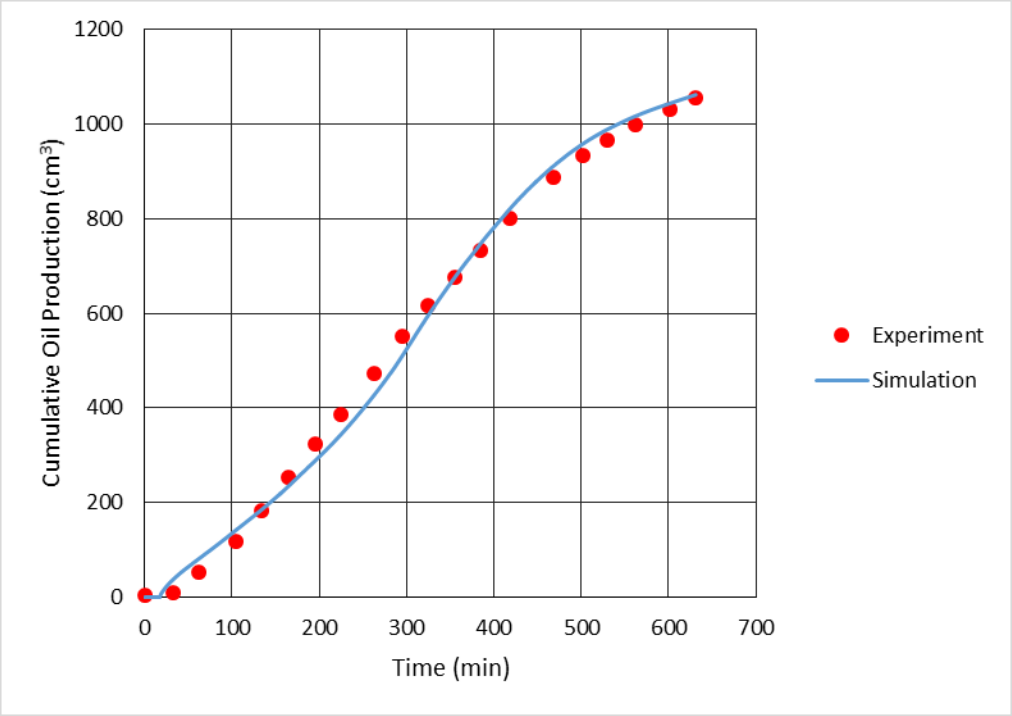

Fig. 43—Cumulative oil production vs. time results of SAGD2 experiment and simulation.

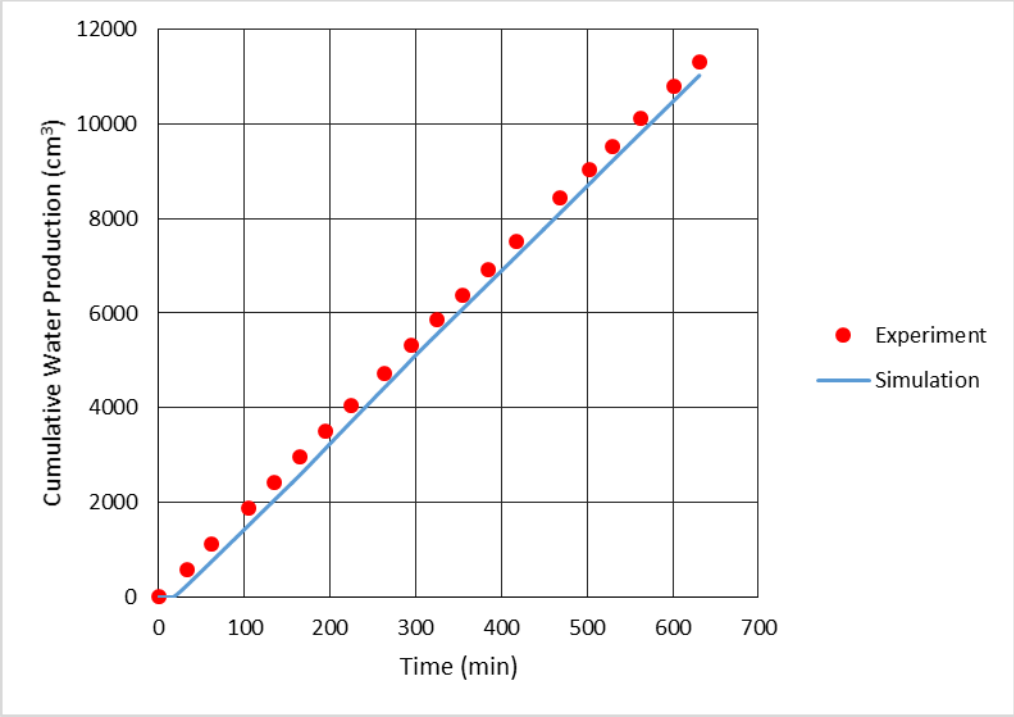

Fig. 44—Cumulative water production vs. time results of SAGD2 experiment and simulation.

Because there was no oil production in the first 90 minutes of the experiment, temperature profiles comparison also delayed for 90 minutes. The results were reasonably matched after 2 hours. The outside of the steam chamber zone is warmer in the experimental results than numerical simulation results in early time steps. Injected steam during the first 90 minutes of the experiment is most probably the cause of this temperature difference. Faster horizontal temperature propagation and slower temperature dispersion in the vertical direction are observed for SAGD2 when compared with its numerical simulation. This behavior was also monitored during the numerical simulation of SAGD1.

The hourly temperature profiles of the SAGD2 experiment numerical simulation are given in **Fig. 45.**

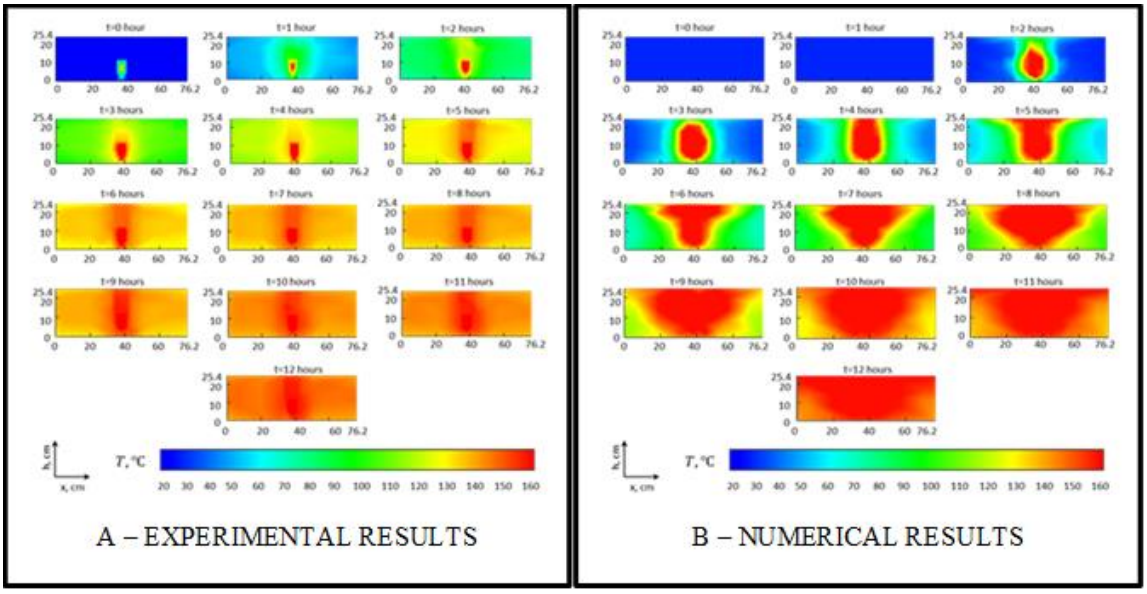

Fig. 45—Hourly change of temperature profiles for SAGD2 obtained during experiments (A) and numerical studies (B).

The accuracy of our simulation studies has been validated with three experiments. Therefore, relative permeability graphs presented in **Fig. 31** through **Fig. 34** and temperature dependency of relative permeability end points given in **TABLE 22,** can be used for the upscaling of SAGD process.

4.3 Sensitivity Studies

Sensitivity studies were conducted to check any numerical error caused by grid size selection and to understand the relationship between permeability and cumulative oil production. Temperature-dependent relative permeability endpoint saturations were also investigated with a sensitivity study to understand which parameters have a greater influence on oil production characteristics.

4.3.1 Grid Size Sensitivity

Optimum grid size was selected according to the results of a grid-size sensitivity study. Grid systems of 4 × 80 × 29, 4 × 60 × 29, and 4 × 40 × 29 were tested to find the appropriate number of grid blocks with minimizing the numerical errors. The cumulative oil production results of these three cases are given in **Fig. 46.** Grid sensitivity results found grid system 4 × 60 × 29 to be the best candidate for this numerical simulation study because the simulation result is almost the same with a finer grid option, and it has less computation time than the 4 × 80 × 29 grid system.

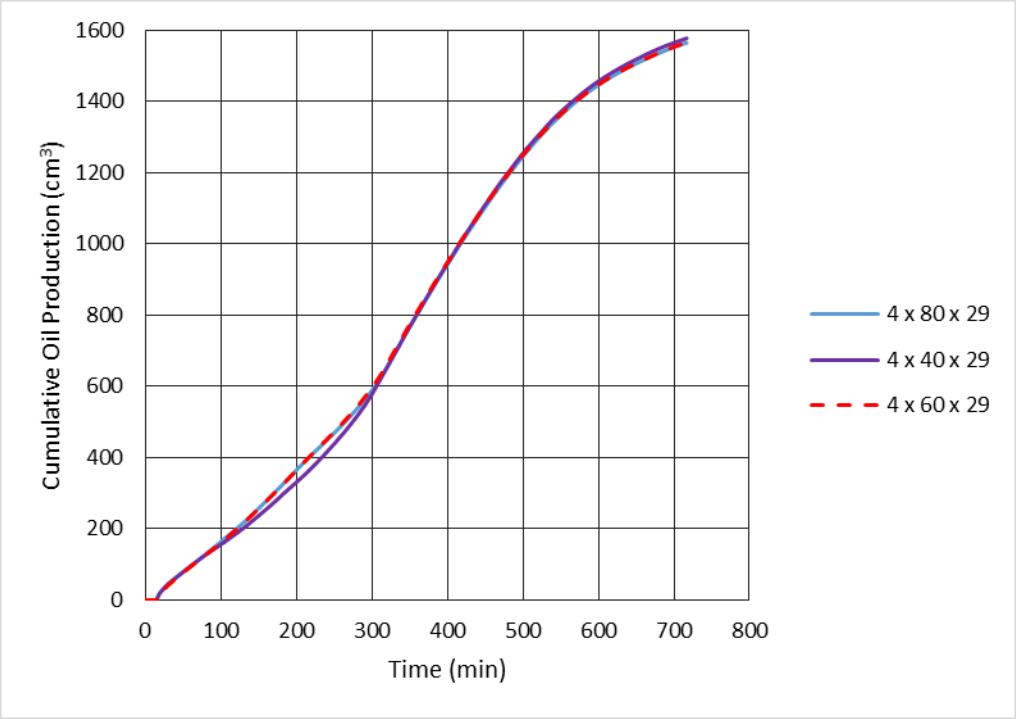

Fig. 46—Effect of grid size on cumulative oil production.

4.3.2 Permeability Sensitivity

Because the permeability value was not measured experimentally, the permeability influence on numerical simulation results was investigated with series of sensitivity studies. Permeability values of 10, 60, 80, 100, and 150 Darcy were investigated with a sensitivity study. The cumulative oil production results are compared in **Fig. 47.** Permeability value significantly affects the cumulative oil production characteristics and oil recovery.

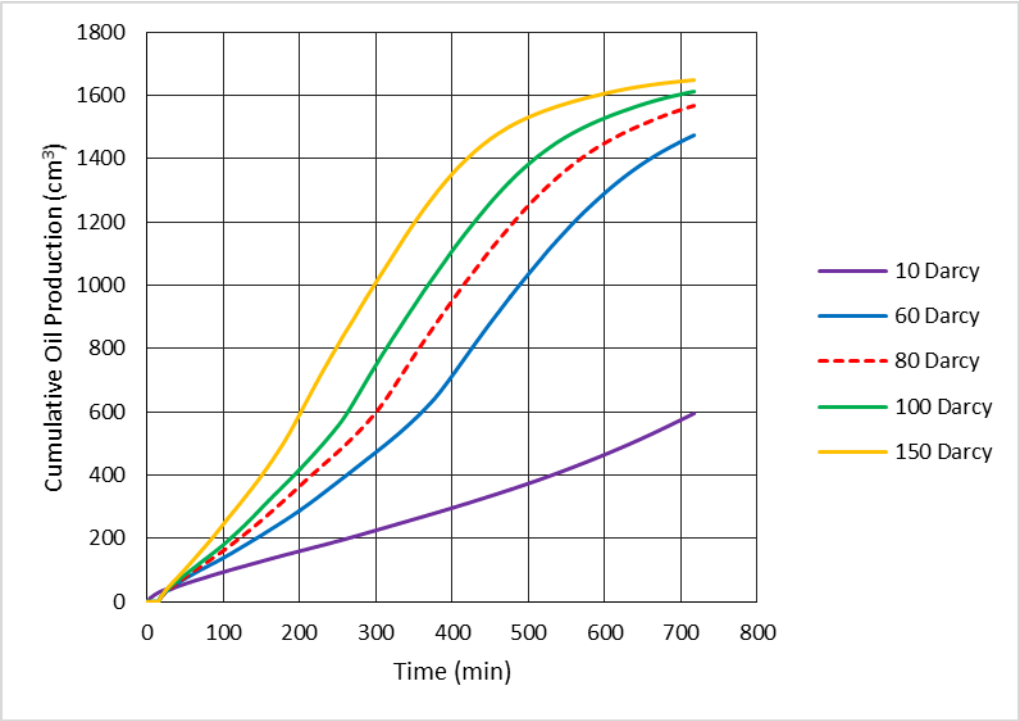

Fig. 47—Effect of permeability on the cumulative oil production.

4.3.3 Relative Permeability Endpoint Sensitivity

Effect of temperature dependence of relative permeability end points has been investigated with series of sensitivity studies. The endpoint saturations were slightly changed for each temperature value to better observe their impact on cumulative oil production characteristics. The changes applied in each numerical run are summarized in **TABLE 24.**

TABLE 24—SENSITIVITY STUDIES ON TEMPERATURE-DEPENDENT RELATIVE PERMEABILITY ENDPOINTS

Experiment Name	Temperature (degC)	S_{wr} (fraction)	S_{orw} (fraction)	S_{org} (fraction)
Base Case (SAGD1)	25	0.05	0.4	0.4
	180	0.2	0.3	0.35
RP1	25	0.05	**0.45**	0.4
	180	0.2	0.3	0.35
RP2	25	0.05	**0.35**	0.4
	180	0.2	0.3	0.35
RP3	25	0.05	0.4	**0.45**
	180	0.2	0.3	0.35
RP4	25	0.05	0.4	**0.35**
	180	0.2	0.3	0.35
RP5	25	**0.1**	0.4	0.4
	180	0.2	0.3	0.35
RP6	25	**0**	0.4	0.4
	180	0.2	0.3	0.35
RP7	25	0.05	0.4	0.4
	180	0.2	**0.35**	0.35
RP8	25	0.05	0.4	0.4
	180	0.2	**0.25**	0.35
RP9	25	0.05	0.4	0.4
	180	0.2	0.3	**0.4**
RP10	25	0.05	0.4	0.4
	180	0.2	0.3	**0.3**
RP11	25	0.05	0.4	0.4
	180	**0.25**	0.3	0.35
RP12	25	0.05	0.4	0.4
	180	**0.15**	0.3	0.35

The comparison of cumulative oil productions by changing S_{orw}, S_{org}, and S_{wr} values are shown in **Fig. 48, Fig. 49,** and **Fig. 50,** respectively. The changes in temperature-dependent endpoints of ROS for water injection (S_{orw}) and IWS (S_{wr}) have a very small impact on cumulative oil production. On the other hand, ROS for gas injection

has a significant effect on late-time cumulative oil production. Specifically, ROS for gas injection at an elevated temperature endpoint is a very important parameter for cumulative oil production (**Fig. 49**).

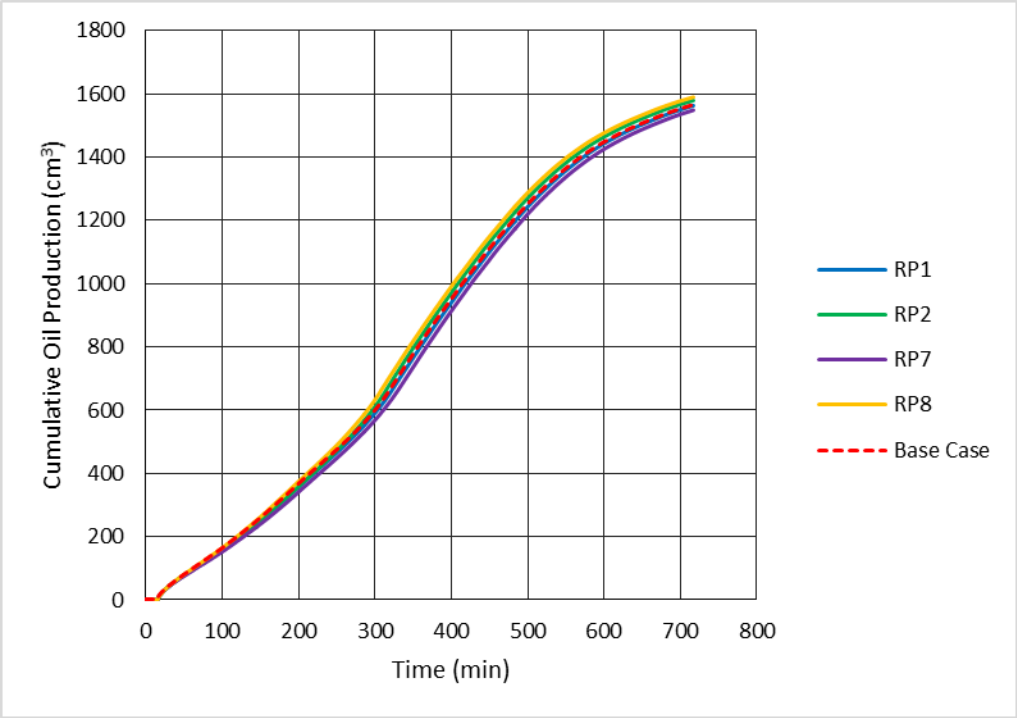

Fig. 48—Effect of temperature dependence of S_{orw} on cumulative oil production.

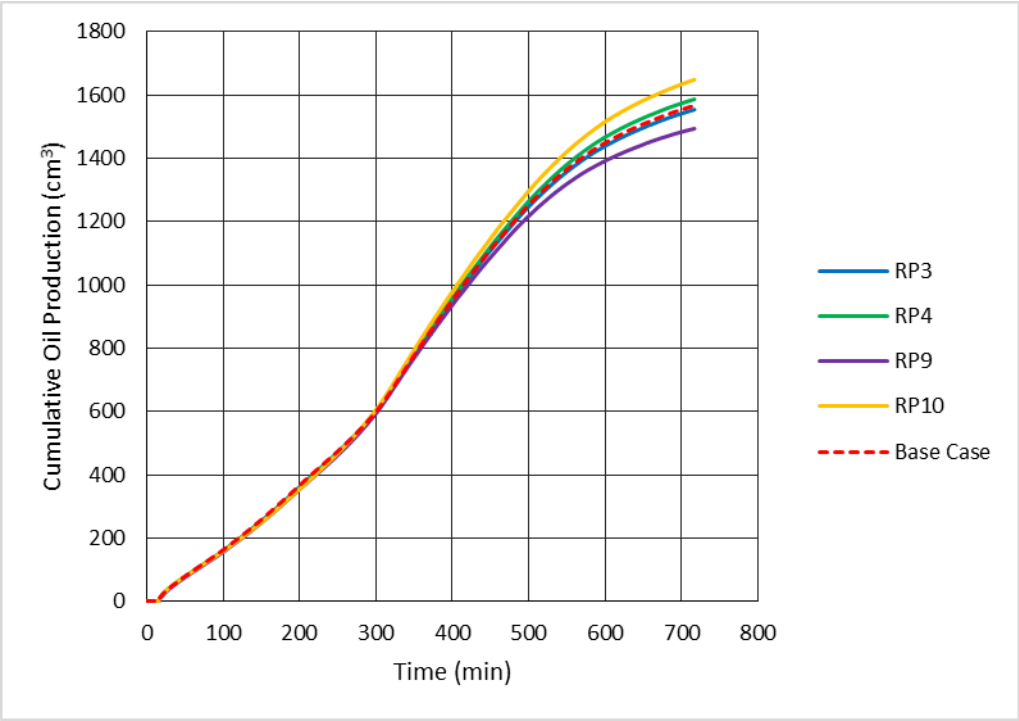

Fig. 49—Effect of temperature dependence of S_{org} on cumulative oil production.

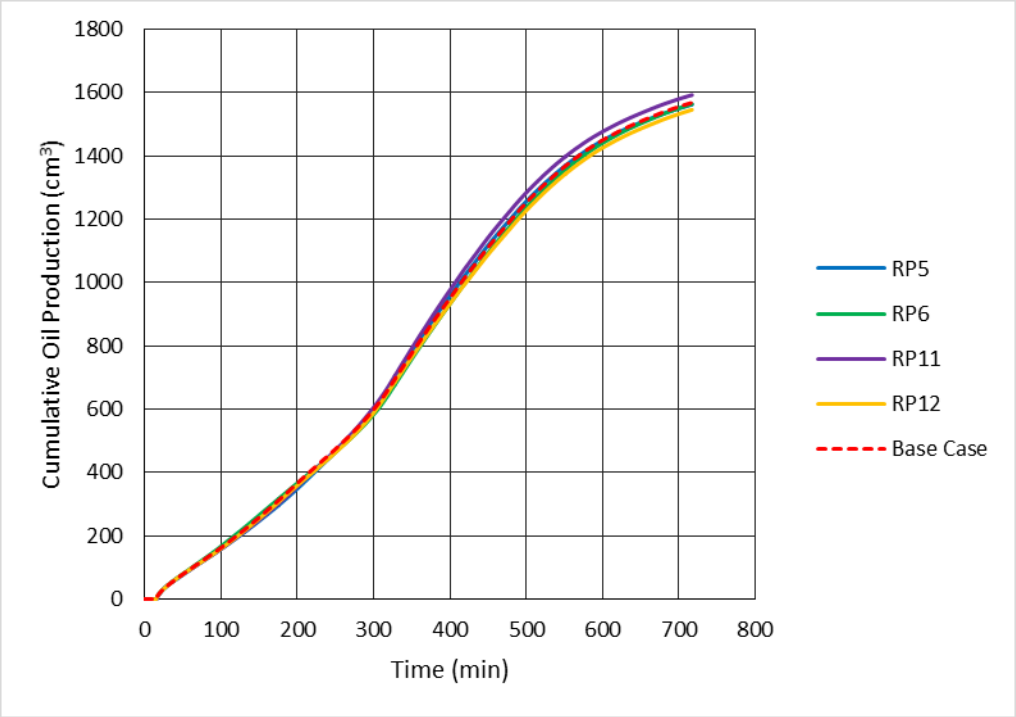

Fig. 50— Effect of temperature dependence of S_{wr} on cumulative oil production.

4.4 Conclusions

The experimental results belong to three SAGD experiments were numerically simulated by using a reservoir simulator. Temperature-dependent relative permeability curves and endpoint saturations were determined experimentally. Data files were constructed by combining literature data with experimental results.

More than 600 simulation runs were conducted to obtain a history-match between experimental results and numerical simulation results. Permeability, relative permeabilities, and temperature-dependent saturation endpoints were used as tuning parameters. Well constraints were 18 cc/min of cold water–equivalent steam injection for

the injector well and 618.5-kPa [75-psig]-minimum bottomhole pressure for the producer well.

Cumulative oil production, cumulative water production, and hourly temperature profiles were history-matching parameters that were reasonably matched for each of the experiments. Thus, it can be said that the relative permeability curves, which were prepared by using the results of wettability analyses, represent the real values.

After history-match was obtained for the numerical model, several sensitivity studies were conducted on parameters influencing cumulative oil production (grid size, permeability, and saturation endpoints). The results of this study show that the grid size used in the numerical model is the most optimal option. In addition, permeability reduction causes a decrease in oil recovery. The sensitivity study on saturation endpoints shows that the most important parameter changing cumulative oil production significantly is ROS for gas injection (S_{org}) for high-temperature values.

CHAPTER V

CONCLUSIONS

SAGD is one of the most successful EOR techniques, and efforts to develop this technique continue. A less-investigated part of this technique is its wettability. Wettability is one of the most crucial parameters directly affecting reservoir behavior and its ultimate recovery. Therefore, it is very important to understand the wettability behavior of SAGD-applied reservoirs to better interpret the performance of the process.

Three SAGD experiments were conducted with a 2D SAGD experimental setup and were investigated extensively for identifying wettability characteristics with additional experimental analyses.

To reach this goal, the produced oil, produced water, and spent rock samples were subjected additional analyses with contact angle, zeta potential, interfacial/surface tension, residual fluid saturation, and XRD measurements. The results of these measurements were studied, and wettability characteristics of postmortem samples of each experiment were determined. Possible causes of these wettability behaviors were explained and supported with the particle size analyses and SEM images. After that, the results of these investigations were used as input data for numerical model.

The results of wettability studies were combined with relative permeability endpoints, and more representative relative permeability values were obtained. The history-matched numerical simulation outputs are in a good agreement with experimental

results. For tuning parameters, sensitivity studies were also conducted to study the impact of each parameter on the simulation results.

The general conclusions reached at the end of these studies are as follows:

1. Contact angle measurements show that increasing temperature triggers wettability to more a water-wet state, and illite-containing clays (clay type 2) in oil sands yield more oil-wet rock samples after steam treatment.
2. Asphaltene wettability change, clay migration, and permeability reduction due to cementation could be possible reasons for different wettability characteristics.
3. Increasing temperature yields a more water-wet state, and this behavior was introduced to the numerical model by changing temperature-dependent saturation endpoints. The oil-wet behavior of SAGD2 postmortem samples was also put into the numerical model by changing saturation endpoints of relative permeability curves.
4. The combination of post-experimental and numerical simulation study results gave reliable relative permeability curve assumptions, which was validated with history matching. HWI and SAGD1 experiments were perfectly simulated with one data file by changing only the injected steam quality. SAGD1 and SAGD2 numerical models were history-matched with experimental data by changing relative permeability curves and permeability according to the results of wettability measurements of postmortem samples.

REFERENCES

Abdul-Hamid, O. S., 2013, World Oil Outlook 2013, *in* J. Griffin, A.-M. Fantini, and K. Aylward-Marchant, eds., World Oil Outlook, Austria, Organization of the Petroleum Exporting Countries.

Adams, J., S. Larter, B. Bennett, and H. Huang, 2012, Oil Charge Migration in the Peace River Oil Sands and Surrounding Region, *in* E. MacPherson, ed., CSPG/CSEG/CWLS GeoConvention 2012 Vision, Canada.

Akbarzadeh, K., A. Hammami, A. Kharrat, D. Zhang, S. Allenson, J. Creek, S. Kabir, A. J. Jamaluddin, A. G. Marshall, R. P. Rodgers, O. C. Mullins, and T. Solbakken, 2007, Asphaltenes-Problematic but Rich in Potential: Oilfield Review, v. 19, p. 22-43.

Alboudwarej, H., J. Felix, S. Taylor, R. Badry, C. Bremner, B. Brough, and C. Skeates, 2006, Highlighting Heavy Oil: Oilfield Review, v. 18, p. 34-53.

Alotaibi, M. B., R. M. Azmy, and H. A. Nasr-El-Din, 2010, Wettability Studies Using Low-Salinity Water in Sandstone Reservoirs, Offshore Technology Conference, Houston, Texas, USA.

Alotaibi, M. B., and H. A. Nasr-El-Din, 2011, Electrokinetics of Limestone Particles and Crude-Oil Droplets in Saline Solutions: SPE Reservoir Evaluation & Engineering, v. 14, p. 604-611.

Anderson, W. G., 1986, Wettability Literature Survey- Part 1: Rock/Oil/Brine Interactions and the Effects of Core Handling on Wettability: Journal of Petroleum Technology, v. 38, p. 1,125-1,144.

Anderson, W. G., 1987, Wettability Literature Survey Part 5: The Effects of Wettability on Relative Permeability: Journal of Petroleum Technology, v. 39, p. 1,453-1,468.

Ashrafi, M., Y. Souraki, H. Karimaie, O. Torsaeter, and J. Kleppe, 2011, Numerical Simulation Study of SAGD Experiment and Investigating Possibility of Solvent Co-Injection, SPE Enhanced Oil Recovery Conference, Kuala Lumpur, Malaysia, Society of Petroleum Engineers.

Bahlani, A. M. M. A., and T. Babadagli, 2008, A Critical Review of the Status of SAGD: Where Are We and What Is Next?, SPE Western Regional and Pacific Section AAPG Joint Meeting, Bakersfield, California, USA, Society of Petroleum Engineers.

Baker, L. E., 1988, Three-Phase Relative Permeability Correlations, SPE Enhanced Oil Recovery Symposium, Tulsa, Oklahoma

Bantignies, J.-L., C. C. D. Moulin, and H. Dexpert, 1997, Wettability Contrasts in Kaolinite and Illite Clays: Characterization by Infrared and X-ray Absorption Spectroscopies: Le Journal de Physique IV, v. 7, p. C2-867-C2-869.

Bayliss, P., and A. Levinson, 1976, Mineralogical Review of the Alberta Oil Sand Deposits (Lower Cretaceous, Mannville Group): Bulletin of Canadian Petroleum Geology, v. 24, p. 211-224.

Bell, S., R. Tyshkewich, D. MacKenzie, J. Watson, C. Ma, F. V. Beek, and B. Blachford, 2010, Peace River In Situ Oil Sands Progress Report, Shell Peace River 2010 Annual Performance Review.

Bennion, D. B., F. B. Thomas, B. Schulmeister, and T. Ma, 2006, A Correlation of the Low and High Temperature Water-Oil Relative Permeability Characteristics of Typical Western Canadian Unconsolidated Bitumen Producing Formations, Canadian International Petroleum Conference, Calgary, Alberta, Petroleum Society of Canada.

Bennion, D. W., R. G. Moore, and F. B. Thomas, 1985, Effect of Relative Permeability on The Numerical Simulation of The Steam Stimulation Process: Journal of Canadian Petroleum Technology, v. 24, p. 40-44.

Butler, R. M., 1994, Steam-Assisted Gravity Drainage: Concept, Development, Performance and Future: Journal of Canadian Petroleum Technology, v. 33, p. 44-50.

Chow, L., and R. M. Butler, 1996, Numerical Simulation of The Steam-Assisted Gravity Drainage Process (SAGD): Journal of Canadian Petroleum Technology, v. 35, p. 55-62.

Chung, K. H., 1988, Heavy Oil Recovery By The Steam-Assisted Gravity Drainage Process: Ph.D. thesis, University of Calgary.

Civan, F., 2004, Temperature Dependence of Wettability Related Rock Properties Correlated by the Arrhenius Equation: Petrophysics, v. 45, p. 350-362.

Clelland, W. D., and T. W. Fens, 1991, Automated Rock Characterization with SEM/Image-Analysis Techniques: SPE Formation Evaluation, v. 6, p. 437-443.

Closmann, P. J., M. H. Waxman, and C. T. Deeds, 1988, Steady-State Tar/Water Relative Permeabilities in Peace River Cores at Elevated Temperature: SPE Reservoir Engineering, v. 3, p. 76-80.

Craig, F. F., 1976, The Reservoir Engineering Aspects of Waterflooding: New York, Henry L. Doherty Memorial Fund of AIME, Society of Petroleum Engineers of AIME, 134 p.

Crocker, M. E., and L. M. Marchin, 1988, Wettability and Adsorption Characteristics of Crude-Oil Asphaltene and Polar Fractions: Journal of Petroleum Technology, v. 40, p. 470-474.

Deutsch, C., and J. McLennan, 2005, Guide to SAGD (Steam Assisted Gravity Drainage) Reservoir Characterization Using Geostatistics: Centre for Computational Excellence (CCG), Guidebook Series Vol. 3, University of Alberta, April 2003.

Dubey, S. T., and M. H. Waxman, 1991, Asphaltene Adsorption and Desorption from Mineral Surfaces: SPE Reservoir Engineering, v. 6, p. 389-395.

Egermann, P., G. Renard, and E. Delamaide, 2001, SAGD Performance Optimization Through Numerical Simulations: Methodology and Field Case Example, SPE International Thermal Operations and Heavy Oil Symposium, Porlamar, Margarita Island, Venezuela, Society of Petroleum Engineers.

EIA, 2012, Canada Country Report, U.S. Energy Information Administration, <http://www.eia.gov/countries/analysisbriefs/Canada/canada.pdf>.

Frizzell, D. F., 1990, Analysis of 15 Years of Thermal Laboratory Data: Relative Permeability and Saturation Endpoint Correlations for Heavy Oils, SPE Annual Technical Conference and Exhibition, New Orleans, Louisiana, 1990 Copyright 1990, Society of Petroleum Engineers Inc.

Glandt, C. A., and J. D. Malcolm, 1991, Numerical Simulation of Peace River Recovery Processes, SPE Annual Technical Conference and Exhibition, Dallas, Texas, 1991 Copyright 1991, Society of Petroleum Engineers Inc.

Glover, D. P., 2014, Wettability, Formation Evaluation MSc Course Notes.

Good, W. K., C. Rezk, and B. D. Felty, 1997, Possible Effects of Gas Caps on SAGD Performance, The Alberta Environment and Alberta Energy Utilities Board.

Good, W. K., J. D. Scott, and R. W. Luhning, 1994, [7]4 Review and Assessment of Steam Assisted Gravity Drainage (SAGD) Applications in Canada, 14th World Petroleum Congress, Stavanger, Norway World Petroleum Congress.

Government, A., 2013a, Alberta's Oil Sands, <http://www.energy.alberta.ca/OilSands/pdfs/FactSheet_OilSands.pdf>.

Government, A., 2013b, In-Situ Process Steam Assisted Gravity Drainage (SAGD), <http://www.energy.alberta.ca/OilSands/pdfs/FS_SAGD.pdf>.

Grate, J. W., K. J. Dehoff, M. G. Warner, J. W. Pittman, T. W. Wietsma, C. Zhang, and M. Oostrom, 2012, Correlation of Oil–Water and Air–Water Contact Angles of

Diverse Silanized Surfaces and Relationship to Fluid Interfacial Tensions: Langmuir, v. 28, p. 7182-7188.

Greene, D. L., J. L. Hopson, and J. Li, 2006, Have We Run Out of Oil Yet? Oil Peaking Analysis from an Optimist's Perspective: Energy Policy, v. 34, p. 515-531.

Hamm, R. A., and T. S. Ong, 1995, Enhanced Steam-assisted Gravity Drainage: A New Horizontal Well Recovery Process for Peace River, Canada: Journal of Canadian Petroleum Technology, v. 34, p. 33-40.

Hascakir, B., and A. R. Kovscek, 2010, Reservoir Simulation of Cyclic Steam Injection Including the Effects of Temperature Induced Wettability Alteration, SPE Western Regional Meeting, Anaheim, California, USA Society of Petroleum Engineers.

Hein, F. J., and R. A. Marsh, 2008, Regional Geologic Framework, Depositional Models and Resource Estimates of the Oil Sands of Alberta, Canada, World Heavy Oil Congress, Canada, dmg world media, Calgary, AB (Canada); China National Petroleum Corporation - Alberta Petroleum Centre, Beijing (China); dmg world media, Calgary, AB (Canada), p. page(s) 1-9.

Hematfar, V., B. B. Maini, and Z. J. Chen, 2013, Influence of Clay Minerals and Water Film Properties on In-Situ Adsorption of Asphaltene, SPE Heavy Oil Conference-Canada, Calgary, Alberta, Canada, Society of Petroleum Engineers.

Heron, C. A., H. F. Thimm, L. Sullivan, and I. K. Atkinson, 2008, NCG Behaviour in SAGD - A Numerical Simulation Analysis, International Thermal Operations

and Heavy Oil Symposium, Calgary, Alberta, Canada, Society of Petroleum Engineers.

Hussain, S. A., Ş. Demirci, and G. Özbayoğlu, 1996, Zeta Potential Measurements on Three Clays from Turkey and Effects of Clays on Coal Flotation: Journal of Colloid and Interface Science, v. 184, p. 535-541.

IEA, 2011, World Energy Outlook 2011, *in* M. v. d. Hoeven, ed., France, International Energy Agency.

International, A., 2011, Test Method for Characteristic Groups in Rubber Extender and Processing Oils and Other Petroleum-Derived Oils by the Clay-Gel Absorption Chromatographic Method.

Jamaluddin, A. K. M., J. Creek, C. S. Kabir, J. D. McFadden, apos, D. Cruz, J. Manakalathil, N. Joshi, and B. Ross, 2002, Laboratory Techniques to Measure Thermodynamic Asphaltene Instability: Journal of Canadian Petroleum Technology, v. 41, p. 44-52.

Jiang, T., G. J. Hirasaki, and C. A. Miller, 2010, Characterization of Kaolinite ζ Potential for Interpretation of Wettability Alteration in Diluted Bitumen Emulsion Separation†: Energy & Fuels, v. 24, p. 2350-2360.

Jimenez, J., 2008, The Field Performance of SAGD Projects in Canada, International Petroleum Technology Conference, Kuala Lumpur, Malaysia, International Petroleum Technology Conference.

Kaya, A., A. H. Oren, and Y. Yukselen, 2003, Settling Behavior And Zeta Potential of Kaolinite In Aqueous Media, The Thirteenth International Offshore and Polar

Engineering Conference, Honolulu, Hawaii, USA International Society of Offshore and Polar Engineers.

Kokal, S. L., and S. G. Sayegh, 1995, Asphaltenes: The Cholesterol of Petroleum, Middle East Oil Show, Bahrain, Society of Petroleum Engineers.

Kwan, M. Y., 1998, Measuring Wettability of Unconsolidated Oil Sands Using the USBM Method: Journal of Petroleum Science and Engineering, v. 21, p. 61-78.

Law, D. H. S., T. N. Nasr, and W. K. Good, 2003, Lab-Scale Numerical Simulation of SAGD Process in the Presence of Top Thief Zones: A Mechanistic Study: Journal of Canadian Petroleum Technology, v. 42, p. 29-35.

Lei, Q., J. Y. J. Wang, and I. D. Gates, 2010, Impact of Oil-Water Relative Permeability Curves on SAGD Behaviour, International Oil and Gas Conference and Exhibition in China, Beijing, China, Society of Petroleum Engineers.

Leverett, M. C., 1939, Flow of Oil-Water Mixtures Through Unconsolidated Sands: Transactions of the AIME, v. 132, p. 149-171.

Li, K., and R. N. Horne, 2003, Numerical Simulation with Input Consistency between Capillary Pressure and Relative Permeability, SPE Reservoir Simulation Symposium, Houston, Texas Society of Petroleum Engineers.

Liu, J., Z. Xu, and J. Masliyah, 2005, Interaction Forces in Bitumen Extraction from Oil Sands: Journal of Colloid and Interface Science, v. 287, p. 507-520.

Liu, J., Z. Zhou, Z. Xu, and J. Masliyah, 2002, Bitumen–Clay Interactions in Aqueous Media Studied by Zeta Potential Distribution Measurement: Journal of Colloid and Interface Science, v. 252, p. 409-418.

Maini, B. B., and T. Okazawa, 1987, Effects Of Temperature On Heavy Oil-Water Relative Permeability Of Sand: Journal of Canadian Petroleum Technology, v. 26, p. 33-41.

Mattax, C., and R. Dalton, 1990, Reservoir Simulation: Henry L. Doherty Series, Monograph, v. 13: Richardson, TX, Society of Petroleum Engineers, 172 p.

McCaffery, F. G., and D. W. Bennion, 1974, The Effect Of Wettability On Two-Phase Relative Permeabilities: Journal of Canadian Petroleum Technology, v. 13, p. 42-53.

Mukhametshina, A., 2013, Reducing the Environmental Impact of Bitumen Extraction with ES-SAGD Process: MSc. thesis, Texas A&M University.

Mungan, N., 1972, Relative Permeability Measurements Using Reservoir Fluids: Society of Petroleum Engineers Journal, v. 12, p. 398-402.

Mungan, N., 1981, Enhanced Oil Recovery Using Water as a Driving Fluid: World Oil;(United States), v. 193, p. 69-84.

Nakornthap, K., and R. D. Evans, 1986, Temperature-Dependent Relative Permeability and Its Effect on Oil Displacement by Thermal Methods: SPE Reservoir Engineering, v. 1, p. 230-242.

Nasr, T. N., and O. R. Ayodele, 2005, Thermal Techniques for the Recovery of Heavy Oil and Bitumen, SPE International Improved Oil Recovery Conference in Asia Pacific, Kuala Lumpur, Malaysia, Society of Petroleum Engineers.

Nasralla, R. A., and H. A. Nasr-El-Din, 2011, Impact of Electrical Surface Charges and Cation Exchange on Oil Recovery by Low Salinity Water, SPE Asia Pacific Oil

and Gas Conference and Exhibition, Jakarta, Indonesia Society of Petroleum Engineers.

OilSandsReview, 2014, Key Oil Sands Projects, <http://navigator.oilsandsreview.com/listing>.

Owens, W. W., and D. L. Archer, 1971, The Effect of Rock Wettability on Oil-Water Relative Permeability Relationships: Journal of Petroleum Technology, v. 23, p. 873-878.

Parra-Barraza, H., D. Hernández-Montiel, J. Lizardi, J. Hernández, R. Herrera Urbina, and M. A. Valdez, 2003, The Zeta Potential and Surface Properties of Asphaltenes Obtained with Different Crude oil/n-heptane Proportions: Fuel, v. 82, p. 869-874.

Polikar, M., F. Ferracuti, V. Decastro, R. Puttagunta, and S. M. F. Ali, 1986, Effect Of Temperature On Bitumen-Water End Point Relative Permeabilities And Saturations: Journal of Canadian Petroleum Technology, v. 25, p. 44-50.

Pollkar, M., V. R. Puttagunta, V. Decastro, and S. M. F. Ali, 1989, Relative Permeability Curves for Bitumen and Water in Oil Sand Systems: Journal of Canadian Petroleum Technology, v. 28, p. 93-99.

Poston, S. W., S. Ysrael, A. K. M. S. Hossain, and E. F. Montgomery III, 1970, The Effect of Temperature on Irreducible Water Saturation and Relative Permeability of Unconsolidated Sands: Society of Petroleum Engineers Journal, v. 10, p. 171-180.

Prats, M., 1982, Thermal Recovery: New York, H.L. Doherty Memorial Fund of AIME, Society of Petroleum Engineers of AIME 283 p.

Quan, X., W. Jiazhong, Q. Jishun, L. Qingjie, M. Desheng, L. Li, and L. Manli, 2012, Investigation of Electrical Surface Charges and Wettability Alteration by Ions Matching Waterflooding, International Symposium of the Society of Core Analysts, Aberdeen, Scotland.

Rajnauth, J. J., 2012, Is It Time to Focus on Unconventional Resources?, SPETT 2012 Energy Conference and Exhibition, Port-of-Spain, Trinidad, Society of Petroleum Engineers.

Rao, D. N., 2002, Correlation of Oil-Water Flow Behaviour in Reservoir Rocks With Dynamic Contact Angles: Journal of Canadian Petroleum Technology, v. 41, p. 31-38.

Riddick, T., 1968, Control of Colloid Stability Through Zeta Potential: with a Closing Chapter on its Relationship to Cardiovascular Disease, Zeta-Meter: Inc, Wynnewood, PA.

Rosenberg, M., I. J. Kopelman, and Y. Talmon, 1985, A Scanning Electron Microscopy Study of Microencapsulation: Journal of Food Science, v. 50, p. 139-144.

Sasaki, K., S. Akibayahsi, N. Yazawa, Q. Doan, and S. M. F. Ali, 2001, Numerical and Experimental Modelling of the Steam Assisted Gravity Drainage (SAGD): Journal of Canadian Petroleum Technology, v. 40, p. 44-50.

Shin, H., 2006, Experimental and Numerical Investigation of the Fast-SAGD Process: Ph.D. thesis, University of Alberta (Canada), Ann Arbor, 308-308 p. p.

Shuhua, G., and Q. Jialin, 1997, Micro-Structure Model of Some Chinese Oil Sand: Petroleum Science and Technology, v. 15, p. 857-872.

Souraki, Y., M. Ashrafi, H. Karimaie, and O. Torsaeter, 2012, Experimental Analyses of Athabasca Bitumen Properties and Field Scale Numerical Simulation Study of Effective Parameters on SAGD Performance: Energy and Environment Research, v. 2, p. 140-156.

Steel, A., 2007, 304/304L Stainless Steel Data Sheet, <http://www.aksteel.com/pdf/markets_products/stainless/austenitic/304_304L_Data_Sheet.pdf>.

Sufi, A. H., H. J. Ramey Jr., and W. E. Brigham, 1982, Temperature Effects on Relative Permeabilities of Oil-Water Systems, SPE Annual Technical Conference and Exhibition, New Orleans, Louisiana, Society of Petroleum Engineers of AIME.

Svrcek, W. Y., and A. K. Mehrotra, 1989, Properties of Peace River Bitumen Saturated with Field Gas Mixtures: Journal of Canadian Petroleum Technology, v. 28, p. 50-56.

Tamim, M., J. H. Abou-Kassem, and S. M. Farouq Ali, 2000, Recent Developments in Numerical Simulation Techniques of Thermal Recovery Processes: Journal of Petroleum Science and Engineering, v. 26, p. 283-289.

Treiber, L. E., and W. W. Owens, 1972, A Laboratory Evaluation of the Wettability of Fifty Oil-Producing Reservoirs: Society of Petroleum Engineers Journal, v. 12, p. 531-540.

Tunio, S. Q., A. H. Tunio, N. A. Ghirano, and Z. M. El Adawy, 2011, Comparison of Different Enhanced Oil Recovery Techniques for Better Oil Productivity: International Journal of Applied Science and Technology, v. 1, p. 143-153.

Van Dijke, M. I. J., and K. S. Sorbie, 2002, The Relation Between Interfacial Tensions and Wettability in Three-Phase Systems: Consequences for Pore Occupancy and Relative Permeability: Journal of Petroleum Science and Engineering, v. 33, p. 39-48.

Wang, X., 2010, Experimental and Numerical Studies on Multiple Well Pairs SAGD Performance: M.Sc. thesis, University of Alberta (Canada), Ann Arbor, 141 p.

Wilson, M. D., 1982, Origins of Clays Controlling Permeability in Tight Gas Sands: Journal of Petroleum Technology, v. 34, p. 2,871-2,876.

Worden, R., and S. Morad, 2003, Clay Minerals in Sandstones: Controls on Formation, Distribution and Evolution, v. 34, p. 3-41.

Xu, R., 2010, Zeta Potential Determination of Colloidal Particles, USA.

Yuan, J.-Y., D. H.-S. Law, and T. N. Nasr, 2003, Impacts of Gas in SAGD: History Matching of Lab Scale Tests, Canadian International Petroleum Conference, Calgary, Alberta, Petroleum Society of Canada.

Yuan, J. Y., D. H. S. Law, and T. N. Nasr, 2002, Benefit of Wettability Change Near the Production Well in SAGD, Canadian International Petroleum Conference, Calgary, Alberta Petroleum Society of Canada.

Yukselen, Y., and A. Kaya, 2003, Zeta Potential of Kaolinite in the Presence of Alkali, Alkaline Earth and Hydrolyzable Metal Ions: Water, Air, & Soil Pollution, v. 145, p. 155-168.

Zhao, L., D. H. S. Law, T. N. Nasr, R. Coates, H. Golbeck, G. Beaulieu, and G. Heck, 2005, SAGD Wind-Down: Lab Test and Simulation: Journal of Canadian Petroleum Technology, v. 44, p. 49-53.

Zhao, L., A.-F. Li, X.-J. Wu, H.-j. Xie, J.-j. Wang, and Q. Wang, 2013, Oil-water Interfacial Tension Effects on Relative Permeability Curves in Low-permeability Reservoirs: Journal of Petroleum Science Research, v. 2, p. 75-81.

APPENDIX A

TABLE 25—ZETA POTENTIAL MEASUREMENT DETAILS OF REFERENCE MATERIALS AND CLAY-ASPHALTENE MIXTURES

	Cuvette	Zeta Potential Run 1	Zeta Potential Run 2	Zeta Potential Run 3	Zeta Potential Run 4	Zeta Potential Run 5	Average Zeta Potential (mV)	TDS (ppm)	pH	Particle Size (nm)
Sand	1	-41.13	-34.46	-29.54	-42.31	-41.51	-37.79	70	5.9	3942
	2	-38.41	-41.59	-55.75	-58.42	-59.16	-50.666	70	5.9	3942
	3	-34.39	-38.49	-31.58	-41.44	-44.67	-38.114	70	5.9	3942
	4	-38.07	-45.03	-61	-59.23	-59.5	-52.566	70	5.9	3942
	5	-44.17	-47.32	-48.1	-46.78	-42.59	-45.792	70	5.9	3942
					Total Average		-44.986			
Clay type 1	1	-25.13	-30.42	-35.78	-42.31	-44.66	-35.66	68	5.5	1200
	2	-28.07	-26.86	-36.23	-38.44	-40.97	-34.114	68	5.5	1200
					Total Average		-34.887			
Clay type 2	1	-25.08	-37.81	-39.18	-39.93	-49.34	-38.268	68	5.5	2300
	2	-19.04	-32.09	-44.45	-50.35	-51.96	-39.578	68	5.5	2300
					Total Average		-38.923			
Clay type 2-steam injected 6 hours	1	-24.61	-33.63	-35.13	-50.87	-55.79	-40.006	70	5.5	2400
	2	-20.77	-18.47	-42.97	-48.61	-50.73	-36.31	70	5.5	2400
					Total Average		-38.158			
Clay type 1 + asphaltene SAGD1	1	-26.62	-31.54	-30.43	-32.34	-31.81	-30.548	69	5.6	1545
	2	-31.73	-31.77	-34.18	-34.44	-33.32	-33.088	69	5.6	1277
	3	-29.92	-31.02	-30.68	-32.21	-31.85	-31.136	69	5.6	1362
					Total Average		-31.59			
Clay type 2 + asphaltene SAGD2	1	-29.62	-34.25	-47.14	-44.81	-40.44	-39.252	64	5.8	2482
	2	-27.38	-27.74	-39.09	-42.21	-52.31	-37.746	64	5.8	x
	3	-30.27	-46.4	-42.48	-40.94	-39.9	-39.998	64	5.8	2093
					Total Average		-38.999			

TABLE 26—ZETA POTENTIAL MEASUREMENT DETAILS OF ORIGINAL BITUMEN AND PRODUCED OIL SAMPLES FROM EXPERIMENTS

	Cuvette	Zeta Potential Run 1	Zeta Potential Run 2	Zeta Potential Run 3	Zeta Potential Run 4	Zeta Potential Run 5	Average Zeta Potential (mV)	TDS (ppm)	pH	Particle Size (nm)
Original bitumen	1	-41.79	-56.48	-64.72	-70.7	-72.7	-61.278	70	5.3	439
	2	-34.95	-22.07	-62.46	-70.74	-74.31	-52.906	70	5.3	460
					Total Average		-57.092			
Hot water injection oil	1	-56.05	-51.44	-71.75	-70.17	-67.54	-63.39	64	5.3	284
	2	-42.31	-20.57	-55.7	-69.14	-69.51	-51.446	64	5.3	281
					Total Average		-57.418			
SAGD1 oil	1	-45.95	-27.38	-48.89	-68.12	-69.47	-51.962	69	5.2	395
	2	-48.8	-36.96	-73.27	-76.4	-72.14	-61.514	69	5.2	394
					Total Average		-56.738			
SAGD2 oil	1	-39.56	-17.59	-28.54	-78.64	-78.95	-48.656	64	5.5	453
	2	-55.02	-47.83	-60.07	-71.54	-69.23	-60.738	64	5.5	447
					Total Average		-54.697			

TABLE 27—ZETA POTENTIAL MEASUREMENT DETAILS OF ORIGINAL ASPHALTENE AND ASPHALTENES OBTAINED FROM PRODUCED OIL SAMPLES

	Cuvette	Zeta Potential Run 1	Zeta Potential Run 2	Zeta Potential Run 3	Zeta Potential Run 4	Zeta Potential Run 5	Average Zeta Potential	TDS (ppm)	pH	Particle Size (nm)
Original Asphaltene	1	-18.06	-12.29	1.76	-10.74	-10.87	-10.040	76	5.6	1503
	2	-22.2	-4.5	-13	-19.63	-11.97	-14.260	76	5.6	1730
	3	-30.64	-19.2	-15.32	-19.9	-11.66	-19.344	76	5.6	1280
					Total Average		-14.548			
HWI Asphaltene	1	-29.41	-23.57	-20.38	-20.02	-22.69	-23.214	87	5.5	1549
	2	-27.77	-6.12	-11.82	-11.25	-12.53	-13.898	87	5.5	x
	3	-32.17	-15.61	-18.58	-17.42	-15.3	-19.816	87	5.5	x
					Total Average		-18.976			
SAGD1 Asphaltene	1	-22.52	-22.52	-18.47	-20.96	-20.93	-21.08	72	5.4	1269
	2	-25.61	-20.46	-13.82	-13.23	-13.66	-17.356	72	5.4	1615
	3	-26.54	-14.5	-16.23	-18.42	-20.06	-19.15	722	5.4	1698
					Total Average		-19.195			
SAGD2 Asphaltene	1	-20.26	-13.87	-10.23	-11.32	-5.78	-12.292	70	5.1	x
	2	-20.85	-13.3	-7.21	-7.36	-12.49	-12.242	70	5.1	1880
	3	-19.44	-11.81	-8.24	-4.78	-8.94	-10.642	70	5.1	1317
					Total Average		-11.725			

TABLE 28—ZETA POTENTIAL MEASUREMENT DETAILS OF PRODUCED WATER SAMPLES

	Cuvette	Zeta Potential Run 1	Zeta Potential Run 2	Zeta Potential Run 3	Zeta Potential Run 4	Zeta Potential Run 5	Average Zeta Potential (mV)	TDS (ppm)	pH	Particle Size (nm)
Produced water HWI	1	-35.13	-46.25	-48.12	-46.31	-45.47	-44.256	128	6	530
	2	-38.08	-43.88	-45.27	-47.4	-47.06	-44.338	128	6	575
					Total Average		-44.297			
Produced water SAGD1	1	-21.16	-34.56	-35.46	-38.93	-36.79	-33.38	290	7.1	1124
	2	-31.38	-35.9	-37.48	-37.68	-34.82	-35.452	290	7.1	1465
					Total Average		-34.416			
Produced water SAGD2	1	-51.24	-53.88	-53.13	-51.65	-51.67	-52.314	51	6.1	369
	2	-45.93	-54.27	-54.47	-55.12	-54.34	-52.826	51	6.1	371
					Total Average		-52.57			

TABLE 29—ZETA POTENTIAL MEASUREMENT DETAILS OF BEFORE EXPERIMENT OIL SAND SAMPLES AND HWI POSTMORTEM SAMPLES

	Cuvette	Zeta Potential Run 1	Zeta Potential Run 2	Zeta Potential Run 3	Zeta Potential Run 4	Zeta Potential Run 5	Average Zeta Potential (mV)	TDS (ppm)	pH	Particle Size (nm)
Before experiment oil sand clay type 1	1	-28.81	-31.06	-31.79	-32.61	-38.61	-32.576	78	5.6	1309
	2	-29.65	-37.88	-49.24	-44.57	-47.85	-41.838	78	5.6	1717
	3	-30.37	-31.97	-42.99	-41.14	-38.36	-36.966	78	5.6	2296
					Total Average		-37.127			
Before experiment oil sand clay type 2	1	-31.28	-32.18	-35.97	-38.73	-39.71	-35.574	85	5.6	1103
	2	-30.2	-32.04	-43.96	-41.7	-41.85	-37.95	85	5.6	1300
	3	-31.85	-37.95	-46.38	-42.8	-42.51	-40.298	85	5.6	1409
					Total Average		-37.941			
HWI (R1)	1	-32.59	-29.02	-30.16	-28.24	-32.74	-30.55	72	5.6	2130
	2	-28.98	-30.07	-37.8	-38	-38.25	-34.62	72	5.6	2601
	3	-29.62	-34.28	-37.64	-40.45	-39.92	-36.382	72	5.6	2236
					Total Average		-33.851			
HWI (R2)	1	-31.57	-40.65	-40.94	-42.71	-40.96	-39.366	70	5.9	x
	2	-30.24	-30.07	-37.85	-47.11	-44.79	-38.012	70	5.9	954
	3	-31.5	-32.85	-42.5	-43.5	-45.76	-39.222	70	5.9	1138
					Total Average		-38.867			

TABLE 30—ZETA POTENTIAL MEASUREMENT DETAILS OF SAGD1 AND SAGD2 POSTMORTEM SAMPLES

	Cuvette	Zeta Potential Run 1	Zeta Potential Run 2	Zeta Potential Run 3	Zeta Potential Run 4	Zeta Potential Run 5	Average Zeta Potential (mV)	TDS (ppm)	pH	Particle Size (nm)
SAGD1 (R3)	1	-29.27	-30.85	-36.15	-37.5	-33.88	-33.53	77	5.7	x
	2	-29.18	-29.45	-34.7	-37.25	-33.95	-32.906	77	5.7	1847
	3	-27.23	-32.08	-39.65	-37.37	-37.84	-34.834	77	5.7	x
					Total Average		-33.757			
SAGD1 (R4)	1	-29.77	-31.36	-40.51	-42.95	-41.76	-37.27	75	5.5	1351
	2	-31.38	-37.02	-45.83	-46.82	-45.76	-41.362	75	5.5	2206
	3	-31	-33.96	-40.99	-45.46	-45.93	-39.468	75	5.5	1183
					Total Average		-39.367			
SAGD2 (R5)	1	-34.29	-37.34	-44.12	-43.35	-40.89	-39.998	84	6.3	1078
	2	-35.09	-40.62	-45.97	-44.94	-46.6	-42.644	84	6.3	2167
	3	-32.63	-36.22	-44.77	-49.1	-46.05	-41.754	84	6.3	3636
					Total Average		-41.465			
SAGD2 (R6)	1	-37.82	-37.69	-42.41	-48.83	-44.64	-42.278	68	5.7	888
	2	-31.02	-35.78	-42.31	-43.69	-44.23	-39.406	68	5.7	1171
	3	-36.08	-34.67	-45.06	-47.82	-42.96	-41.318	68	5.7	1006
					Total Average		-41.001			

APPENDIX B

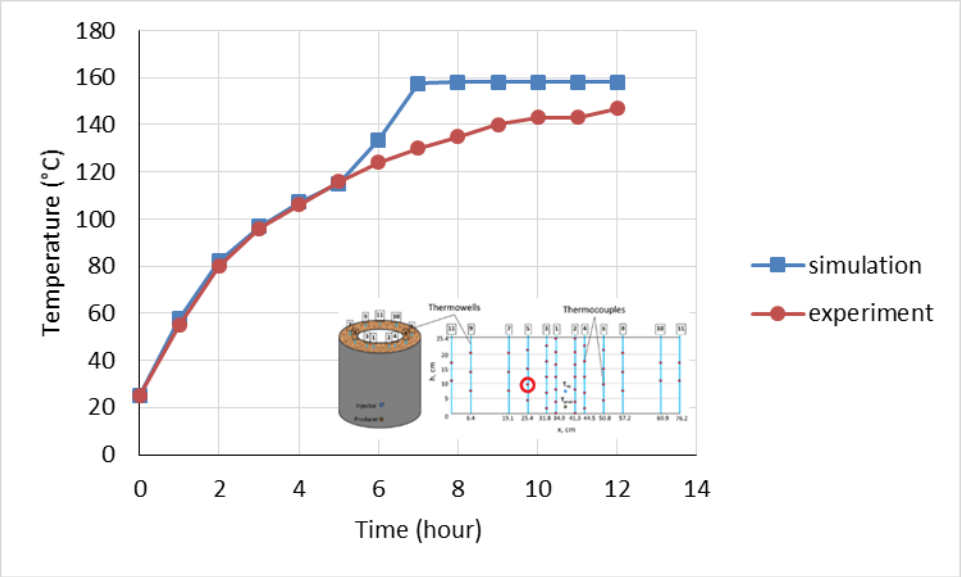

Fig. 51—SAGD1 temperature comparison between experiment and simulation, where the thermocouple located 25.4 cm away in horizontal direction and 9.8 cm away in vertical direction from the bottom left corner of the experimental setup.

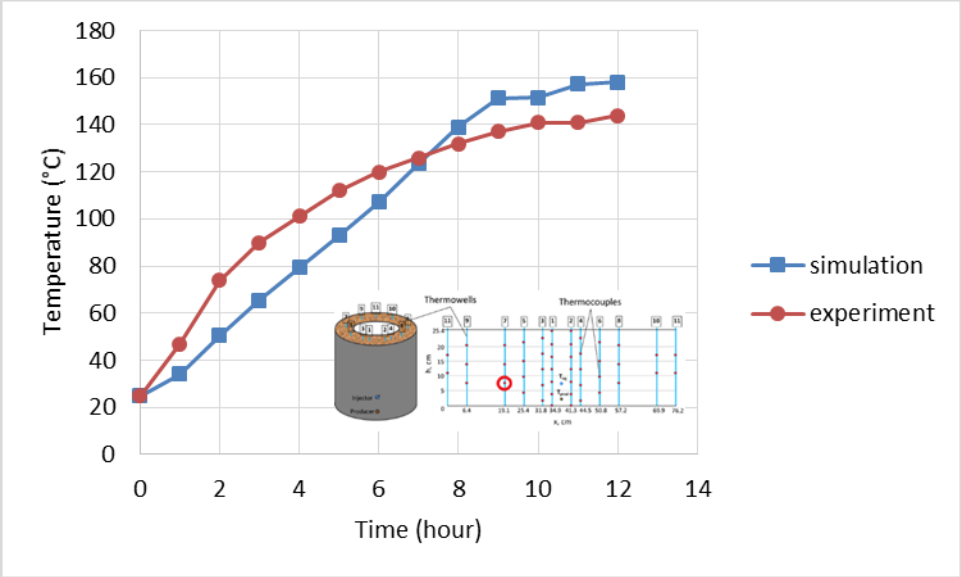

Fig. 52—SAGD1 temperature comparison between experiment and simulation, where the thermocouple located 19.1 cm away in horizontal direction and 7.8 cm away in vertical direction from the bottom left corner of the experimental setup.

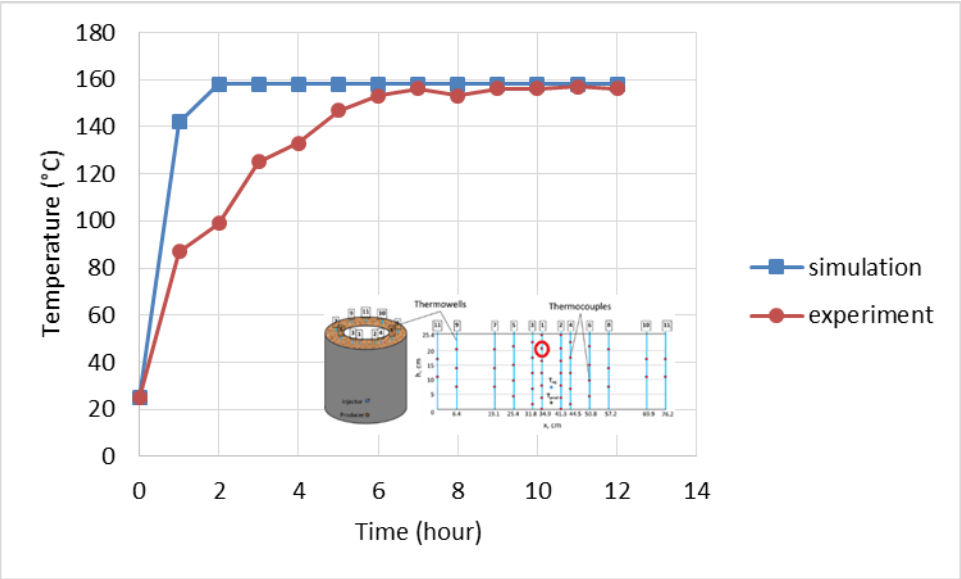

Fig. 53—SAGD1 temperature comparison between experiment and simulation, where the thermocouple located 34.9 cm away in horizontal direction and 20.5 cm away in vertical direction from the bottom left corner of the experimental setup.

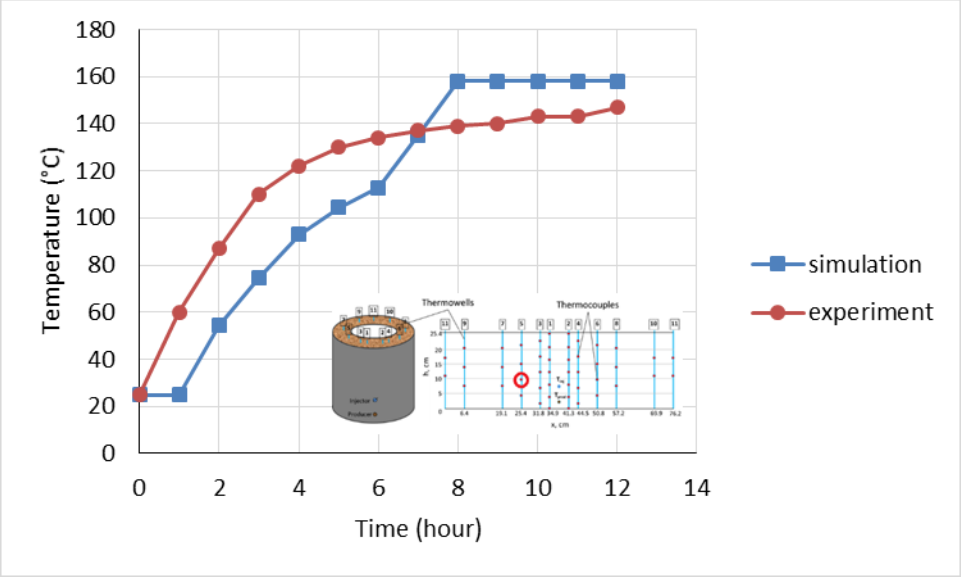

Fig. 54—SAGD2 temperature comparison between experiment and simulation, where the thermocouple located 25.4 cm away in horizontal direction and 9.8 cm away in vertical direction from the bottom left corner of the experimental setup.

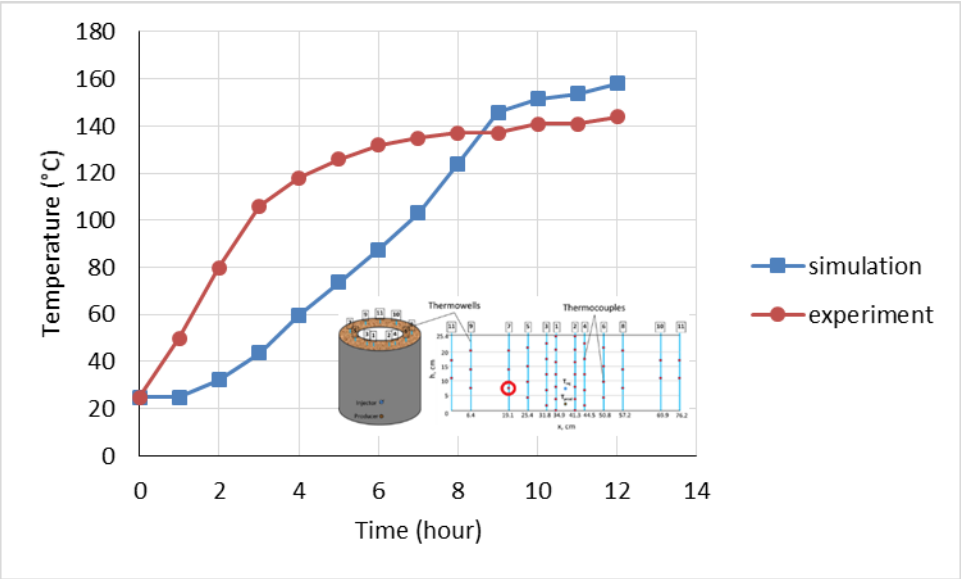

Fig. 55—SAGD2 temperature comparison between experiment and simulation, where the thermocouple located 19.1 cm away in horizontal direction and 7.8 cm away in vertical direction from the bottom left corner of the experimental setup.

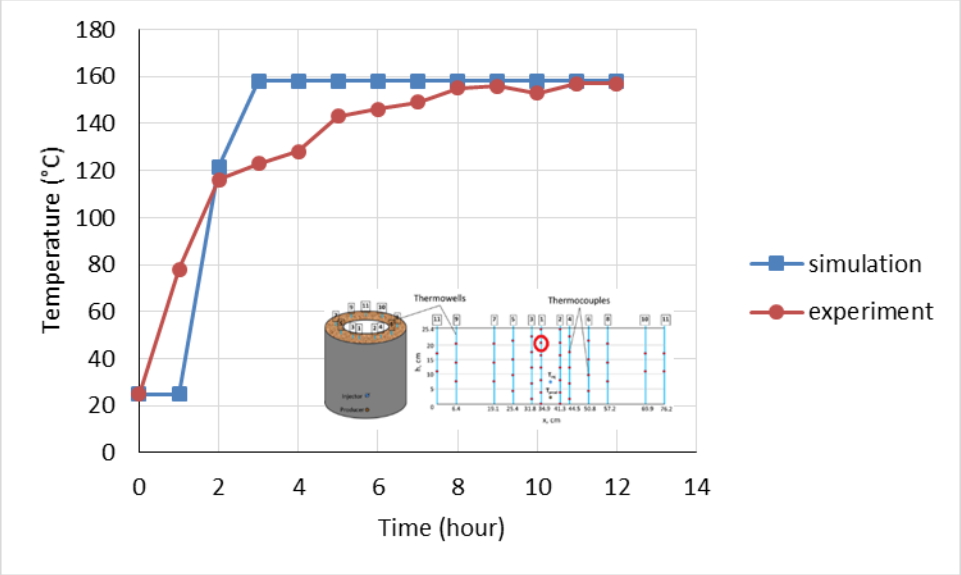

Fig. 56—SAGD2 temperature comparison between experiment and simulation, where the thermocouple located 34.9 cm away in horizontal direction and 20.5 cm away in vertical direction from the bottom left corner of the experimental setup.

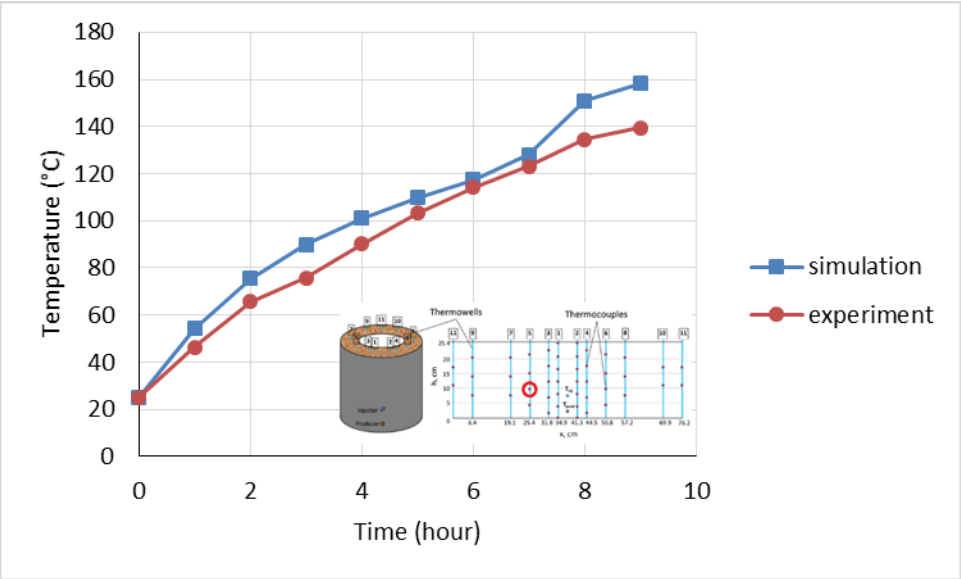

Fig. 57—HWI temperature comparison between experiment and simulation, where the thermocouple located 25.4 cm away in horizontal direction and 9.8 cm away in vertical direction from the bottom left corner of the experimental setup.

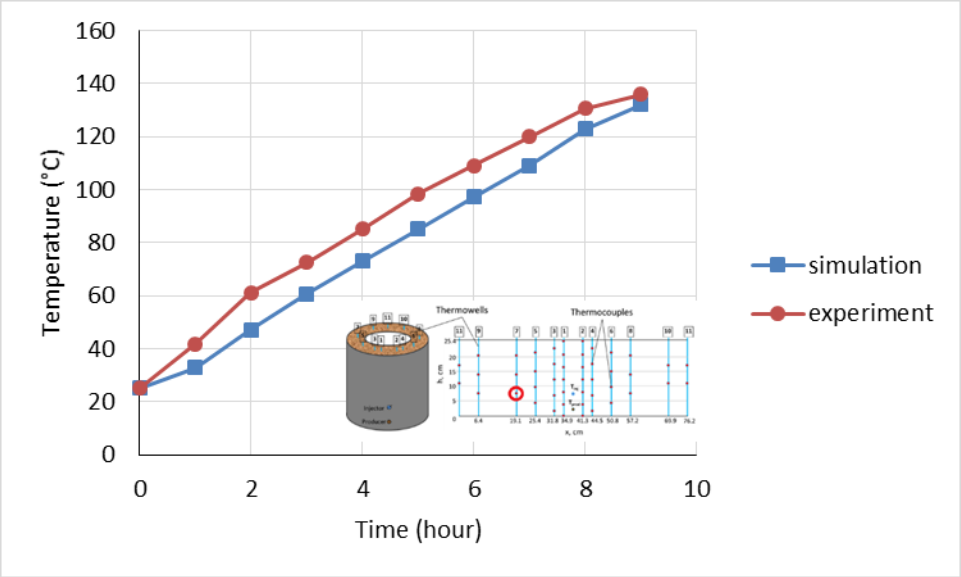

Fig. 58—HWI temperature comparison between experiment and simulation, where the thermocouple located 19.1 cm away in horizontal direction and 7.8 cm away in vertical direction from the bottom left corner of the experimental setup.

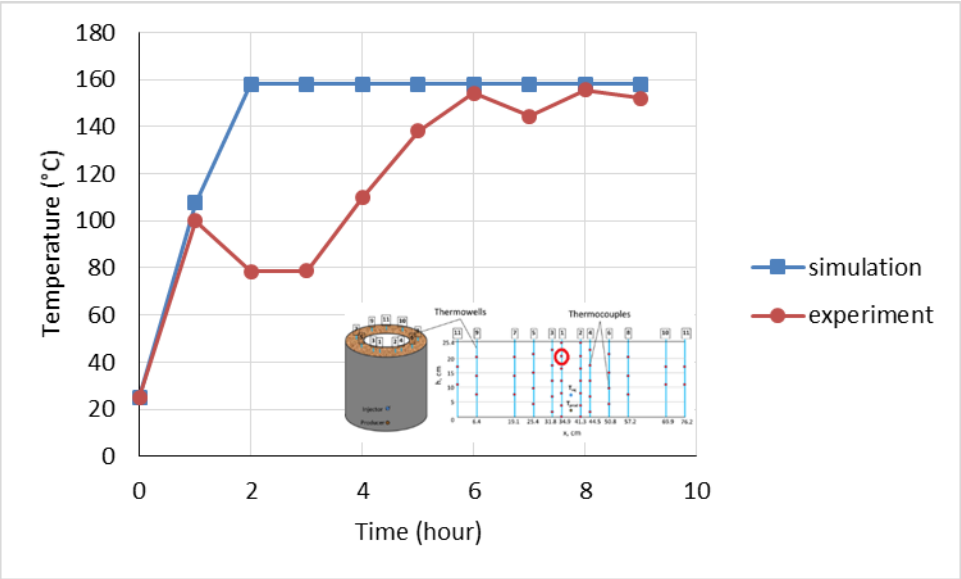

Fig. 59—HWI temperature comparison between experiment and simulation, where the thermocouple located 34.9 cm away in horizontal direction and 20.5 cm away in vertical direction from the bottom left corner of the experimental setup.

APPENDIX C

TABLE 31—VISCOSITY-TEMPERATURE RELATION USED IN NUMERICAL STUDIES

Temperature (°C)	Viscosity (cP)
21.1	95,587.3
26.7	36,253.6
32.2	16,530.1
37.8	8542.6
51.7	2329.7
65.6	867.3
79.4	390.7
93.3	200.2
121.1	67.9
148.9	28.8
176.7	14.2
204.4	7.7
232.2	4.6
260.0	2.9
287.8	1.9
315.6	1.3

APPENDIX D

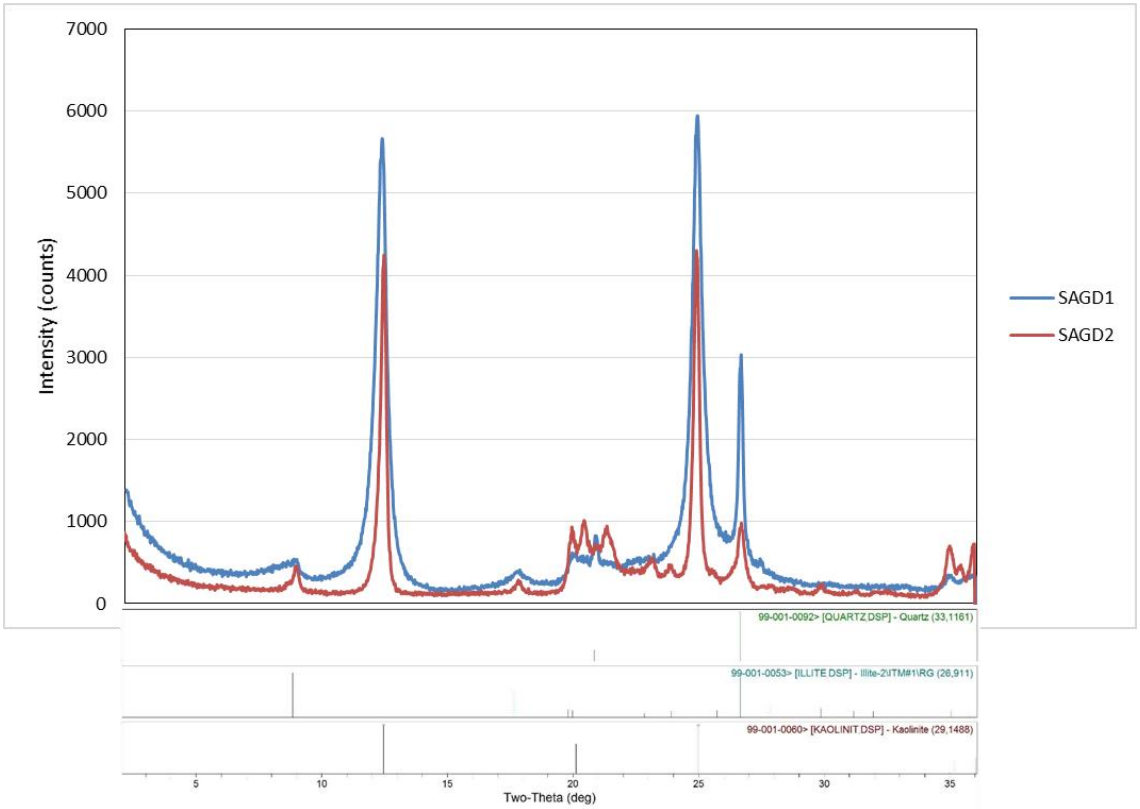

Fig. 60—XRD traces of SAGD1 and SAGD2 postmortem samples gathered from inside steam chamber region.

APPENDIX E

TABLE 32—BERRYMAN B-12 CHEMTOOL COMPOSITION

Ingredient	CAS Number	Weight
Ethylbenzene	100-41-4	10 – 15%
Petroleum Distillates	64742-47-8	30 – 40%
n-Propanol	71-23-8	5 – 10%
Xylene (mixed isomers)	1330-20-7	40 – 50%

APPENDIX F

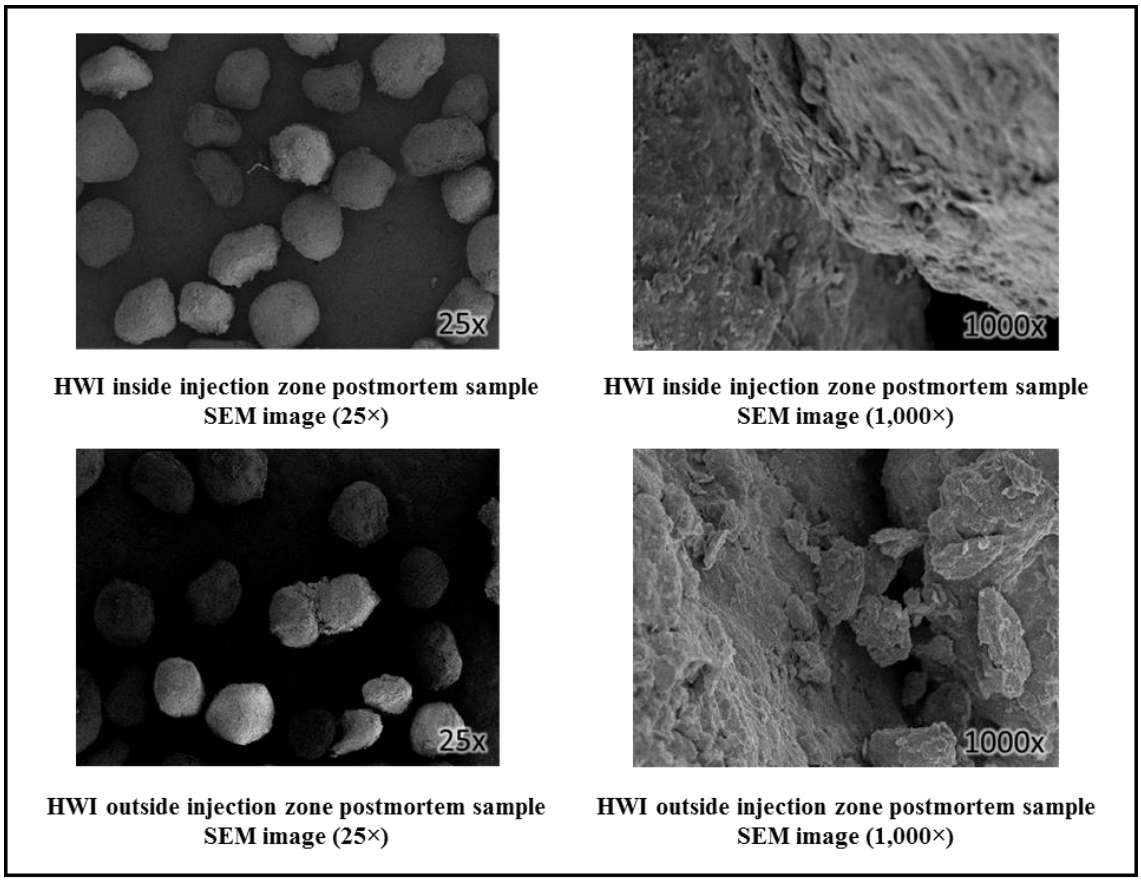

Fig. 61—SEM images of the postmortem samples of HWI experiment

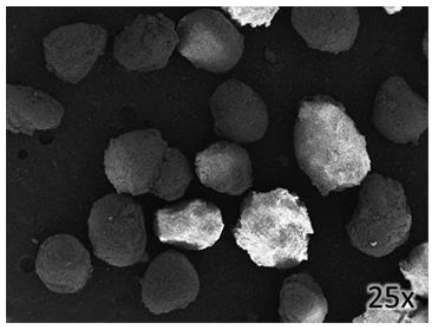

SAGD1 inside injection zone postmortem sample SEM image (25×)

SAGD1 inside injection zone postmortem sample SEM image (1,000×)

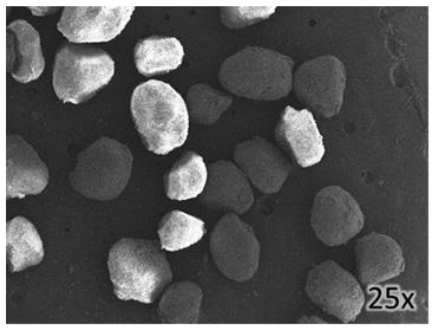

SAGD1 outside injection zone postmortem sample SEM image (25×)

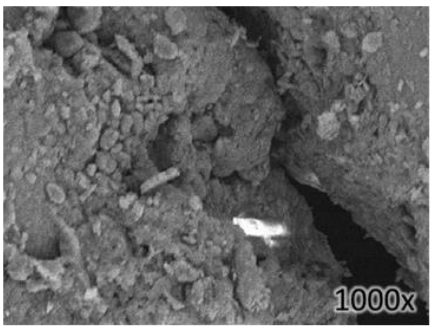

SAGD1 outside injection zone postmortem sample SEM image (1,000×)

Fig. 62—SEM images of the postmortem samples of SAGD1 experiment

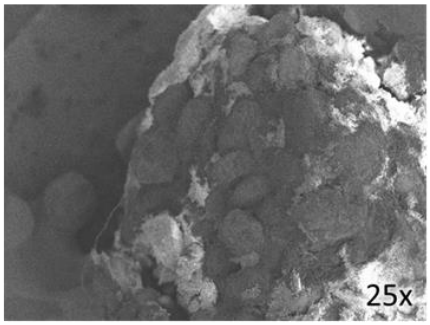

SAGD2 inside injection zone postmortem sample SEM image (25×)

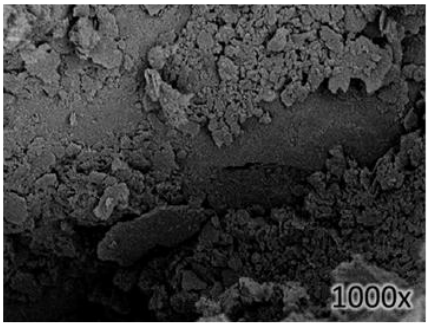

SAGD2 inside injection zone postmortem sample SEM image (1,000×)

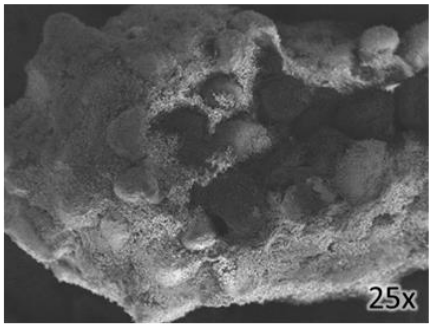

SAGD2 outside injection zone postmortem sample SEM image (25×)

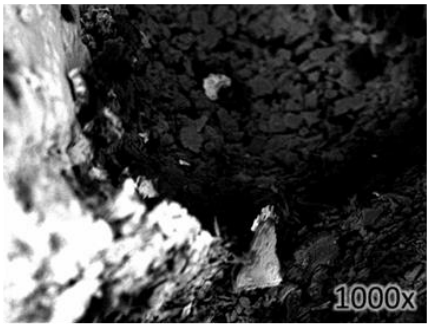

SAGD2 outside injection zone postmortem sample SEM image (1,000×)

Fig. 63—SEM images of the postmortem samples of SAGD2 experiment